From polyelectrolytes towards poly amino acid complexes and protein polymers

Von der Fakultät für Mathematik, Informatik und Naturwissenschaften der RWTH Aachen University zur Erlangung des akademischen Grades einer Doktorin der Naturwissenschaften genehmigte Dissertation

Vorgelegt von

Ekaterina Buvalaia
Master in medizinischer Physik aus
Moskau, Russland

Berichter: Prof. Dr. Stephan Förster
Prof. Dr. Walter Richtering

Tag der mündlichen Prüfung: 03.06.2025

Diese Dissertation ist auf den Internetseiten der Universitätsbibliothek online verfügbar

1. Abstract

Polyelectrolytes (PEs), polymers with ionizable groups, are fundamental in a wide range of applications, reaching from environmental science to biomedical engineering. This thesis delves into two primary areas of study: first, bridging the knowledge gap between PEs and structurally more complex proteins, particularly focusing on structure and dynamics of PEs, second, examining the formation and behavior of polyelectrolyte complexes (PECs) under diverse environmental conditions.

Using polystyrene sulfonate (PSS) as a model PE, its structural and dynamic properties were studied, where dynamics was described as Zimm-like supplemented by internal friction (ZIF). This analysis is aimed to enhance the understanding of hydrodynamic interactions and internal friction within PEs by correlating collective diffusion with local chain dynamics. Dynamic light scattering (DLS), neutron spin-echo (NSE) spectroscopy, pulsed field gradient neutron magnetic resonance (PFG-NMR) spectroscopy and small-angle X-ray scattering (SAXS) were employed to investigate the structure and dynamics of PSS at dilute and semidilute regimes.

The second part of the thesis focuses on PECs, composed of oppositely charged poly amino acids (PAAs), examining how environmental factors and PAA variations influence PECs structure. Mixing charged PAAs results in high-density droplet phases and dense hexagonal lattices of parallel α-helices, affected by PAA properties like molecular weight, concentration and pH. These mixtures are promising for applications in drug delivery and tissue engineering, requiring an understanding of their phase transitions in response to temperature, pH and ionic strength. The study also explores how magnetic fields and shear forces impact PEC formation and stability, revealing a range of structures from crystalline α-helices to amorphous phases based on salt concentrations.

Through these investigations, this thesis aims to shed light on the complex behaviors of PEs and PECs, contributing to a deeper understanding of their roles in diverse applications and biological processes.

2. Zusammenfassung

Polyelektrolyte (PE), Polymere mit ionisierbaren Gruppen, sind grundlegend in einer Vielzahl von Anwendungen, die von den Umweltwissenschaften bis zum biomedizinischen Engineering reichen. Diese Arbeit befasst sich mit zwei Hauptbereichen: erstens, die Wissenslücke zwischen PE und komplexeren Proteinen zu überbrücken, insbesondere mit dem Fokus auf Struktur und Dynamik von PEs, und zweitens, die Bildung und das Verhalten von Polyelektrolytkomplexen (PEC) unter verschiedenen Umweltbedingungen zu untersuchen.

Mit Polystyrolsulfonat (PSS) als Modell-PE wurden dessen strukturellen und dynamischen Eigenschaften untersucht, wobei die Dynamik als Zimm-artig mit zusätzlicher interner Reibung (ZIF) beschrieben wurde. Diese Analyse zielt darauf ab, das Verständnis von hydrodynamischen Wechselwirkungen und interner Reibung innerhalb von PEs zu erweitern, indem kollektive Diffusion mit lokaler Kettenbewegung in Beziehung gesetzt werden. Dynamische Lichtstreuung (DLS), Neutronen-Spin-Echo (NSE)-Spektroskopie, gepulste Feldgradienten-NMR-Spektroskopie und Kleinwinkel-Röntgenstreuung (SAXS) wurden eingesetzt, um die Struktur und Dynamik von PSS in verdünnten und halbverdünnten Bedingungen zu untersuchen.

Der zweite Teil der Arbeit konzentriert sich auf PECs, die aus gegensätzlich geladenen Polyaminosäuren (PAA) bestehen, und untersucht, wie Umweltfaktoren und Variationen der PAA die Struktur der PECs beeinflussen. Das Mischen geladener PAA führt zu Phasen hochdichter Tropfen und dicht gepackten hexagonalen Gittern aus parallelen α-Helices, beeinflusst durch Eigenschaften der PAA wie Molekulargewicht, Konzentration und pH-Wert. Diese Mischungen sind vielversprechend für Anwendungen in der Arzneimittelabgabe und im Tissue Engineering, was ein Verständnis ihrer Phasenübergänge in Reaktion auf Temperatur, pH-Wert und Ionenstärke erfordert. Die Studie erforscht auch, wie Magnetfelder und Scherkräfte die Bildung und Stabilität von PECs beeinflussen und offenbart eine Reihe von Strukturen von kristallinen α-Helices bis zu amorphen Phasen, abhängig von der Salzkonzentration.

Diese Forschungsarbeit zielt darauf ab, das komplexe Verhalten von PEs und PECs zu beleuchten und zu einem tieferen Verständnis ihrer Rolle in vielfältigen Anwendungen und biologischen Prozessen beizutragen.

3. Author contributions

The following is the list of projects that are presented in this dissertation:

- Interchain hydrodynamic interaction and internal friction of polyelectrolytes

Status: Published in ACS Macro Letters
Ekaterina Buvalaia, Margarita Kruteva, Ingo Hoffmann, Aurel Radulescu, Stephan Förster, and Ralf Biehl, ACS Macro Letters 2023 12 (9), 1218-1223, DOI: 10.1021/acsmacrolett.3c00409

I was responsible for the sample preparation and performing the experiments with SAXS, SANS, NSE, DLS and PFG-NMR. SAXS experiments were done under supervision from Ralf Biehl. PFG-NMR measurements were conducted with the help of Margarita Kruteva. SANS experiments were assisted by Aurel Radulescu, while NSE experiments were assisted by Ingo Hoffmann. I and Ralf Biehl created the Python script used in the analysis of the scattering data as well as other experiments. I, Margarita Kruteva and Ralf Biehl wrote the manuscript.

- Formation of ordered phases in dense poly amino acid coacervate droplets

Status: Manuscript has not been published

I was responsible for the sample preparation and performing the experiments with SAXS, optical microscopy and NMR. SAXS experiments were done under supervision from Martin Dulle. NMR measurements were assisted by Jürgen Allgaier. SEM was conducted by Beate Förster. I and Ralf Biehl created the Python script used in the analysis of the scattering data as well as other experiments. I, Margarita Kruteva, Ralf Biehl and Stephan Förster wrote the manuscript.

4. Contents

1. Abstract 3

2. Zusammenfassung 4

3. Author contributions 5

4. Contents 6

5. List of Figures 8

6. Abbreviations 11

7. Symbols 12

8. Introduction 15

9. Theory 17

9.1. Polyelectrolytes 17

9.2. Structure of PEs 17

9.3. Polyelectrolyte complexes 18

9.4. PECs phase transition behaviour and structure 18

9.5. Scattering of light, X-rays and neutrons 20

9.6. Small-angle scattering (SAXS & SANS) 22

9.6.1. Form factor 24

9.6.2. Structure factor 25

9.6.3. Crystal structure 27

9.7. Polymer dynamics 29

9.7.1. Dynamics of polymer chains in solution 29

9.7.2. Dynamics of PEs 30

9.7.3. Concentration effects on dynamics 33

10. Methods 33

10.1. Small-angle scattering instruments 33

10.1.1. Collimation 33

10.1.2. Small-angle X-ray scattering 34

10.1.3. Small-angle neutron scattering 36

10.2. Neutron spin echo to measure polymer chain dynamics 37

10.3. Complementary methods 38

10.3.1. Dynamic light scattering 38

10.3.2. Nuclear magnetic resonance and PFG-NMR 41

10.3.3. Optical microscopy 43

11. Interchain hydrodynamic interaction and internal friction of polyelectrolytes 47

11.1. Abstract 47

11.2. Introduction 47

11.3. Materials 49

11.4. Results 49

11.4.1. Collective diffusion 49

11.4.2. Structure of PSS 51
11.4.3. Dynamics of PSS 54
11.5. Conclusion 60
12. Formation of ordered phases in dense poly amino acid coacervate droplets 61
12.1. Abstract 61
12.2. Introduction 61
12.3. Materials and preparation 62
12.3.1. Centrifugation 62
12.4. Results 63
12.4.1. Physical properties of PECs 63
12.4.2. Chemical composition of precipitate 64
12.4.3. Structure of PECs 65
12.4.4. How to influence the structure of PECs 75
12.5. Conclusion 79
13. Conclusions 81
14. Acknowledgments 84
15. Eidesstätliche Erklärung 85
16. Supplementary 86
17. References 110

5. List of Figures

Fig. 1 Typical scattering experiment 21
Fig. 2 Sphere formfactor..... 25
Fig. 3 RMSA SFs at $\gamma = 0{,}2$ and the volume fraction $\eta = 0{,}1$..... 26
Fig. 4 Two Yukawa potential for particle with radius $R = 0.5\ nm, K2 = -kT, \rho 1 = 0.1\ nm, \rho 2 = 2\ nm$ 27
Fig. 5 SF of a hexagonal lattice filled with long cylinders..... 29
Fig. 6 Zimm model representation of the polymer 31
Fig. 7 Polymer chain in ZIF representation where beads are connected with springs and internal friction between the elements is also implemented..... 32
Fig. 8 A scheme of a SAXS/SANS instrument and a beam propagation..... 34
Fig. 9 Two types of collimation systems in SAXS instruments..... 34
Fig. 10 Representation of the NSE spectrometer..... 38
Fig. 11 The sequence of getting information during the DLS measurement..... 39
Fig. 12 The main components of a DLS instrument..... 39
Fig. 13 Image formation in LM 44
Fig. 14 Magnification of the specimen's image in the microscope..... 45
Fig. 15 Light passing through the medium with refractive index n..... 45
Fig. 16 Collective diffusion coefficient Dc measured by DLS (fast mode, Q = 0.0264 nm^{-1}, solid symbols) and self-diffusion Ds (open symbols, c_p = 10 mg/ml) measured by PFG-NMR for PSS 39k. 50
Fig. 17 SAXS data for PSS 39k after background correction and scaled by concentration (c_s shifted consecutively by 10 for visibility). 52
Fig. 18 SAXS data for PSS 39k in NaCl, RbCl and CsCl salts after background correction and scaled by concentration..... 53
Fig. 19 SANS data at T=20ºC for PSS 39k (left) and 17.5k (right) after background correction and desmearing measured at KWS2, MLZ, Garching [79]..... 54
Fig. 20 NSE measured intermediate scattering function I(Q,t)/I(Q,0) up to 100 ns for PSS 39k 500 mM at 30 mg/mL measured at IN15, ILL, Grenoble [95]. 55
Fig. 21 Effective diffusion coefficients $Deff$ for PSS 39k cp = 30 mg/ml with respective parameters from the full fit model 56
Fig. 22 Viscosity scaled $Deff$ for PSS 39k at different temperatures..... 59

Fig. 23 Images from the optical microscope made for the mixtures of PASP and PLA at different NaCl concentrations directly after preparation at 0,7 mM (10,7 mg/ml) total PE concentration. 63
Fig. 24 NMR spectra of separate PAAs and PECs at 0 and 2400mM NaCl 64
Fig. 25 SAXS curves for PASP+PLA (2mM PAAs concentration) PECs at different NaCl concentrations..... 66
Fig. 26 Possible structure of PECs dense phase at low and high salt concentrations..... 67
Fig. 27 SAXS curves for PASP/PGA+PLA PECs at 2400mM NaCl concentrations with or without centrifugation before the SAXS measurement..... 68
Fig. 28 SAXS curves for PECs with different composition..... 69
Fig. 29 SAXS curves for PECs at 2400 mM NaCl..... 71
Fig. 30 SAXS curves for PASP+PLA at 0 mM NaCl..... 71
Fig. 31 Peaks' evaluation for PASP+PLA at 0 mM NaCl..... 73
Fig. 32 SEM image of 200 AAs PASP+PLA 0mM NaCl sample..... 74
Fig. 33 Comparison of not sheared and sheared samples of PASP+PLA at 0mM NaCl, 200 AAs per chain..... 76
Fig. 34 Influence of the magnetic field on the PECs structure..... 77
Fig. 35 SAXS data for PASP+PLA 0mM NaCl 100 AAs/chain sample crosslinked with a 2% glutaraldehyde solution in dry and hydrated states 79

Fig. S1 Collective diffusion coefficient DC measured by DLS (fast mode, solid symbols) and self-diffusion DS (open symbols, conc.=10 mg/ml) measured by PFG-NMR for PSS 17.5k 86
Fig. S2 SAXS data for PSS 17.5k 89
Fig. S3 Relevant SAXS fit parameters for the generalized Gaussian worm (R_{core}, excluded volume parameter υ) and for the two-Yukawa potential (screening length κ_I, surface potential K_i in units kT)..... 91
Fig. S4 SAXS data for PSS 39k in NaCl, RbCl and CsCl salts after background correction and scaled by concentration..... 92
Fig. S5 SAXS data for PSS 17.5k in NaCl, RbCl and CsCl salts after background correction and scaled by concentration..... 93
Fig. S6 SANS data at T=20ºC for PSS 39k (left) and 17.5k (right) after background correction and desmearing measured at KWS2, MLZ, Garching..... 94

Fig. S7 NSE measured intermediate scattering function $I(Q,t)/I(Q,0)$ up to 100 ns for PSS 39 kDa at 30 mg/ml measured at IN15, ILL, Grenoble 95
Fig. S8 NSE measured intermediate scattering function $I(Q,t)/I(Q,0)$ up to 100 ns for PSS 17.5 kDa at 30 mg/ml measured at IN15, ILL, Grenoble..... 96
Fig. S9 Effective diffusion coefficients $Deff$ for PSS 39kDa with respective parameters from the full fit model 97
Fig. S10 NSE measured intermediate scattering function $I(Q,t)/I(Q,0)$ up to 100 ns for PSS 39 kDa at 30 mg/ml measured at IN15, ILL, Grenoble for 20, 40 and 60 ºC..... 98
Fig. S11 Arrhenius behavior of internal friction in comparison to D_2O viscosity..... 99
Fig. S12 Images from the optical microscope made for the mixtures of PASP and PLA at different NaCl concentrations directly after preparation, in 3, 4,5 and 24 hours, at 0,7mM (10,7 mg/ml) total PE concentration..... 101
Fig. S13 Comparison of the SAXS curves for PGA+PLA PECs for 100 and 200 AAs/chain 102
Fig. S14 Comparison of the SAXS curves for PASP+PLA PECs at 1 and 2 mM total PAAs concentration 102
Fig. S15 Comparison of the SAXS curves for PASP/PGA+PLA PECs with and without centrifugation during samples preparation..... 103
Fig. S16 Comparison of the SAXS curves for PGA+PLA PECs at different PAAs ratios 104
Fig. S17 SAXS curves for PASP+PLA PECs for 30 and 50 AAs/chain..... 104
Fig. S18 SAXS curves for PSS 17kDa and PLA 100 AAs/chain PECs at 0 and 2400mM NaCl 105
Fig. S19 Temperature scans for PASP+PLA 100 AAs/chain 106
Fig. S20 Peaks' evaluation for PASP+PLA at 80 mM NaCl..... 107
Fig. S21 Sheared PASP+PLA sample at 20, 30, 40 and 50°C upon heating and cooling down..... 108
Fig. S22 Influence of the magnetic field on the PASP+PLA sample structure..... 109

6. Abbreviations

DLS	dynamic light scattering
FF	form factor
FID	free induction decay
FWHM	full width half maxima
HI	hydrodynamic interaction
IDP	intrinsically disordered protein
ISF	intermediate scattering function
LM	light microscope
MW	molecular weight
NA	numerical aperture
NMR	nuclear magnetic resonance
NSE	neutron spin echo
PAA	poly amino acid
PASP	poly(L-aspartic acid)
PDADMA	poly(diallyldimethylammonium)
PDMAEMA	poly(N,N-dimethylaminoethylmethacrylate)
PE	polyelectrolyte
PEC	polyelectrolyte complex
PFG-NMR	pulsed-field-gradient nuclear magnetic resonance
PGA	poly(L-glutamic acid)
PLA	poly(L-arginine hydrochloride)
PSS	polystyrene sulfonate
RMSA	rescaled mean spherical approximation
SANS	small-angle neutron scattering
SAXS	small-angle X-ray scattering
SEM	scanning electron microscope
SF	structure factor
TEM	transmission electron microscopy
ZIF	Zimm-like dynamics with internal friction
2Y	two Yukawa

7. Symbols

κ	Debye length
Q	scattering vector
I	intensity
k	wave vector
λ	wavelength
V	volume
2θ	scattering angle
n	refractive index
$\frac{d\Sigma}{d\Omega}$	macroscopic cross section
bgr	background
N	number of particles
S	structure factor
P	form factor
c	concentration
$g(r)$	radial distribution function
b	scattering length
r	position
$\langle\,\rangle$	mean ensemble average
ρ	scattering length density
$p(r)$	pair distance distribution function
R_g	radius of gyration
ν	excluded volume parameter
γ	incomplete gamma function
$1/k$	screening length
L_B	Bjerrum length
X	coupling parameter
Z_0	macroion charge
σ_0	macroion diameter
η	volume fraction
F	scattering amplitude

DW	Debye Waller factor
Z_0	lattice factor
(hkl)	Miller indices
c	Porod constant
d	lattice spacing
D_s	self diffusion coefficient
D_c	collective diffusion coefficient
η	viscosity
μ	single chain mobility
H	hydrodynamic function
p	mode number
τ	characteristic time
R_e	end-to-end distance
k_B	Boltzmann constant
T	temperature
τ_i	relaxation time
r_H	hydrodynamic radius
E	electric field intensity
e	charge of electron
m	mass of electron
c	light velocity in vacuum
r_0	Thomson radius
i_x	scattering intensity (the differential cross section)
σ	integral cross section
g^2	intensity autocorrelation
Γ	relaxation rate
B	strength of magnetic field
γ	gyromagnetic ratio
M	magnification
NA	numerical aperture
D_0	diffusion coefficient of single particles
c_I	ion concentration
c_s	salt concentration

c_p	PE concentration
$d(Q)$	diffused scattering
τ_Z	Zimm time
ξ_{int}	friction between neighboring beads
τ_p	mode relaxation time
τ_{int}	internal friction time
R_{HI}	hydrodynamic interaction screening radius
a	lattice constant
d	domain size

8. Introduction

Polyelectrolytes (PEs) are charged polymers that are characterized by their charge, the screening by the surrounding fluid and additional hydrophobic/hydrophilic properties dependent on the monomers present in the chain. Compared to intrinsically disordered proteins (IDPs), PEs are simplified versions which allow to study basic principles. Protein polymers, defined as repeating short amino acid sequences, are known to undergo phase separations like mixtures of oppositely charged PEs [1]. Such phase behaviors are also driving the formation of membrane less compartments in cells [2]–[5]. Using simple PEs, poly amino acids (PAAs) and well-defined protein polymers open a path to examine specific interactions between the chains that are too complex to be investigated using IDP.

In this work we explore the progression from simple PEs to more complex protein polymer complexes (PECs). This approach allows us to examine and compare the structure, dynamics, and phase behavior across these systems. For simple PE, polystyrene sulfonate (PSS), internal friction is investigated. Internal friction was studied before in IDPs, but still the contributing interactions are not fully understood. The phase behavior of PAA systems involving opposite charges is probed by looking at the mixing two oppositely charged PAA, giving ideas for future studies involving the mixing of protein polymers and the sequence dependence in protein polymers and their functionalities.

Starting with a thorough investigation of the structural elements of PEs, particularly PSS as the classical PE, we explore how this charged polymer interacts with its environment, focusing on how variables such as pH and ionic strength influence its behavior. PEs are polymers with ionizable groups along their chains, creating charged molecules in solution. They are used for different applications from biomedical engineering to environmental sciences [6]. Their behavior is influenced by factors like ion concentration, type, degree of ionization, concentration and molecular weight. At low ionic strengths, PEs exhibit strong electrostatic interactions, while at high ionic strengths these interactions weaken due to charge screening. The conformation of PEs (rod-like, coiled, etc.) is dictated by these conditions, directly affecting the physical properties of PEs like solubility, charge density and interaction potential with other molecules. Different conformations may then be adopted for specific use and application. Using different techniques, the idea was to bridge the gap between polymers and IDPs, where PSS has a simpler hydrophobic backbone without peptide bond, a larger side group (styrene) and is uniquely charged [7]. While PE is typically built of a single monomer type

with a charge and maybe a hydrophobic backbone like PSS, IDP consists of 21 different amino acids with varying charge and hydrophilicity/hydrophobicity along the chain. The objective was to correlate collective diffusion and self-diffusion with local chain dynamics, thereby enhancing our understanding of hydrodynamic interactions and internal friction within classical PEs.

The second part of the work deals with the phase behavior of PAA mixtures creating PECs and the question how various environmental factors and different PAA impact PEC structure. A striking property of mixing charged PAA is the observation of a high-density droplet phase and the presence of self-assembled dense hexagonal lattices build of parallel α-helices. Thy self-assembly is influenced by factors like PAA molecular weight, concentration and pH, and make PAA mixtures suitable for various applications including drug delivery [8] and tissue engineering [9]. Understanding their phase transition behavior and formation of the droplet phases in response to external stimuli like temperature, pH and ionic strength, is crucial for their effective application. PECs formation and stability are also significantly influenced by external fields: magnetic fields and shear forces, which are less commonly explored in traditional studies. The investigation of these factors provides a deeper insight into the phase transition behaviors of PECs, essential for optimizing their use in practical applications. The structural investigation within droplets reveals formations ranging from crystalline α-helices to amorphous phases, depending on salt concentrations.

Dynamic light scattering (DLS), neutron spin-echo (NSE) spectroscopy, pulsed field gradient NMR (PFG-NMR) spectroscopy, small-angle X-ray (SAXS) and neutron (SANS) scattering, and optical and electron microscopy were used in this work to investigate the structure and dynamics of PEs and PECs in various regimes.

By exploring the dynamics and structure of PEs and PECs, this thesis aims to contribute to the broader understanding of their roles in diverse applications and biological processes, bridging a critical knowledge gap and giving the way for novel applications and deeper scientific insights.

9. Theory

9.1. Polyelectrolytes

Polyelectrolytes (PEs) are a type of polymer that contains ionizable groups along its polymer chain. These groups can either be acidic or basic, which leads to the formation of charged PEs. As a result, PEs possess distinct physical and chemical characteristics, such as aqueous solubility, viscosity and stability. These unique properties make them highly suitable for a wide range of industrial, biological and environmental applications.

The behavior of PEs is strongly influenced by the type and concentration of ions present in solution, as well as by the degree of ionization of PE. The presence of ions in solution affects the behavior of PEs by altering the ionic strength of the solution. Ionic strength is the total concentration of ions in a solution, and it influences the PE stability and charge distributions of PEs. At low ionic strength, PEs tend to be highly charged and exhibit strong electrostatic interactions with other charged chains in the solution. At high ionic strength, the electrostatic interactions between PEs and other ions are weakened, leading to decrease in the degree of ionization and an increase in the solubility of the PE.

9.2. Structure of PEs

The conformation of PEs is influenced by the type and concentration of ions in solution, as well as by the electrostatic interactions between the charged species. The common expectation from the PE's conformation behavior depending on the salt concentration in the solution, which is a combined overview of different papers [6], [10]–[16], is the following: At low salt concentrations the charged side groups repel each other and a rod-like chain conformation for PEs is expected. Adding salt causes electrostatic screening effects. With enough salt, when the electrostatic screening length or Debye length κ is much smaller than chain dimensions, a Gaussian coil conformation is predicted. κ is dependent on ion concentration, with κ^2 proportional to ion concentration [6].

With increasing PE concentration, the chains start to overlap, and a gel is observed. That occurs when the distance between PE chains becomes on the order of their size.

In the intermediate phase between rod-like and a Gaussian coil ion condensation causes partial chain collapsing that results in more compact configuration [17].

The pH of the solution also influences the conformation of PEs. The degree of ionization of the ionizable groups along the polymer chain depends on the pH of the solution and pK_a of the ionizable groups. As the pH of the solution changes, the degree of ionization changes, which in turn affects the net charge of the polymer and the electrostatic interactions between the charged groups.

9.3. Polyelectrolyte complexes

Polyelectrolyte complexes (PECs) are formed by the electrostatic interaction between oppositely charged PEs, resulting in a self-assembled material with unique properties. PECs have attracted considerable attention in recent years due to their potential use in a wide range of applications, such as drug delivery [8], tissue engineering [9] and water treatment [18].

The resulting PEC is a self-assembled material with a complex structure that depends on the properties of the PEs, their concentration and the pH of the solution. Simulations have shown that in aqueous media at room temperature the entropic changes resulting from the release of counterions from the PE chains are the primary driving force for complexation, rather than the enthalpic changes associated with electrostatic attraction [6]. Recently it was also demonstrated that the reorganization of water molecules around the polymer chains during the complexation process also contributes to the entropic forces [6].

PECs have unique properties that make them attractive for a wide range of applications. For example, they are typically insoluble in water, which makes them useful for drug delivery applications, as they can protect a drug from degradation in the body. They also can encapsulate a wide range of molecules, including proteins and nucleic acids, making them useful for different applications.

PECs also have unique mechanical properties, including high elasticity and the ability to form gels and films. These properties make them attractive for use in tissue engineering applications, where they can be used to mimic the structure and function of natural tissues.

9.4. PECs phase transition behaviour and structure

One of the most interesting and important properties of PECs is their phase transition in response to changes in external conditions (such as temperature, pH and ionic strength) and chirality [19] [20] [21].

The phase transition behavior of PECs is closely related to their structure and composition. Typically, PECs exist in a range of phases, including a PE-rich phase, a complex coacervate phase and a PE-lean phase. The phases transform from one to another if external conditions change. The process of forming complexes usually involves an increase in entropy, which happens as counterions are released, ion pairs are created, and water molecules around the complexes rearrange themselves [21].

Salt, respectively ion concentration, plays a crucial role in determining the state of PECs. It is commonly observed that the precipitate in the solution with low salt concentration is dissolving with addition of salt. Sometimes very high salt concentration can also cause secondary aggregation. R. Chollakup et al. studied phase separation and complexation of poly(acrylic acid) and poly(allylamine hydrochloride) [22]. They changed e.g. polyacid/polybase ratio, salt and polymer concentration, pH and temperature. Using optical microscopy, they found different phase behavior of the complexes. At zero salt concentration precipitate was observed. Adding salt caused coacervates (droplets) formation, then with higher salt concentration gel-like behavior can be achieved, and after mixing in sufficient amount of salt the solution gets transparent and contains no more large aggregates. After centrifugation of these samples a white precipitate was observed at law salt concentrations and a highly viscous liquid (coacervate) phase – at medium salt concentrations. They also measured turbidity at different conditions. The main results were that, firstly, a 1:1 anion:cation molar ratio had the highest turbidity due to the strongest PEC formation. Secondly, the change from precipitate to coacervate phase required less salt, but more salt at coacervate-solution transition at 1:1 ratio than at other PE combinations. Thirdly, lower amount of salt was necessary to destroy PECs at higher polymer concentrations. Fourthly, the turbidity was higher at pH=5 than at pH=7 meaning larger aggregates at lower pH due to decreased protonation and less extended coil conformation. Lastly, the secondary aggregation was observed at 50°C at salt concentrations higher than 3M.

Different studies showed for many poly amino acids' (PAAs) mixtures that the greatest formation of PECs occurred at 1:1 ratio in both salted and unsalted systems [23] [24].

One of the most important factors that influence the phase transition behavior of PECs is temperature. As the temperature increases, the PECs can undergo a phase transition from the complex coacervate phase to the PE-rich or PE-lean phase. This phase transition is typically reversible and can be controlled by the temperature of the system.

Changes in pH or ionic strength can cause the PECs to undergo a phase transition, with the nature and extent of the transition depending on the specific PEs involved, their charge density and the conditions of the solution.

To examine PECs structure scattering techniques can be used. At the molecular level, PECs can exhibit a variety of structures, ranging from highly ordered and intertwined networks to more disordered and loosely associated aggregates. These structures arise from the balance between electrostatic attractions, e.g. oppositely charged PE chains or hydrophilic backbones, and repulsive forces due to the presence of solvent and counterions. The resulting complexes can adopt a variety of morphologies, such as core-shell nanoparticles, micelles, vesicles or hydrogels, depending on the specific conditions and the nature of the PEs involved.

H.M. Fares et al. investigated poly(diallyldimethylammonium) (PDADMA)/PSS complex at different KBr concentrations using small-angle neutron scattering (SANS) [25]. For Q values below 0.01 $Å^{-1}$, a small upturn was seen in the 0.2-0.3 μm range that vanished at higher salt concentrations when the coacervates were observed. At the intermediate-Q range a -1.7 slope was observed which is associated with a chain in a good solvent with excluded volume. High-Q peaks resulted from the deuterated PSS interchain interactions, they were observed at low KBr concentrations and shifted to lower Qs with increasing salt content.

Different scattering techniques were used in E. Spruijt et al. paper to study poly(acrylic acid) and poly(N,N-dimethylaminoethylmethacrylate) (PDMAEMA) complexes [26]. Q^{-2} slope was observed for complex coacervates that is a sign of a close to an ideal Gaussian coil conformation. Complex coacervate networks experiments showed structure peaks at SANS and small-angle X-ray scattering (SAXS) which were explained as an ability of PDMAEMA to form micellar structures at high salt concentrations in water. SANS, SAXS and static light scattering showed an upturn at low Q that are referred to density fluctuations on large length scales. The dynamics of these PECs was measured by DLS and showed two modes. The fast mode was attributed to an object of 1-2 nm size which fits to the PEC's mesh size and the slow mode – to 200-500 nm that was related to the density fluctuations observed before.

9.5. Scattering of light, X-rays and neutrons

Different scattering techniques (i.e. light scattering, X-ray and neutron scattering) open possibilities to get information about structural and thermodynamic properties of matter.

In Fig. 1 a typical scattering experiment is shown. An incident beam of intensity I_0 with the wave vector k_i and wavelength λ passes through a sample in the volume V_s and part of the beam is scattered. The intensity $I(Q)$ of the scattered beam with the wave vector k_s varies with the

scattering angle 2θ (the angle between the wave vectors of incident and scattered beams). The scattering vector $\vec{Q}$ is calculated as $\vec{Q} = \overrightarrow{k_s} - \overrightarrow{k_i}$.

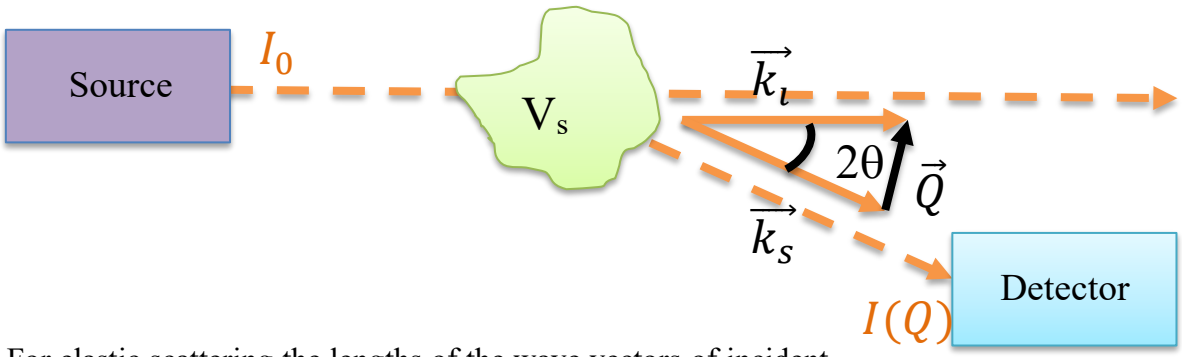

Fig. 1 Typical scattering experiment.

For elastic scattering the lengths of the wave vectors of incident and scattered beams are equal ($|\overrightarrow{k_s}| = |\overrightarrow{k_i}|$) and for quasielastic scattering they have almost the same lengths ($|\overrightarrow{k_s}| \approx |\overrightarrow{k_i}|$). For this reason, in both cases the scattering vector Q is:

$$Q = |\vec{Q}| = \frac{4\pi}{\lambda} n \sin(\theta) \qquad (1)$$

n is the refractive index of the sample (n=1 for X-rays and neutrons) [27].

In light scattering experiments, a beam of light is directed onto the sample, and the scattered light is collected and analyzed. A typical wavelength is 633 nm of a HeNe laser. By measuring the intensity and angle of the scattered light, valuable information about the size, shape and interactions of the scattering particles can be obtained. Light scattering techniques, such as dynamic light scattering (DLS) or static light scattering, are commonly used to determine the hydrodynamic radius, aggregation behavior and polydispersity of PEs and PECs in solution. X-ray scattering is a widely employed technique for studying the structure of materials. X-rays have a much shorter wavelength than visible light, e.g. 0.154 nm for Cu K_α line, allowing for the investigation of smaller length scales. Small-angle X-ray scattering (SAXS) provides information about the spatial arrangement and distribution of particles within the PECs, while wide-angle X-ray scattering can reveal details about the crystalline or semi-crystalline structures present in the complexes. X-ray scattering experiments can also be combined with other techniques, such as differential scanning calorimetry, to study the thermal behavior and phase transitions of PECs.

Neutron scattering is particularly useful for studying the structure and dynamics of polymers and PECs due to the strong interaction of neutrons with hydrogen, which is abundant in organic

compounds. Neutrons can penetrate deep into samples, allowing for the investigation of bulk properties and intermolecular interactions. Small-angle neutron scattering (SANS) provides information about the size, shape and organization of PECs at the nanoscale, while neutron spin-echo (NSE) spectroscopy can probe the dynamics and segmental motion of the polymer chains within the complexes. Typical wavelengths are 0.4-0.6 nm for SANS and 0.6-1.6 nm for NSE.

By utilizing scattering techniques, researchers can gain valuable insights into the structural arrangement, morphology and behavior of PEs and PECs at different length scales and under various experimental conditions. This information is crucial for understanding their fundamental properties and designing tailored materials for specific applications.

9.6. Small-angle scattering (SAXS & SANS)

The usual size of the objects or particles measured by SAXS and SANS is between ≈0.5 nm and a few hundreds of nm and they are investigated at the angles 2θ from close to 0° to 10°. Small-angle scattering involves measuring the interference between neutrons (SANS) or photons (e.g. SAXS) scattered by atoms in the direction of the scattering vector Q [28]. The measured intensity contains both coherent and incoherent parts (incoherent is neglected for X-rays) and is defined as a macroscopic cross section $\frac{d\Sigma}{d\Omega}$:

$$I_{measured}(Q) = \frac{d\Sigma}{d\Omega} = I_{coh}(Q) + I_{incoh} + bgr \qquad (2a)$$

with bgr – background.

The coherent and incoherent parts of the scattering refer to different contributions to the total scattering intensity. The coherent part arises from the interference between scattered waves and provides information about the spatial arrangement and interactions of particles within the sample. Coherent scattering provides the main information we often seek in SAXS or SANS experiments, such as particle shapes, sizes, and distributions. Incoherent scattering arises from the independent scattering of individual atoms or groups, where the scattered waves do not interfere constructively or destructively. It provides no useful structural information since it's not sensitive to the relative positions of the scatterers. For X-rays, the incoherent scattering, e.g. Compton scattering, is usually much smaller than the coherent scattering, so it's often neglected. For neutrons, incoherent scattering can be significant, particularly for certain types of atoms (like hydrogen) or at larger scattering vectors.

The incoherent part essentially contributes as a kind of "background noise" to the scattering pattern for SANS.

In the ideal case of isotropic and identical particles I_{coh} can be separated like

$$I(Q) = I_{coh}(Q) = \frac{N}{V} S(Q,c) P(Q) \tag{2b}$$

With N – number of particles in the volume V, $S(Q,c)$ structure factor (SF) describing interparticle interactions and $P(Q)$ as form factor (FF). $S(Q,c)$ depends on the concentration of the particles $c = N/V$ and the interaction between the particles. $S(Q,c)$ is also related to the spatial particle distribution via a Fourier transform of the radial distribution function $g(r)$. The spatial organization inside a particle is described by $P(Q)$, which includes details about the particles' dimensions, morphology, and internal characteristics. We find

$$\begin{aligned} P(Q) &= \langle \sum_{i,j} b_i b_j e^{iQ(r_i - r_j)} \rangle \\ S(Q) &= \frac{1}{N} \langle \sum_{n,m} e^{iQ(R_n - R_m)} \rangle \end{aligned} \tag{3}$$

where b_i is the scattering length of atom i at position r_i relative to the particle center of mass, $\langle\,\rangle$ mean ensemble average. According to Babinets principle, b_i can be replaced by the contrast if a solvent is assumed, thus $b_i \to b_i - V_i \rho_s$ with $V_i \rho_s$ as the displaced solvent scattering length with V_i – displaced volume and ρ_s – solvent scattering length density.

Both FF and SF can be separated from measurements at different concentrations by extrapolating $P(Q)$ to zero concentration with $S(Q,0) = 1$ and then calculating $S(Q,c) \sim I(Q,c)/P(Q)$.

Approximations related to the FF allow a first examination of experimental data. The pair distance distribution function between atoms inside a particle is

$$p(r) = \frac{r^2}{2\pi^2} \int_0^\infty Q^2 I(Q) \frac{\sin Qr}{Qr} dQ \tag{4}$$

Using the approximation that for $Q \to 0$ $\frac{\sin Qr}{Qr} \approx 1 - \frac{(Qr)^2}{3}$, one gets a simplified formula, the Guinier model, that is valid at $Q < 1.3/R_g$:

$$I(Q) = I(0) e^{-\frac{1}{3} R_g^2 Q^2} \tag{5}$$

where $I(0)$ is the forward scattering intensity $I(0) = (\Delta\rho)^2 V^2$ for homogeneous particles and R_g is the radius of gyration:

$$R_g = \frac{\int r^2 p(r) dr}{2 \int p(r) dr} \tag{6}$$

Equation (5) is important in the beginning of SAXS data analysis, as a so-called Guinier plot ($\ln(I(Q))$ as a function of Q^2), which presents a linear dependence from which forward scattering intensity $I(0)$ and the radius of gyration R_g can be easily extracted. From an absolute value of $I(0)$ one can also calculate the molecular mass of an object [29].
For some particles R_g is calculated from geometrical characteristics [30]:

- Spherical particle: $R_g = \sqrt{\frac{3}{5}}R$
- Solid ellipsoid (a, b, c – half axes): $R_g = \frac{1}{\sqrt{5}}\sqrt{a^2 + b^2 + c^2}$
- Solid rod (L – length, R – cross-section radius): $R_g = \sqrt{\frac{L^2}{12} + \frac{R^2}{2}}$

A useful tool to look at the compactness of the studied particle is the so-called Kratky plot $I(Q) * Q^2$ vs. Q. When in this plot a plateau at high Q values is observed, a Gaussian chain conformation is predicted (see later) for the polymer according to the high Q limit $\sim Q^2$, while a more compact structure, like a collapsed polymer or sphere, will show a distinct maximum on a Kratky plot [31].

9.6.1. Form factor

Form factor of identical particles is calculated using Equation (3).
For a simple case – a sphere – an analytical form can be found as

$$P(Q) = \rho^2 V^2 \left(\frac{\sin(QR) - QR * \cos(QR)}{(QR)^3}\right)^2 \quad (7)$$

with contrast ρ and volume $V = \frac{4}{3}\pi R^3$ of a sphere. The sphere FF is plotted at Fig. 2 in normalized coordinates. At $qR < 1$ a Guinier region is shown and a Q^{-4} envelop at high Qs is observed (Porod scattering).

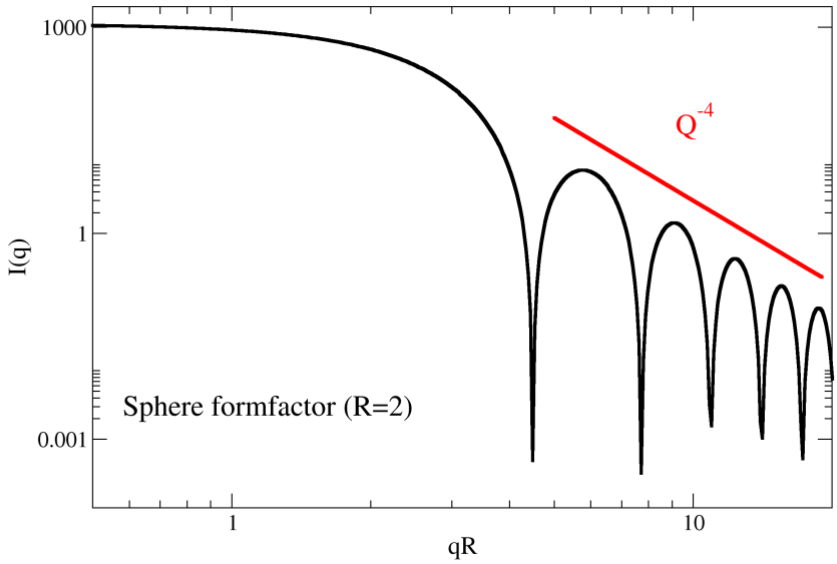

Fig. 2 Sphere formfactor.

Chainlike macromolecules, like polymers, are usually represented as Gaussian chains within a bead-spring model of N elements of length l for which the probability that the distance between distant segments i and j ($|i-j|>30$) is given by the Gaussian distribution [32]. The end-to-end distance for them is calculated as $\langle r_{ee}\rangle = \sqrt{N}l$ and the radius of gyration $R_g = \sqrt{N}l/\sqrt{6} = \langle r_{ee}\rangle/\sqrt{6}$.

The FF of a Gaussian chain is introduced by Debye for an ideal Gaussian chain [33]

$$P(Q) = \frac{1}{Q^4 R_G^4}\left(e^{-Q^2R_G^2} - 1 + Q^2R_G^2\right) \tag{8}$$

This can be generalized to expanded or collapsed chains with $\nu \neq 0.5$ [33]:

$$P(Q) = \frac{1}{\nu U^{\frac{1}{2\nu}}}\gamma\left(\frac{1}{2\nu}, U\right) - \frac{1}{\nu U^{\frac{1}{\nu}}}\gamma\left(\frac{1}{\nu}, U\right) \tag{9}$$

where γ is an incomplete gamma function and $U(Q,\nu) = \frac{Q^2R_G^2(2\nu+1)(2\nu+2)}{6}$.

9.6.2. Structure factor

When particles are uncorrelated, $S(Q) = 1$. The correlation between the particles appears due to attraction (e.g. aggregation) or repulsion (a mean distance with small variance). This results in oscillations that appear in the low Q region and constant S(Q) at high Q where the inner structure of the particles is visible.

When the concentration of the solution is high enough for particles to “feel” each other, structure factor effect should be considered [30] (Equation (3)).

For charged particles the rescaled mean spherical approximation (RMSA) SF of Hayter-Penfold describing a fluid structure is often used [34]. It describes a particle with charges at the surface and ions in solution screening the surface charge leading to a Yukawa type potential:

$$\begin{cases} U(r) = \infty, & r < 1 \\ U(r) = \dfrac{\gamma e^{-kr}}{r}, & r > 1 \end{cases} \tag{10}$$

$1/k$ is the screening length, which is related to the ion concentration, and the surface potential γ is determined by the surface charge and defined as $\gamma = L_B(XZ_0)^2/\sigma_0$ (L_B – the Bjerrum length, X – the coupling parameter, Z_0, σ_0 - macroion charge and macroion diameter, respectively) [35]. RMSA SFs at $k = 0{,}2$ and $k = 1$ are shown in Fig. 3.

When the interparticle potential contains a short-range attraction and a long-range repulsion parts, two Yukawa potential in the mean spherical approximation is used as a SF [36]:

$$\frac{\mathrm{V}}{k_B T} = \begin{cases} \infty, & 0 < r < 1 \\ -K_1 \dfrac{e^{-Z_1(r-1)}}{r} - K_2 \dfrac{e^{-Z_2(r-1)}}{r}, & r > 1 \end{cases} \tag{11}$$

where r is scaled to have a hardcore diameter equals 1 and $Z_i = \frac{1}{\rho_i}$ (ρ – scattering length density). Fig. 4 shows the resulting SF for different K_1 values presenting a cluster peak dependent on the attractive component.

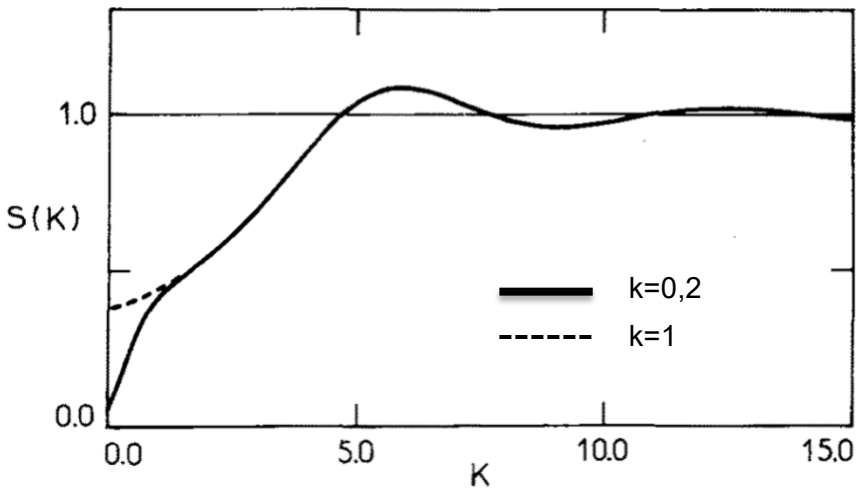

Fig. 3 RMSA SFs at $\gamma = 0{,}2$ and the volume fraction $\eta = 0{,}1$. Taken from the work of J. P. Hansen and J. B. Hayter [34].

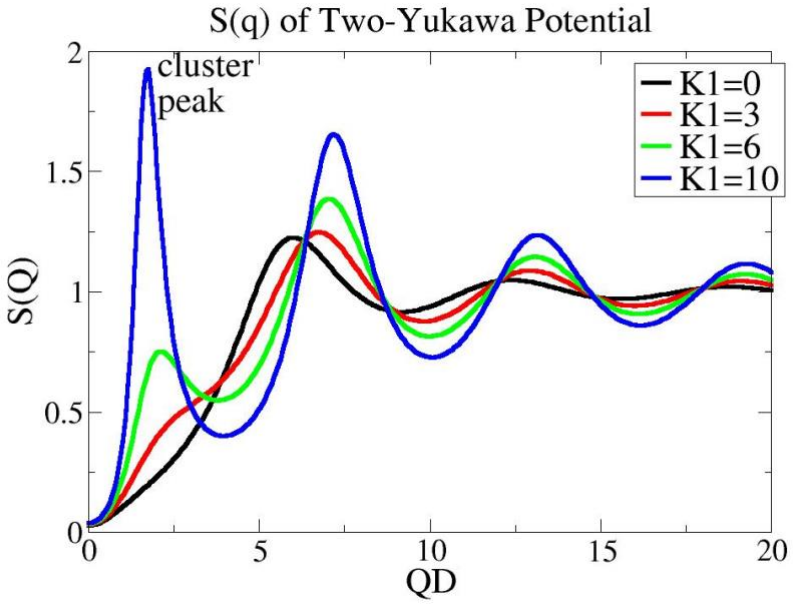

Fig. 4 Two Yukawa potential for particle radius $R = 0.5\ nm, K2 = -kT, \rho_1 = 0.1\ nm, \rho_2 = 2\ nm$. $K1$ is in kT units. Taken from Jscatter examples [37].

9.6.3. Crystal structure

A crystal is characterized by a repeating three-dimensional arrangement of atoms or molecules. The unit cell is the basic building block of a crystal lattice, representing the smallest repeating unit that retains the overall symmetry and structure of the crystal. It serves as a fundamental reference frame for describing the crystal's arrangement and properties. The unit cell is defined by its lattice parameters, which include the lengths of its edges and the angles between them.

To separate the SF of isotropic scattering particles in a crystal domain, a correction term $\beta(Q)$ is required (due to particles polydispersity and anisotropic shapes) [38]:

$$\beta(Q) = \langle F(Q)\rangle^2 / \langle F^2(Q)\rangle \tag{12}$$

where $F(Q)$ is scattering amplitude.

Then the crystal SF can be calculated as [39]:

$$S(Q) = 1 + \beta(Q) * (Z_0(Q) - 1) * DW(Q) \tag{13}$$

where $DW(Q)$ is Debye Waller factor ($DW(Q) = e^{-\sigma_a^2 a^2 Q^2}$, a – the distance to the nearest particle, σ – polydispersity). Lattice factor $Z_0(Q)$ for an ideal undistorted lattice with (hkl) Miller indices for a given crystal lattice plane can be expressed as:

$$Z_0(Q) = \frac{(2\pi)^{d-1} c}{n v_d Q^{d-1}} \sum_{hkl} m_{hkl} f_{hkl}^2 L_{hkl}(Q) \tag{14}$$

Here n – number of particles per unit cell, v_d – volume ($d = 3$) / surface area ($d = 2$) / length ($d = 1$) of the d-dimensional unit cell, f_{hkl} – unit cell SF, m_{hkl} – peak multiplicity, $L_{hkl}(Q)$ – normalized peak shape function and c – Porod constant ($c \approx 1$).

If the lattices are composed of anisotropic particles with strong orientation, the SF can be calculated using only $Z_0(Q)$ and with a unit cell of dummy atoms. As a result, $S(Q)$ will represent the FF amplitude in the direction of Bragg peaks.

f_{hkl}^2 should be 1 at $Q \to \infty$, then we get for atom i in a unit cell having coordinates (x_i, y_i, z_i) and scattering amplitude b_i:

$$f_{hkl}^2 = \left(\sum_i b_i e^{-2\pi(hx_i + ky_i + lz_i}} \right)^2 / \sum_i b_i^2 \tag{15}$$

When SAXS is applied to crystalline structures, the ordered arrangement of atoms or molecules leads to the presence of peaks in the scattering pattern [39][40]. These peaks, also known as Bragg peaks, arise due to the constructive interference of X-rays scattered by the periodic lattice planes in the crystal as described above. The positions, intensities, and shapes of these peaks allow to extract the crystal's unit cell dimensions, symmetry, and overall structure inside the unit cell.

By analyzing the positions of the peaks in the SAXS pattern, the lattice spacings d in the crystalline structure can be determined using Bragg's law:

$$n\lambda = 2d \sin\theta \tag{16}$$

where n is an integer (the order of the reflection), λ is the wavelength of the X-rays, d is the lattice spacing, and θ is the scattering angle. The intensities of the peaks can provide information about the atomic positions within the unit cell and the overall electron density distribution.

In certain cases, molecules or atoms can form ordered structures along planes presenting different length scales perpendicular and parallel to the planes as lamellar crystals. These lamellar crystals exhibit characteristic peaks in SAXS at low-Q values. The position and intensity of the low-Q peak provide information about the periodicity and ordering of the planar structure.

As an example, the SF of a hexagonal lattice filles with long cylinders is shown on Fig. 5, where both low- and high-Q peaks are visible. Hexagonal lattices are a common type of two-dimensional crystal structure. They exhibit distinctive peaks in the SAXS pattern at high-Q values. The position and intensity of the high-Q peak provide information about the spacing between lattice points in the hexagonal lattice.

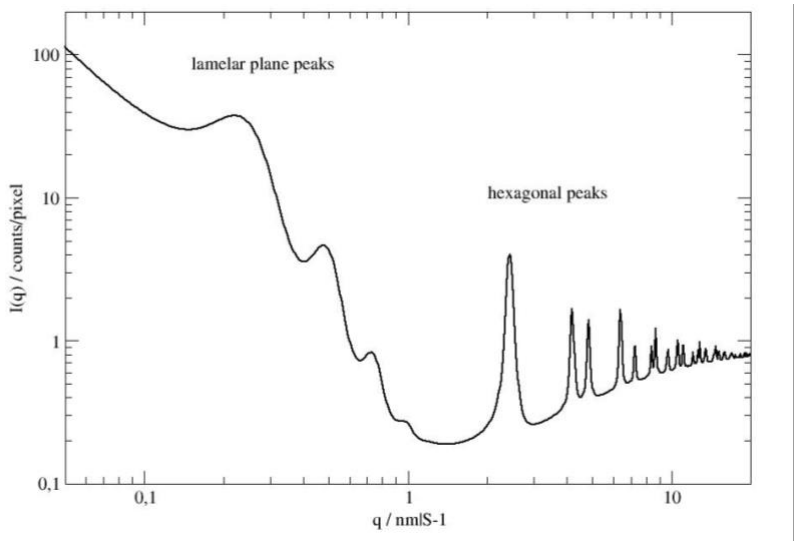

Fig. 5 SF of a hexagonal lattice filled with long cylinders. Taken from Jscatter examples [37].

9.7. Polymer dynamics

9.7.1. Dynamics of polymer chains in solution

In the context of single polymer chain dynamics in solution, various factors such as additional hydrogen bonding, dipolar interactions, ion condensation and chain connectivity can influence the collective behavior of polymer chains. These interactions have an impact on macroscopic properties like viscosity, turbidity, collective diffusion and surface interactions. The relationship between self and collective diffusion coefficients (D_s and D_c), radius of gyration (R_g) and viscosity (η) is described by Zimm dynamics for neutral polymers [41] or for PEs by models, such as the double screening model of Muthukumar [42] and the scaling model of Dobrynin [43], which consider electrostatic screening, excluded volume effects and hydrodynamic interactions (HIs). Scaling laws exhibit different behaviors depending on salt concentration, polymer concentration regime (dilute, semi dilute or entangled) and assumptions about hydrodynamic screening between chains [44]. Experimental data generally agree with these power laws, although some discrepancies have been reported [45]–[47].

The dynamics of a neutral polymer chain at the molecular level can be described theoretically as either Rouse-like, assuming hydrodynamic screening, or Zimm-like, considering the

relevance of hydrodynamic interactions [41], [42], [48]. To gain direct insight into the dynamics of PEs at the molecular level, neutron spin echo (NSE) spectroscopy is employed. This unique technique enables the investigation of polymer chains on the nanometer and nanosecond scales. While NSE spectroscopy has been widely used to study polymer dynamics, protein domain motions and IDPs, its application to PE dynamics is relatively limited [7], [28], [49]–[53].

The dynamics of polymer chains plays a crucial role in determining the physical and mechanical properties of polymer materials, such as their elasticity, viscosity and response to external stimuli. By studying the dynamics of single polymer chains, researchers can gain insights into the behavior of macromolecules in solution, which has implications in polymer processing, drug delivery systems, biomaterials and many other areas.

9.7.2. Dynamics of PEs

The conformation and chain mobility of PEs both influence the ability of the polymer chains to move and fluctuate in solution. They are both dependent on various conditions, including ionic strength and pH of the solution, the type and concentration of ions, the type of ionizable groups along the polymer chain and the electrostatic interactions between the charged parts.

The HIs between the polymer chains can also influence their chain mobility. HIs are caused by the motion of the solvent around the chains and can restrict their movement, reducing their mobility. The magnitude of these interactions depends on the size and shape of the polymer and the viscosity of the solvent.

Hayter et al. focused on PSS as a representative example of classical PEs and explored the correlation between the diffusion coefficient ($D(Q)$), single chain mobility ($\mu(Q)$) and the SF ($S(Q)$) of the PE at low salt concentration [49]. They established the relationship $D(Q) = kT\mu(Q)/S(Q)$, which connects the observed collective diffusion to the forces ($kT/S(Q)$) acting between particles or chains, as reflected in $S(Q)$. This correlation is associated with the phenomenon known as “de Gennes narrowing”, which describes the reduced mobility observed at the peak of the correlation function. Here, kT represents the thermal energy.

In the case of colloidal spherical particles, Ackerson et al. introduced the concept of reduced mobility at higher particle concentrations [54]. Subsequently, the $\delta\gamma$-expansion by Beenakker and Mazur quantified this effect and introduced the hydrodynamic function $H(Q)$, which describes the decreased mobility of hard spheres as the concentration increases. $H(Q)$ splits into two parts: a Q-dependent distinct part ($H_d(Q)$) and a self-part representing the reduced

self-diffusion (D_s/D_0) [55], [56]. This formulation led to the well-known correction $D(Q) = D_0 H(Q)/S(Q)$, where D_0 denotes the diffusion coefficient of a single particle. Although originally derived for spheres, this correction has been found applicable to other systems such as globular proteins, highly anisotropic proteins like antibodies, and IDPs [50], [57]–[64].

Zimm dynamics

The Zimm model is a theoretical model that provides a simple description of the dynamics of PEs [65]. It is a bead-spring model, which is a coarse-grained description of the dynamics of polymers in solution including HIs. Specifically, it describes a chain made up of N beads that are connected by entropic springs, with each bead spaced apart by a distance l (Fig. 6).

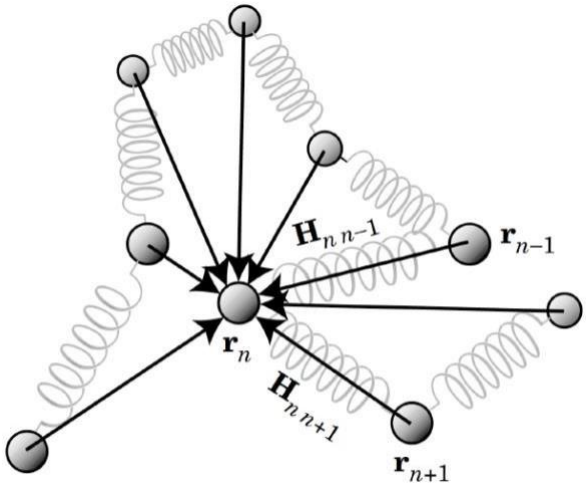

Fig. 6 Zimm model representation of the polymer. Taken from the work of I. Teraoka [66].

The Zimm model involves different relaxation modes with different mode numbers (p) and characteristic times (τ_p), which describe the chain's internal motions including rotational diffusion. The equation used to calculate the characteristic times of the different relaxation modes is [41]:

$$\tau_p = \frac{\eta R_e^3}{\sqrt{3\pi} k_B T} p^{-3\vartheta} \tag{17}$$

with η – solution viscosity, R_e – end-to-end distance $R_e = \sqrt{(2\nu+1)(2\nu+2)} R_G$, k_B – Boltzmann constant, T – temperature and ϑ describes solvent quality. The dynamic SF is calculated as:

$$I(q,t) = \frac{\exp\left(-q^2 D_{Zimm}\tau\right)}{N}\sum_{n,m}^{N}\exp\left(\frac{-q^2 B_{n,m}(\tau)}{6}\right) \tag{18}$$

$$B_{n,m}(\tau) = |n-m|^{2\nu}l^2 + \\ +\frac{4R_e^2}{\pi^2}\sum_{p=0..\infty}\frac{A_p}{p^{2\nu+1}}\cos\left(\frac{\pi p n}{N}\right)\cos\left(\frac{\pi p m}{N}\right)\left(1-e^{-t/\tau_p}\right) \tag{19}$$

where $l = \sqrt{\frac{R_e^2}{N^{2\nu}}}$.

The Zimm model provides a simple expression for the center of mass diffusion coefficient of a polymer chain, $D_z = 0.196k_bT/(\eta R_e)$, which is a measure of its mobility in solution.
This model is a simple, idealized model that has several limitations, that, for example, it does not account for the specific interactions between the charged groups along the chain, such as electrostatic and hydrodynamic interactions and internal friction of the chain. To take the last one into account, the extended Zimm model with internal friction (ZIF) can be used.

Zimm model with internal friction

ZIF model extends the original model and includes a relaxation time τ_i that is added to each Zimm mode (Equation (18)) to account for internal friction: $\tau_p^{ZIF} = \tau_p + \tau_i$ [67], [68]. Internal friction is represented as polymer's resistance to steric hindrances [67] (**Error! Reference s ource not found.**).

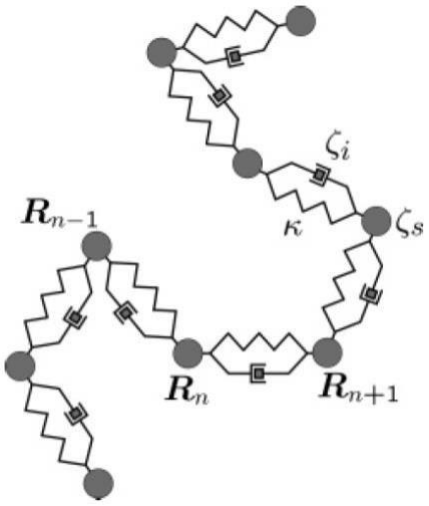

Fig. 7 Polymer chain in ZIF representation where beads are connected with springs and internal friction between the elements is also implemented. Taken from the work of B. S. Khatri and T. C. B. McLeish [67].

The model with internal friction incorporates the internal friction of the polymer chain into the expression for the diffusion coefficient. This is achieved by introducing a friction coefficient, which represents the internal friction between neighboring segments of the chain. The friction coefficient is proportional to the temperature, the length of the chain and the inverse of the persistence length.

9.7.3. Concentration effects on dynamics

For non-spherical particles or polymers, the hydrodynamic radius r_H is equal to the radius of a sphere showing the same translational diffusion coefficient. This radius depends on the particle's structure, surface and ions around in the solution but not on the interaction between the particles [69].

During measurements only in the dilute limit particle interactions can be neglected. Therefore, the measured diffusion coefficient D is corrected according to [70]:

$$D = D_0 \frac{H(q)}{S(q)} \tag{20}$$

with the SF $S(q)$ and the hydrodynamic function $H(q)$. The SF can be measured (e.g., using SAXS) and depends for charged systems also on salt concentration. The hydrodynamic function for polymers is related to the intrinsic viscosity and shows a reduction with increasing the concentration of the particles. As the concentration of particles or polymers increases, their mutual interactions become more significant, leading to deviations from ideal behavior. These interactions can give rise to changes in the diffusion behavior, viscoelastic properties and even the overall phase behavior of the system.

10. Methods

10.1. Small-angle scattering instruments

10.1.1. Collimation

In Fig. 8 a scheme of a typical small angle scattering instrument is presented [71]. In general, there are two types of instruments that have either point- or line-collimation system (see Fig. 9). In the first type pinholes are used to collimate the beam. Line collimation systems use rectangular slits. They have the advantage of having higher flux and the possibility to measure

at larger sample volumes, but only isotropic systems can be studied [72]. The disadvantage is that desmearing must be applied. Desmearing involves applying algorithms, such as the Lake algorithm, to reconstruct the scattering data and account for the effects of the line collimation. This correction ensures accurate interpretation of the scattering pattern and facilitates comparison with theoretical models [73].

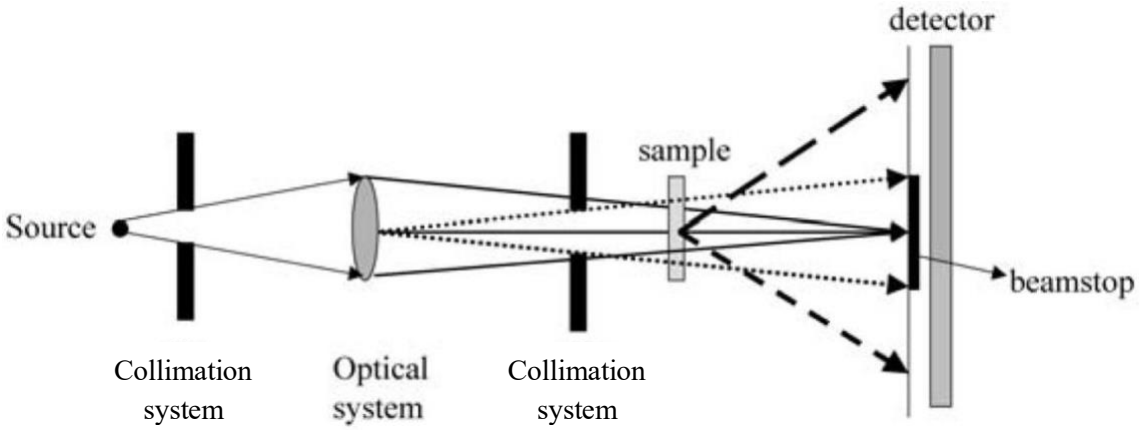

Fig. 8 A scheme of a SAXS/SANS instrument and a beam propagation. Monochromator or mirror are used in the optical system in SAXS. Taken from the work of M. H. J. Koch et al. [71].

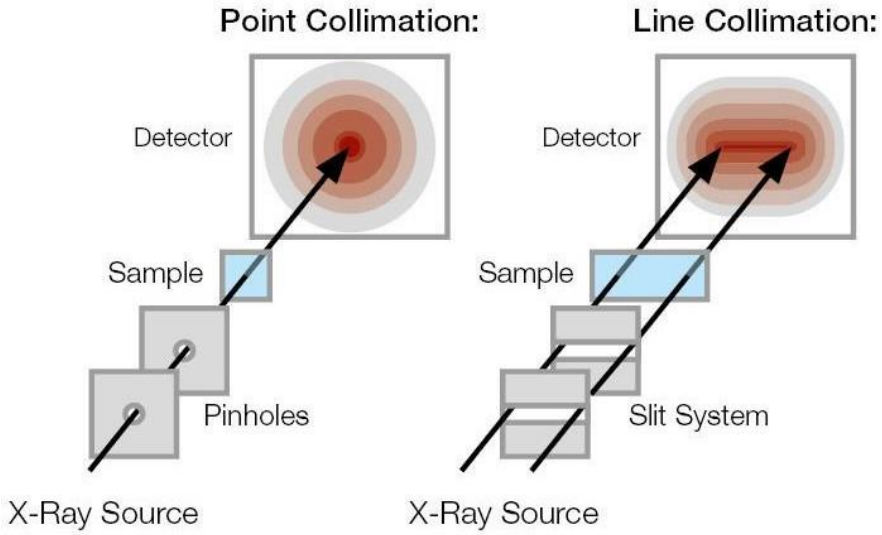

Fig. 9 Two types of collimation systems in SAXS instruments. Taken from H. Schnablegger and Y. Singh, "The SAXS Guide" [72].

10.1.2. Small-angle X-ray scattering

Small-angle X-ray scattering (SAXS) is widely used for studying the structure of different molecules in solution. During SAXS measurement the sample can be investigated both in the

solution or in a crystallized state, and the received signal, which is the function of the scattered intensity on the scattering angle, is the characteristic of the molecules' size, shape and internal structure [74]. SAXS instruments show only small smearing that often it is neglected.

X-rays interact with the electrons of the sample. During scattering of a monochromatic plane wave an electron starts to oscillate and a monochromatic wave with the electric field intensity $E = E_0 e^{i(\boldsymbol{k}_i \boldsymbol{r} - \omega t)}$ is sent out with the amplitude:

$$E_s = -E_0 \frac{e^2}{mc^2} \frac{1}{r} \sin\psi \tag{21}$$

where e, m – charge and mass of the electron, c – light velocity in vacuum, r – distance from the electron and ψ – angle between the scattered beam and the direction of the electron acceleration. Thus, the scattering length of X-rays would be:

$$b_x = \frac{e^2}{mc^2} \sin\psi = r_0 \sin\psi \tag{22}$$

where $r_0 = \frac{e^2}{mc^2} = 2.82 * 10^{-13}\ cm$ – the Thomson radius. As a result, the scattering intensity (the differential cross section) of one electron can be calculated:

$$i_x = b_x^2 = r_0^2\ sin^2\ \psi \tag{23}$$

For SAXS $\psi = 90°$, so $i_x \approx r_0^2 = 7.95 * 10^{-26} cm^2$.

The integral cross section would then be:

$$\sigma_x = \frac{8\pi}{3} r_0^2 = 6.66 * 10^{-25} cm^2 \tag{24}$$

An atom with N_e electrons has a scattering length $b_x = N_e r_0$ [32].

The collimation length in SAXS instruments refers to the distance between the X-ray source and the sample. This distance can vary from tens of cm to several meters depending on the specific SAXS instrument and experimental requirements. Adjusting the collimation length in SAXS experiments allows researchers to control the resolution and the Q range of the experiment.

SAXS experiments were done at the institute-based (located at JCNS-1/IBI-8, FZJ, Julich, Germany) GANESHA instrument (Xenocs, Grenoble, France) or SAXSpace (Anton Paar, Graz). At GANESHA the PECs samples were put into 2 mm capillaries and were measured vertically at different detector distances. SAXSpace is a line collimated system (Kratky camera) which allows to measure at short times. Samples were put into quartz capillaries with diameter of 1 mm and were measured at 20°C for 1-5 hours depending on the PE concentration.

10.1.3. Small-angle neutron scattering

Small-angle neutron scattering (SANS) uses a neutron beam. This difference in radiation type provides complementary information and enables the study of specific features that may not be easily accessible with X-rays. Neutrons have no charge, and they interact with atoms via nuclear forces (short range forces), which allow them to penetrate the investigated material, e.g. soft matter, better than X-rays, and can go through it with less absorption and no radiation damage [75].

In a SANS experiment a beam of neutrons (wavelength band of typical 10% width) is directed at the sample, and the scattered neutrons are detected. The contrast in the scattering pattern arises mainly from hydrogen atoms resulting in the differences in the neutron scattering length density between the sample components [76]. There are two main methods using these differences: contrast variation and selective deuteration. The first one means changing of H_2O/D_2O ratio in solvents, and the second one – deuteration of all or parts of the sample itself. The ability to perform contrast variation using hydrogen H and deuterium D isotopes is one of the key advantages of SANS. This is particularly useful for studying complex systems where different components within the sample can have similar scattering lengths. By selectively replacing H atoms with D in specific parts of the sample, one can enhance or suppress the scattering contrast between different components, making it easier to resolve their individual contributions to the scattering.

SANS instruments have a pinhole collimation, where the beam is collimated by a series of small diaphragms and slits before reaching the sample. This allows to define the beam's size and divergence, ensuring that the scattering is collected with high resolution and minimal background noise. The collimation length is typically between 2 to 40 meters, depending on the desired resolution and the size of the features being investigated. Shorter collimation lengths provide access to larger Q, allowing the study of smaller structures, while longer ones give access to smaller Q, enabling the investigation of larger structures in the sample.

The integral cross section of neutrons is defined as

$$\sigma_n = 4\pi b_n^2 \tag{25}$$

SANS measurements were performed at small-angle neutron diffractometer KWS-2 (MLZ, Garching, Germany) [77]–[79]. The program QtiKWS provided by JCNS was used to convert the SANS data into absolute intensities [80]. All further analysis, such as background subtraction and concentration scaling, was performed using Jscatter [37].

10.2. Neutron spin echo to measure polymer chain dynamics

To investigate polymer movements in the 1-500 ns short time range, high-resolution methods are essential. Neutron spin echo (NSE) is a technique capable of directly measuring minor energy shifts in neutron velocity due to inelastic scattering, permitting access to time scales of several tens of nanoseconds and measuring collective diffusion (like DLS but at shorter times) [28], [50], [81]. Similar to SANS, NSE is mainly performed at small Qs (from around 0.2 to 4 nm^{-1}) which correspond to larger length scales in the sample (from around 1 to 100 nm). These length scales are relevant for studying PEs, PECs, colloids and other biological macromolecules.

Unlike other quasielastic neutron scattering approaches, NSE utilizes the Larmor precession of the neutron spin in an external magnetic field to gauge the velocity changes between incident and scattered neutrons. Each neutron's measurement is conducted individually, enabling a direct comparison of velocities before and after scattering and the determination of velocity differences due to the scattering process. Consequently, NSE can achieve energy resolutions of approximately 10^{-5}, independent of the incident beam's wavelength, allowing the use of a wide neutron spectrum with a typical 10-20% bandwidth.

Fig. 10 depicts the NSE spectrometer's experimental setup. A velocity selector in the primary neutron beam selects a wavelength range with an approximate 20% width. The spectrometer includes a primary and a secondary neutron flight path that pass-through precession solenoids 1 and 2. Prior to entering the first flight path, a supermirror polarizer polarizes the neutron beam in the forward direction. A first π/2 coil rotates the polarization in the x direction, perpendicular to the propagation direction. Each neutron processes in the precession fields without the π-coil's influence, resulting in a phase angle φ. Due to the wide range of neutron wavelengths, the phase angle for each neutron would differ in front of the second π/2 coil, leading to complete beam depolarization. However, the π-coil, accurately positioned at half the field integral value, counteracts this effect. As the neutron spin traverses the phase angle $\varphi = 2\pi n + \Delta\varphi$, the π-coil effect transforms the angle $\Delta\varphi_1$ to $-\Delta\varphi_1$. In a symmetrical configuration where both field integrals in front of and behind the π-coil are identical, the neutron spin passes through a second phase angle $\varphi_2 = \varphi_1 = 2\pi n + \Delta\varphi_1$. Therefore, the spin transformation at the π-coil compensates for the angles $\Delta\varphi_1$, and in front of the second π/2 coil, the neutron spin points in the x direction once more, irrespective of the velocity. This phenomenon is referred to as spin focusing or spin echo.

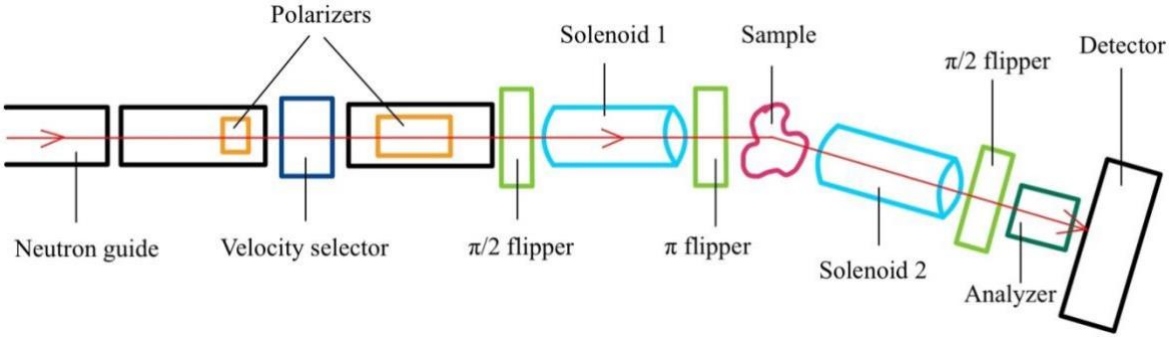

Fig. 10 Representation of the NSE spectrometer. Drawn based on [81]

After projecting the x component of polarization in the z direction with the second π/2 coil, the subsequent supermirror analyzer and detector analyze it. In NSE experiments, the sample is placed near the π-coil, and the polarization is preserved in the case of elastic scattering, except for some losses due to field inhomogeneities. However, if the neutron energy changes because of inelastic scattering processes in the sample, the neutron wavelength alters from λ to $\lambda + \delta\lambda$, and the phase angles φ_1 and φ_2 are no longer compensated. As a result, the second π/2 coil only projects the x component of polarization from a general direction in the z direction.

In order to acquire the normalized intermediate scattering function (ISF) $I(Q,t)/I(Q,0)$, the residual elastic signal and fast dynamics from the solvent are eliminated via background subtraction. The resulting scattering function should start at a value of 1 and display space and time dependent correlation functions originating from the sample. For precise background correction in polymer and protein solutions, it is important to dialyze them and utilize the dialysate for background measurement, considering the exchanged hydrogen [28].

NSE measurements were conducted at NSE instrument IN15 (ILL, Grenoble, France) [82].

10.3. Complementary methods

10.3.1. Dynamic light scattering

Dynamic light scattering (DLS), also called photon-correlation spectroscopy, was already developed more than 100 years ago [83]. Light scattering in general means interaction of light (as electro-magnetic field) with a particle or molecule. DLS has advantages to be non-invasive and non-destructive and is used for measuring dynamic constants, for example, diffusion coefficients, of macromolecules and particles in different solvents. This allows then to get e.g. the size distribution of an observed particle [84]. DLS is sensitive to short timescales, typically

ranging from microseconds to seconds, making it suitable for studying rapid molecular and particle collective diffusion.

Particles in a solution undergo a constant Brownian motion (Fig. 11a), thus spatial position changes of the particles result in fluctuations of the scattering intensity (Fig. 11b). By measuring a correlation function (Fig. 11c) of intensity fluctuations the diffusion coefficient can be obtained [85].

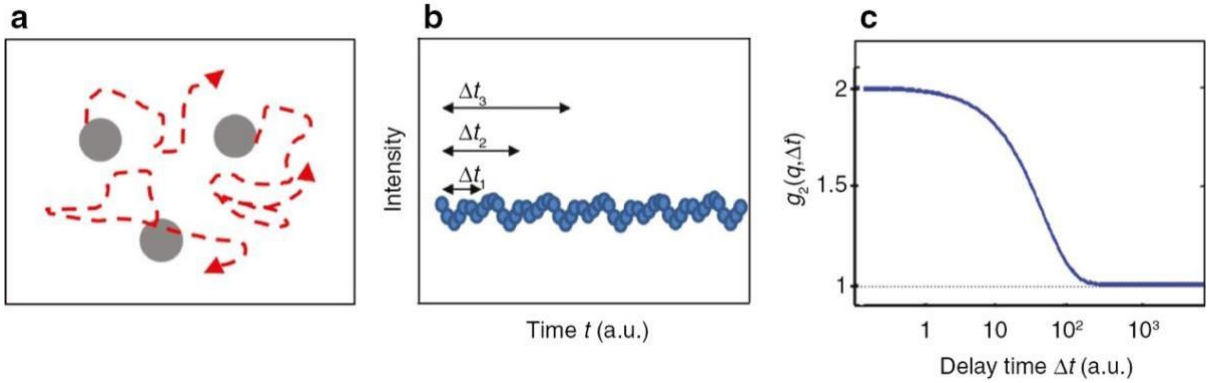

Fig. 11 The sequence of getting information during the DLS measurement. Taken from the work of B. Fischer and V. Abetz [27].

The main components of a DLS instrument are shown in Fig. 6. A laser illuminates the sample. The scattered light is detected by a photon counting device (e.g. avalanche photodiode). A correlator calculates the intensity correlation between two signals (cross correlation) or the same one (autocorrelation) at different lag times τ. The intensity autocorrelation for a signal $I(q,t)$ is:

$$g^2(q,\tau) = \lim_{T\to\infty} \int_{-T}^{T} I(q,t)I(q,t+\tau)dt \Big/ \lim_{T\to\infty} \int_{-T}^{T} I(q,t)^2 dt \qquad (26)$$

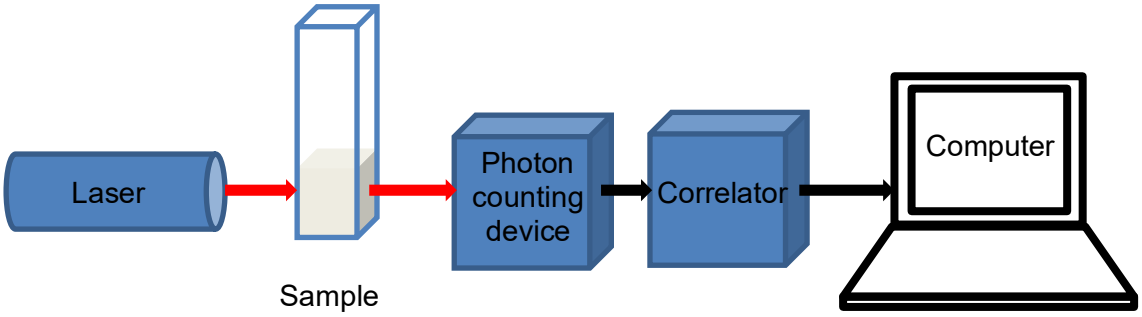

Fig. 6 The main components of a DLS instrument.

The correlation is designed to extract correlation in a fluctuating signal at different times t, $t+\tau$, $t+2\tau$ and so on. At short times the positions of the particles change very little, thus the scattered intensities too, which results in $g^2(\tau=0)=2$. After long time the positions are

uncorrelated to the ones at $\tau = 0$, so that the intensities are random and there is no correlation between them, $g^2(\tau \to \infty) = 1$. On the intermediate time scales the particles diffuse and change positions leading to a loss in the correlation function characterized by the correlation decay time. That explains the curve in **Error! Reference source not found.**c.

The normalized temporal autocorrelation function of the scattered amplitude E_s is:

$$g_1(q,\tau) \equiv \frac{\langle E_s(q,0)E_S^*(q,\tau)\rangle}{\langle |E_s|^2\rangle} \tag{27}$$

where τ is the correlation delay time, q – the magnitude of the scattering vector.

The scattered amplitude E_s can be evaluated as:

$$E_s(q,t) = \sum_{i=1}^{N} b_i(q) e^{i\boldsymbol{q}\boldsymbol{r}_i(t)} \tag{28}$$

where $b_i(q)$ is the field amplitude of the light scattered by particle i at the angle θ and $\boldsymbol{r}_i(t)$ is the position of the center-of-mass of this particle at time t. This represents the dependence of the changes in scattered radiation on the position changes due to Brownian motion.

Since the average intensity of the scattered light is $\langle I\rangle = \langle |E_s|\rangle^2$ (the brackets mean time averaging), the normalized autocorrelation function can be written in this way:

$$g_1(\tau) = \frac{\langle E_s(t+\tau)E_S^*(t)\rangle}{\langle I\rangle} \tag{29}$$

During the DLS measurement the intensity autocorrelation function $g^2(\tau)$ is usually measured:

$$g^2(\tau) = \frac{\langle E_s(t)E_S^*(\tau)E_s(t+\tau)E_S^*(t+\tau)\rangle}{\langle I\rangle^2} \tag{30}$$

For a Gaussian scattered field with zero mean (in most cases) both autocorrelation functions are related by the Siegert relation:

$$g^2(\tau) = 1 + |g_1(\tau)|^2 \tag{31}$$

For a simple diffusion case like e.g. diluted particle in a solvent, $g_1(\tau)$ can be described as single exponentials with relaxation rates Γ:

$$g_1(\tau) = \langle e^{-\Gamma\tau}\rangle \tag{32}$$

The correlation decay rate Γ characterizes how fast the correlation is decreasing and is related to the translational diffusion coefficient D by $\Gamma = \mathrm{q}^2 D$ [84].

For large particles the decay rate is larger than for small particles. Moreover, in the case of polydisperse size distributions the sharper the decay, the more monodisperse system we have [69].

The translational diffusion coefficient can be calculated for a sphere with hydrodynamic radius r_H using the Stokes-Einstein equation:

$$D = \frac{k_B T}{6\pi\eta r_H} \tag{33}$$

where k_B is the Boltzmann's constant, T - temperature and η - viscosity.

DLS allows to detect particles with diameter between 0,001 and 50 microns. Correlation function decay time usually is from several microseconds to seconds and is dependent on the size of the observed particles [86].

The Zetasizer Nano ZS instrument (Malvern Instruments, Malvern, United Kingdom) was used to perform DLS measurements. Autocorrelation functions were analyzed using an algorithm similar to CONTIN, which was installed in the instrument [87]. Experiments were performed in disposable solvent resistant micro cuvettes (ZEN0040) at 20°C with a sample volume of 70 µL. The scattered intensity was measured at 173° using a wavelength of 633 nm (HeNe laser). Detectable particle size range is from 0.3 nm up to 10 µm.

10.3.2. Nuclear magnetic resonance and PFG-NMR

Nuclear magnetic resonance (NMR) is a powerful spectroscopic technique widely used in various scientific fields, including chemistry, physics and biology. NMR provides valuable information about the structure, dynamics and interactions of molecules at the atomic level. In contrast to traditional methods that study self-diffusion by tracking how different isotopes mix within the sample, NMR field gradient techniques have some unique advantages. These techniques allow us to exclude any factors that could interfere with the microdynamic processes [88].

NMR exploits the fundamental property of atomic nuclei, called nuclear spin, which arises from the presence of an odd number of protons and/or neutrons in the nucleus. NMR spectroscopy is based on the interaction between the nuclear spins and an external magnetic field.

In NMR, a sample containing molecules of interest is placed within a strong and uniform magnetic field. This magnetic field aligns the nuclear spins of the sample in two possible orientations, referred to as "spin-up" and "spin-down." The energy difference between these two spin states depends on the local electronic and chemical environment of the nuclei.

To probe the nuclear spin states, a radiofrequency pulse is applied to the sample at a specific frequency corresponding to the energy difference between the spin states called the Larmor frequency. The Larmor frequency depends on the strength of the magnetic field (B) and the gyromagnetic ratio of the nucleus (γ), which is a fundamental property of each specific nucleus:

$\omega_L = \gamma B$. By applying radiofrequency pulses at the Larmor frequency, the nuclear spins can be manipulated and detected. These pulses cause a transition of the spins, resulting in the absorption of energy. When the pulse is stopped, the spins gradually return to their original alignment, releasing the absorbed energy. This energy release is detected as an NMR signal, which is typically represented as a free induction decay (FID), which is a time-domain signal resulting from the detection of the spins returning to equilibrium after the radiofrequency pulse is applied. The FID is then Fourier-transformed to obtain a frequency-domain spectrum known as the NMR spectrum. The NMR spectrum consists of peaks corresponding to different resonances, each representing a distinct nuclear environment in the molecule [89].

The NMR signal is highly sensitive to the local environment and interactions experienced by the atomic nuclei. Various parameters can be derived from the NMR spectrum, including chemical shifts, which provide information about the electronic environment of the nuclei; coupling constants, which reveal the presence of neighboring nuclei; and relaxation times, which describe the rate at which the spins return to equilibrium.

One application of NMR in the study of diffusion processes is the pulsed field gradient NMR (PFG-NMR) technique. This technique is a non-invasive method for analyzing molecular movement without affecting the system being examined at the time scales on the order of microseconds to seconds [90]. By only adjusting the phase and/or orientation of nuclear magnetic moments in the diffusing molecules, a measurable signal can be obtained.

PFG-NMR is a specialized method within the realm of NMR that enables the measurement of molecular diffusion in complex systems. It relies on the application of magnetic field gradients during the NMR experiment, which introduces a spatial dependence to the NMR signal. By varying the strength and duration of the applied gradients, it is possible to selectively encode the diffusion behavior of molecules within the sample.

The underlying principle of PFG-NMR is based on the phenomenon of Brownian motion, where molecules undergo random thermal motion. As molecules diffuse in a solution, they experience different local magnetic field strengths due to the applied gradients. This variation in the magnetic field causes a dephasing of the nuclear spins, which is observed as a loss of coherence in the NMR signal. By analyzing the decay of the NMR signal as a function of the gradient parameters, it is possible to extract quantitative information about the diffusion process, such as the diffusion coefficient and the characteristic length scales associated with the motion.

PFG-NMR has been widely applied in the study of various systems, including liquids, polymers, colloids and biological samples. It provides insights into the dynamics of molecules

in solution, such as the diffusion of small molecules in liquids, the movement of polymer chains in polymer solutions or the transport of particles in colloidal suspensions.

10.3.3. Optical microscopy

A compound light microscope (LM) produces a magnified image of an object, or a specimen, using visible light. The image is projected onto the retina of the observer's eye or other imaging device (like a camera) [91].

The main types of LMs are bright and dark field microscopes, where the first one excludes the scattered beam from the sample and the later includes illumination light (unscattered beam) from the image. In Fig. 13 rays' pathways that form a diffraction pattern in the back focal plane of the objective are shown. The illuminating light is diffracted when it passes the specimen, and the imaging pathway reconstructs the image using the diffracted light. The ray which is not refracted and passes through the sample (gray ray in Fig. 13) is called the zero order and produces the bright background (bright field LM). Other rays interfere constructively and destructively creating a diffraction pattern in the back focal objective's plane. At least two diffracted orders or the zero order and one diffracted order are necessary to resolve details in the primary image plane.

LM can also use transmission or reflection geometries. The difference between them is that for the first one the illumination and imaging parts of LM are on the different sides of the specimen, while for the second one these parts are located on the same side [92].

LM consists of eight planes between the illuminator and the eye. Some of them are fixed (aperture/diffraction planes) and others (object/field planes) can be changed during adjustment the microscope. Usually, a Köhler method of illumination is used that was created by August Köhler in 1893 and provides bright and even image of the specimen and fixed localization of all the planes leading to an improved spatial resolution.

The microscope is called compound because two lenses, the objective and the eyepiece (or ocular), provide the total magnification M of the image:

$$M = M_{objective} * M_{ocular} \tag{34}$$

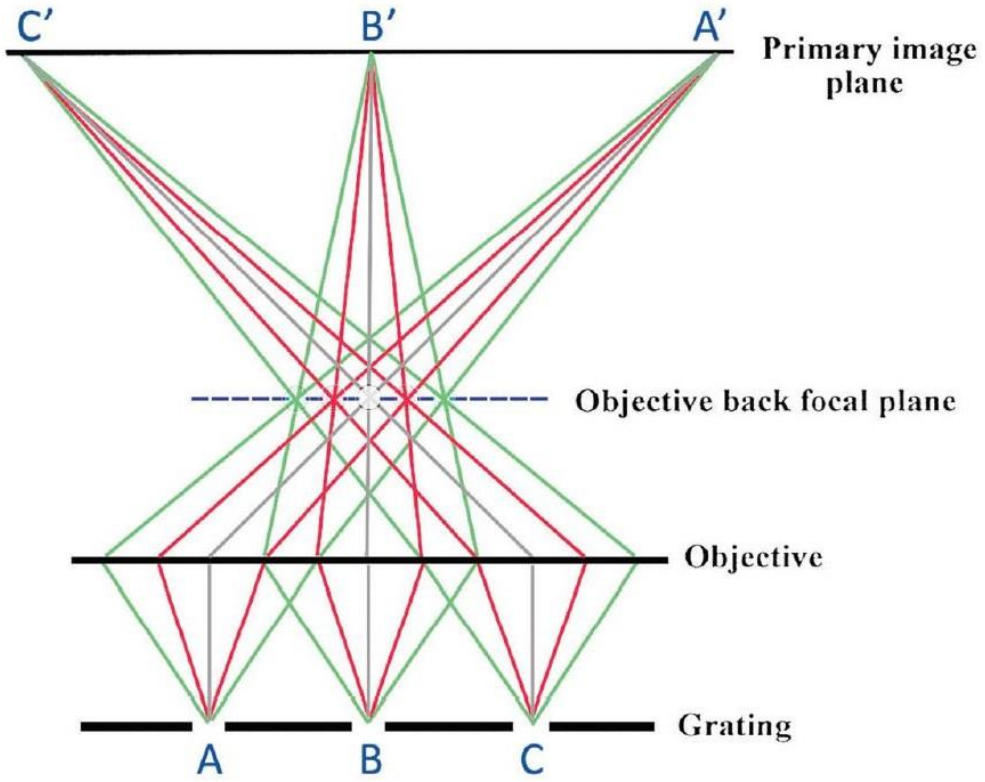

Fig. 13 Image formation in LM. Taken from the work of J. Sanderson [92].

Fig. 14 describes how the image is magnified in the microscope. Firstly, a real intermediate image in the eyepiece is created by the objective. Secondly, the eyepiece and the eye work together to analyze this image and form a real image on retina. Finally, the retina and our brain receive the magnified virtual image that is about 25 cm far from the eye. If one uses a camera to get the image on the screen, the real intermediate image is directly recorded.

Numerical aperture (NA) is the angular aperture of the objective and characterizes its resolution and light-gathering ability. When one uses a high-NA objective with immersion (oil, water) it is possible to have the high-order diffracted rays. The NA is calculated as:

$$NA = n * \sin \alpha \tag{35}$$

where n is the refractive index of the medium through which the objective operates, α is a half of the aperture angle (Fig. 15).

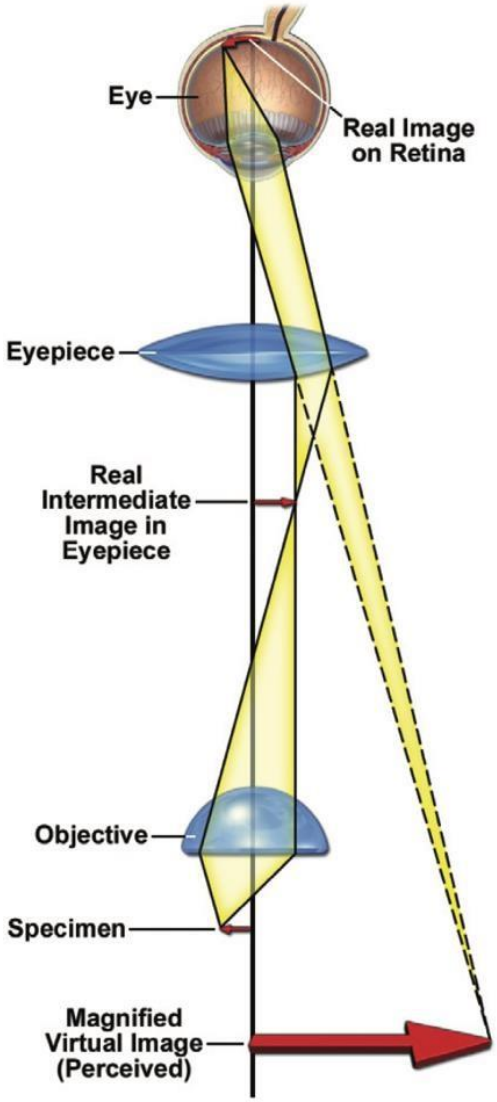

Fig. 14 Magnification of the specimen's image in the microscope. Taken from the work of D. B. Murphy and M. W. Davidson [91].

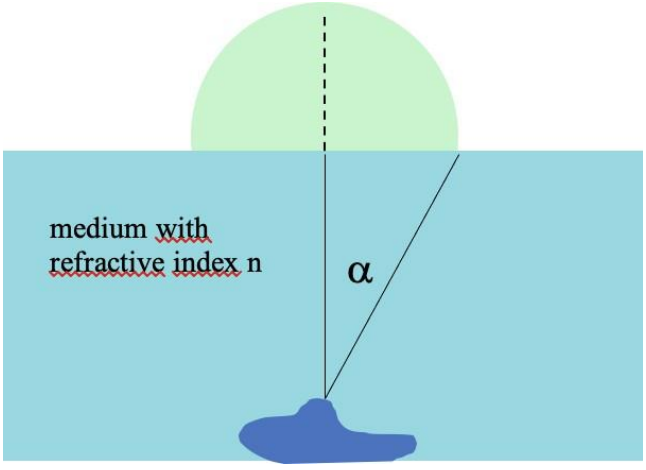

Fig. 15 Light passing through the medium with refractive index n.

The resolution of the microscope can be increased by:

- increasing the aperture half-angle α;
- using smaller illumination wavelengths: it results in smaller diffraction angles from each point of the specimen, which causes a larger number of interference orders that can be collected;
- having the media with larger refractive index n. Immersion oil, water or glycerol between the objective and the specimen are used for this reason;
- increasing the angle of illumination by adjusting the condenser and objective apertures (which can be adjusted setting up Köhler illumination).

The resolution is limited by the diffraction, so called Abbe, limit: the microscope has a limit in the information-gathering power, which is described for coherent illumination as $d = \frac{\lambda}{2\,NA}$, the minimum distance between two points of the sample that can be resolved [92]. The possible size of the objects that can be observed using LM ranges from 0.2 μm to a millimeter.

I used an inverted microscope (Zeiss Axiovert S100). Images were obtained using an AxioCam HRC camera. Glass slides were cleaned before using. Approximately 4μl of sample was dropped onto the glass slide and were covered with a cover slide using tape as a separator.

11. Interchain hydrodynamic interaction and internal friction of polyelectrolytes

11.1. Abstract

Polymers with intrinsic charges in aqueous environments, known as polyelectrolytes (PEs), have distinct characteristics derived from their chain composition and the counterbalancing effects in their surrounding fluid. The dynamics and structural behavior of PEs are influenced by multiple screening length scales, which emerge from electrostatic, steric and fluid-mediated interactions. We employed techniques like DLS, NSE and PFG-NMR spectroscopy to delve into the PE dynamics and SAXS to study its structure, spanning from dilute to semi dilute regimes. Our findings draw a link between macro-level diffusion processes and segmental dynamics of the chain, highlighting a notable distinction between intrachain dynamics and interactions between chains. When considering collective diffusion, we adopted a colloidal perspective that includes both electrostatic and fluid-mediated interactions. The dynamics of the chain aligns with the conventional Zimm model, which describes a neutral chain's movements slowed down by internal friction. One key observation from our research was that fluid-mediated interactions between chains persist even when we expect them to be screened, and the chain's internal friction increases as more ions become condensed onto the chain.

11.2. Introduction

PEs occur in nature in entities such as RNA or IDPs and are widely used in industrial applications [6]. The main determinants of their conformation include polymer structure, solvent compatibility and particularly the intrinsic charge in the enveloping aqueous medium. This leads to a shift between a coiled structure at high salt concentrations and an elongated or rod-like form when charges are not screened (at low salt concentrations). Factors such as hydrogen bonding, dipolar interactions, ion condensation and chain connectivity further influence the collective behavior of polymer chains. These conformations and resulting interchain dynamics, especially at high PE concentrations, affect macroscopic properties like viscosity, turbidity, collective diffusion and surface interactions.

The connection between self and collective diffusion coefficients (D_s and D_c), the radius of gyration (R_g) and viscosity (η) is described within Muthukumar's double screening model [42] or Dobrynin's scaling model [43]. These models take into account electrostatic screening, excluded volume and hydrodynamic interactions (HIs). However, these scaling relations exhibit variations based on salt content and concentration across different regimes (dilute, semi dilute and entangled) are also dependent on certain assumptions such as the screening of HIs between chains [44]. While many experimental data fit these models, discrepancies are also reported [45]–[47]. There is a need to understand the connection between segment level dynamics and chain dynamics, a challenge existed since the beginning of PE research.

Hayter et al. studied polystyrene sulfonate (PSS), a representative PE, and explored the relationship $D(Q) = kT\mu(Q)/S(Q)$ between PE structure factor (SF) $S(Q)$, diffusion coefficient $D(Q)$ and single chain mobility $\mu(Q)$ at low salt conditions [49]. This general equation illustrates the correlation between observed collective diffusion and the interplay of forces at thermal energy kT, calculated as $kT/S(Q)$, between particles or chains. This correlation is related to the "de Gennes narrowing", which highlights the reduced mobility at the highest correlations.

In the context of colloidal spherical particles, Ackerson et al. noted a decrease in mobility with increasing concentrations [54]. Later Beenakker and Mazur introduced the $\delta\gamma$-expansion, elucidating the hydrodynamic function $H(Q)$. This function describes the reduced mobility of hard spheres as concentrations increase, breaking it down into a Q-dependent distinct part, $H_d(Q)$, and a component representing self-diffusion, D_s/D_0 [55], [56]. This gave rise to the established formula

$$D(Q) = D_0 H(Q)/S(Q) \tag{35}$$

with the diffusion coefficient of single particles D_0. This formula is used for spheres but also globular proteins and highly anisotropic proteins, such as antibodies and IDPs [50], [51], [57]–[59], [61]–[64].

On the molecular level the behavior of a neutral chain is described in two distinct ways. When hydrodynamic screening is assumed, the Rouse model is used, but if HIs are taken into account, the Zimm model should be considered [41], [42], [48]. NSE makes it possible to study the PE dynamics at this molecular level, exploring the polymer chain within nanometer and nanosecond scales. While its efficacy in investigating polymer dynamics [52], protein domain motions [28], [50] and IDPs [7], [51] is established, its application in the context of PE dynamics remains limited [49], [53].

In this part we bridge the gap between large-scale properties, especially the collective diffusion, investigated by DLS, self diffusion measured by PFG-NMR, and chain dynamics studied by NSE for a model PE, PSS, in aqueous solution. The chain dynamics is described by the Zimm model with internal friction (ZIF). The transition to collective diffusion is done by using the $\delta\gamma$-expansion, including HI screening radius, R_{HI}. Through this, we aim to show that charged PE dynamics can be fully described assuming a decoupling of local chain dynamics from polymer interchain interactions related to HIs and charges for dilute to semi dilute PE solutions.

11.3. Materials

We used PSS acid (PSSH) with molecular weights MW=39 kg/mol (39k) and MW=17.5 kg/mol (17.5k), purchased from Polymer Source Inc., Canada. These samples had weight ratios of MW/MN equal to 1.03 and 1.09, respectively, with a sulfonation degree exceeding 90%. All samples were dialyzed two times to get rid of impurities and to get desired salt concentration. PSSH 0 mM sample was three times dialyzed with D_2O from 500 mM salt concentration and the final salt concentration was 0,02 mM that was taken as 0 mM. PSSH 100mM was also dialyzed twice from 500 mM sample. Other samples (PSSH 500 mM and 1M) were mixed at the corresponding salt concentration and then dialyzed twice with the same salt concentration solution.

PSSNa samples were titrated using NaOD to attain a pD of 7 in D_2O. Conversely, the PSSH samples were simply dissolved in D_2O, resulting in pD of 2.3 for the 10mg/ml PSSH and 1.8 for the 30mg/ml concentration. All PSS concentrations were below the overlap concentration.

11.4. Results

11.4.1. Collective diffusion

Using DLS, we measured the collective diffusion coefficient, D_c, of PSS [14], [93]. At lower ion concentration c_I values, we noted a splitting of the signal into two: a fast component from collective diffusion and a slow one due to aggregates formation. Further only fast component was investigated. Fig. 16 shows the corresponding D_c for PSS 39k across varying salt concentrations, c_s, from 10mM to 2M. The figure includes the related self-diffusion coefficients, D_s, measured by PFG-NMR. Results for PSS 17.5k are in the Supplementary on

Fig. S1. The D_s values were measured using a 600 MHz Varian spectrometer, which was equipped with a diffusion probe head.

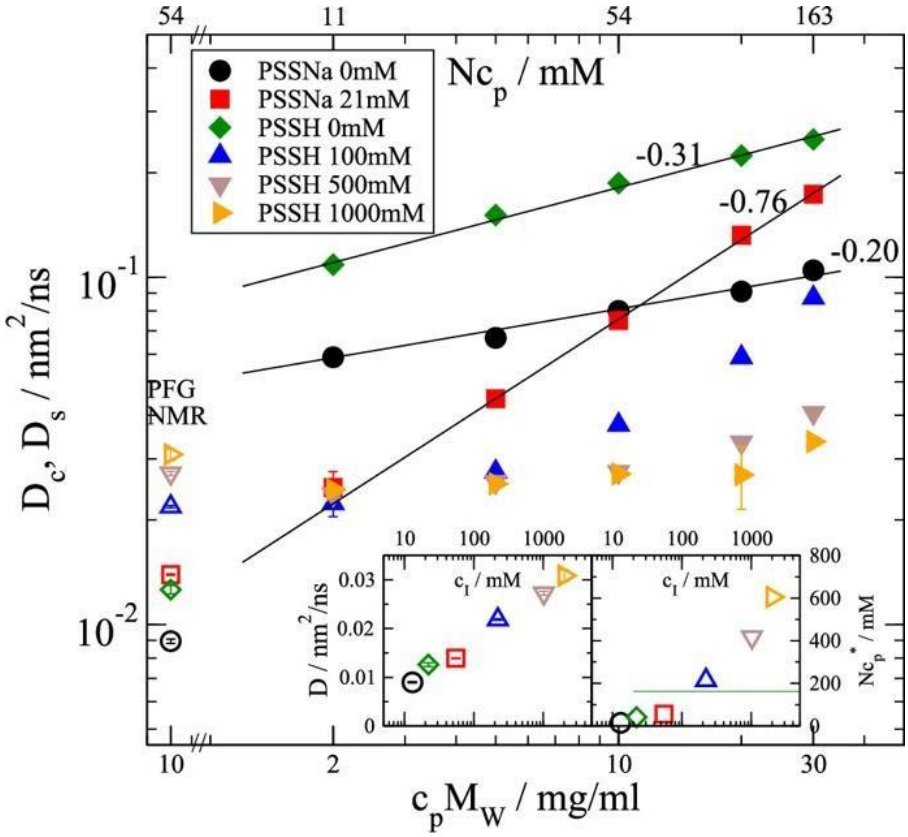

Fig. 16 Collective diffusion coefficient D_c measured by DLS (fast mode, Q = 0.0264 nm^{-1}, solid symbols) and self-diffusion D_s (open symbols, c_p = 10 mg/ml) measured by PFG-NMR for PSS 39k. PSS type (H or Na) and added NaCl concentration c_s as given in the legend. Lines describe power laws with the indicated powers. Left inset: PFG-NMR measured self-diffusion coefficient plotted against the ion concentration $c_I = 2c_s + f^*Nc_p + 2*10^{-pD}$. c_I has contributions from added salt, ions from water dissociation according to the measured pD and counterions. Because of ion condensation on the chain, an effective dissociation of f* ≈ 8% is assumed [94]. Right inset: Monomer overlap concentration Nc_p^* was calculated from D_s (see Supplementary). The line indicates the largest polymer concentration used for NSE.

For high c_s values of 500 mM and 1000 mM, when extrapolating D_c to more diluted conditions, we find an alignment with D_s. However, at reduced c_s levels, the observed scaling relations aren't applicable for such extrapolations. Specifically, at these lower c_s values, D_c has values that are almost ten times greater than D_s. For the intermediate c_s of 100 mM and at higher PE concentration c_p values the slope equals the scaling found for the 21 mM presenting a crossover to the respective power law regime. D_s increases with an increasing ion concentration $\sim c_I^{0.2}$ (left inset of Fig. 16).

Having constant number of segments N, segment length l and the solvent's viscosity η_s, the Zimm model (with $D_Z = (0.196kT)/(\eta_s R_e)$) infers that the end-to-end distance $R_e = lN^{\nu}$ is reduced as ν decreases for higher c_I. The interchain electrostatic repulsion results in an

extended R_e for low c_I. The graph on the right side of Fig. 16 displays monomer overlap concentrations, denoted as Nc_p^*, derived from D_s values. For c_I less than 100 mM at least the larger c_p are above c_p^* and lean towards semi dilute, while their counterparts are more diluted. Similar D_s was observed for PSS 17.5k, but all concentrations remained in the dilute region where $c_p<c_p^*$, as further detailed in the Supplementary.

11.4.2. Structure of PSS

Fig. 17 shows the SAXS results for PSS 39k (17.5k results and fit parameters are in Supplementary, Fig. S2). The scattered intensity $I(Q)$ is calculated as $I(Q) = c_p F(Q, c_p) S(Q, c_p) + d(Q)$, integrating both the FF $F(Q, c_p)$ and the SF $S(Q, c_p)$. Given that the dissociated ions from PE are involved in charge screening, the FF is dependent on c_p. A self-consistent simultaneous fitting approach is employed to derive both $F(Q, c_p)$ and S $S(Q, c_p)$. The chain's FF is a Gaussian chain model, incorporating an excluded volume parameter ν, which describes the chain's extension. This is further complemented by the presence of a disc- like profile as we observed a wormlike structure (additional details in Supplementary). In the mid-Q range, the data aligns with a Q^{-2} power law typically associated with Gaussian chains. This is followed by a clear decay that can be explained by a disc-like cross-sectional representation. The increase at higher Q values is attributed to diffused scattering $d(Q)$, indicating deviations from an ideal wormlike configuration. The respective disc diameter of ≈0.8 nm matches the extent of PSS side chains.

Fig. 18 presents the SAXS results for PSS 39k in varying salt environments: NaCl, CsCl and RbCl (other PSS concentrations are in Fig. S4, 17.5k results – in Fig. S5). The scattered intensity $I(Q)$ remains consistent in its representation as $I(Q) = c_p F(Q, c_p) S(Q, c_p) + d(Q)$, incorporating both FF and SF components. A distinctive feature across the different salt conditions is the pronounced variation in the forward scattering, which underscores the contrast changes induced by different salt ions. This variation, however, does not carry forward into the high Q region, indicating that the structure or form factor remains consistent regardless of the salt type.

As the dissociated ions from the PE are responsible for charge screening, the FF's dependency on c_p remains consistent. The mid-Q region, consistently with previous observations, aligns with a Q^{-2} power law. This signifies Gaussian chains, transitioning into a distinct decay pattern representing a disc-like profile, as previously inferred with wormlike structures.

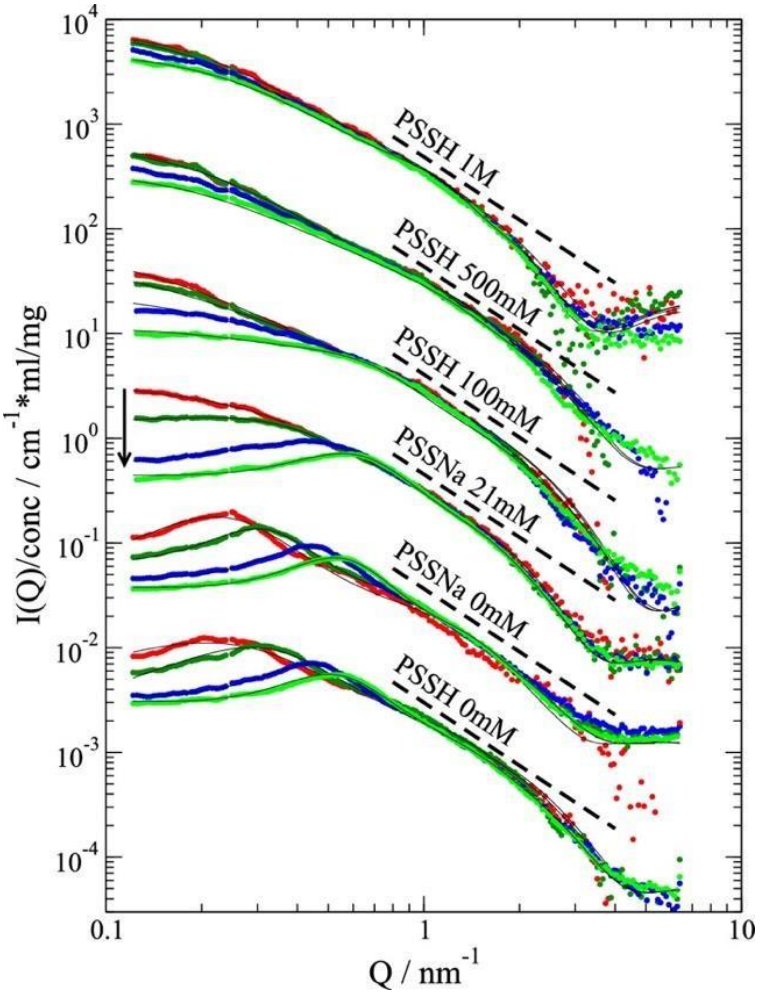

Fig. 17 SAXS data for PSS 39k after background correction and scaled by concentration (c_s shifted consecutively by 10 for visibility). A stronger SF results mainly in the decreased intensity at low Q for increased c_p. Concentrations were 5, 10, 20, 30 mg/ml except for 21mM with 8.3, 16.6, 33.2 and 50 mg/ml (colors red to green, along arrow). Black lines correspond to fits as described. For the two highest NaCl concentrations the repulsive part in 2Y SF was fixed to a negligible contribution. Broken lines indicate the extension of a Q^{-2} power law to high Q to demonstrate the deviation from a Gaussian chain. Measured at inhouse instrument SAXSpace (Anton-Paar).

Interestingly, while the forward scattering contrasts vary with different salts, the high Q regions across these salts demonstrate remarkable similarity. This suggests that while the charge screening and related contrasts can differ based on the salt environment, the fundamental structural characteristics of the PSS chain remain unchanged.

In comparison to NaCl, the SAXS outcomes for both CsCl and RbCl also hint towards the possible influence of ion condensation on the PE chain with some differences. As these ions modulate the chain's environment, they impact the effective charge and dissociation behaviors of the PE chain, potentially altering its dynamics and interactions. These differences in SAXS

patterns due to different salts make a compelling case for further studies into their individual and collective impacts on PSS chain dynamics and structures.

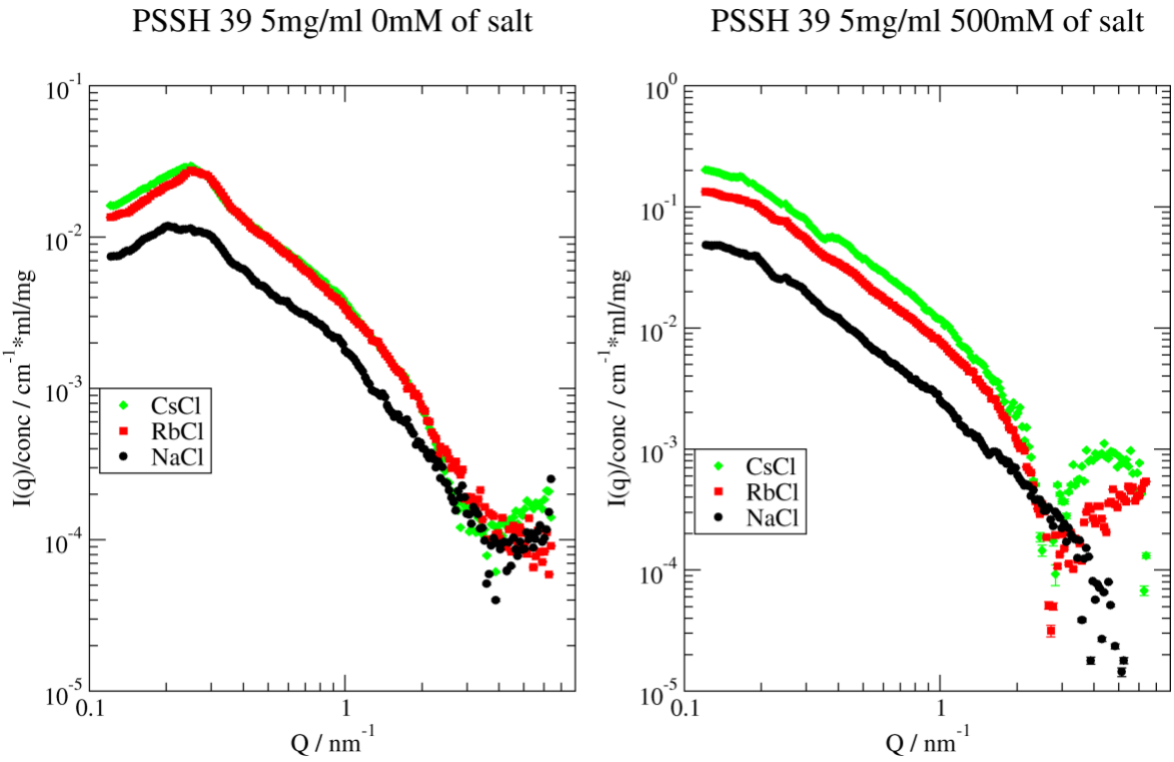

Fig. 18 SAXS data for PSS 39k in NaCl, RbCl and CsCl salts after background correction and scaled by concentration. A stronger SF results mainly in the decreased intensity at low Q depending on the salt used. PSS concentration is 5 mg/ml (other concentration are in Fig. S5). Measured at inhouse instrument SAXSpace (Anton-Paar).

When compared to SANS results, we observe a flatter power law curve (Fig. 19). This divergence between SAXS and SANS interpretations can be due to the Na^+ ion condensation on the chain. The bonded Na^+ significantly modulates the neutron contrast, which is predominantly influenced by hydrogen elements. Such ion condensation has implications for the PE chain's effective charge, leading to an effective dissociation rate around 8% [94].

In our observations, $S(Q)$ aligns with a 2Y SF [36]. This captures screened electrostatic repulsion within a few nanometers and an additional short-range attraction at less than 0.3 nm (Fig. 17 and Fig. S2 in Supplementary). We interpret this attraction as a consequence of the chain's hydrophobic backbone, the influence of Na^+ ions that condense on the chain or the effects of excluded volume screening [42]. As the ion concentration increases, leading to enhanced electrostatic screening, we notice a weaker SF effect. Notably, the 2Y SF was the only model that accurately reproduces the experimental PE concentration, even at high ion concentrations.

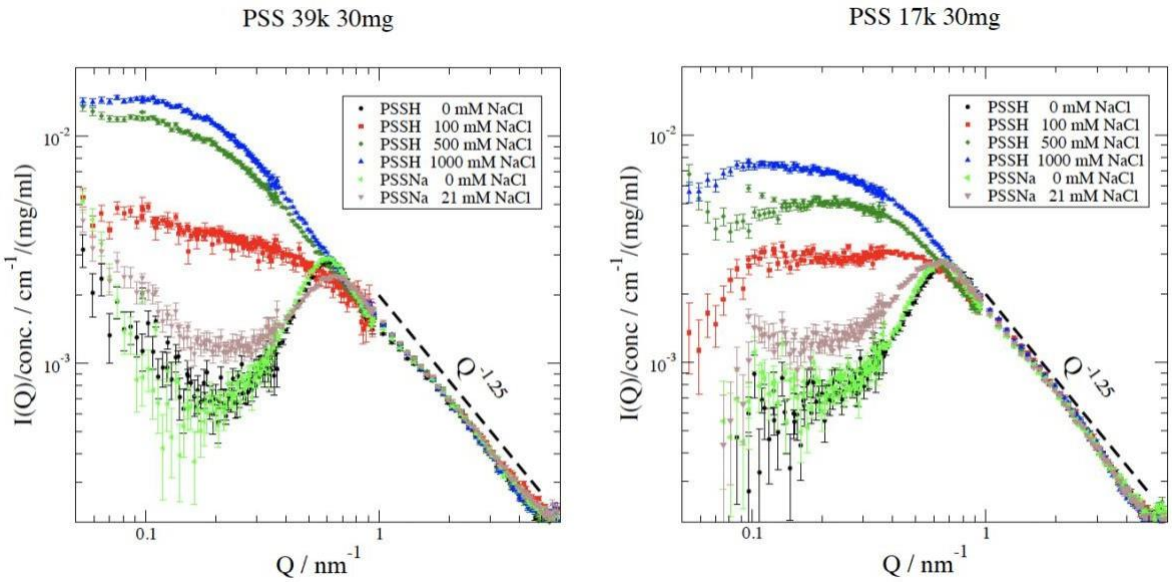

Fig. 19 SANS data at T=20ºC for PSS 39k (left) and 17.5k (right) after background correction and desmearing measured at KWS2, MLZ, Garching [79]. For 17.5k a small increase in slope at larger Q is visible that might also be an indication of the disclike formfactor observed in SAXS. For 39k at low Q we observe for low salt concentrations an upturn caused by the presence of aggregates also visible in DLS as the slow mode.
Extrapolating this contribution to the NSE Q range shows that the slow mode is negligible in the NSE signal. For 17.5k the contribution is even smaller. The data are corrected for instrumental resolution using the Lake algorithm that instrumental resolution does not affect the shown data or the observed power law.

11.4.3. Dynamics of PSS

Fig. 20 shows the dynamic SF of a PE chain over time, as measured by NSE [95]. We observed it in a time frame from 0.1 ns up to 100 ns. We also display a set of synthetic data that aligns with the DLS-measured D_c. For clarity and to better understand upcoming models, we define an effective diffusion coefficient, D_{eff}, by fitting data with $\sim\exp(-Q^2 D_{eff} t)$. The results for the PSS 39k sample are in Fig. 21, and for PSS 17.5k in the Supplementary Fig. S9. At smaller Q values, the transition from collective diffusion to individual chain dynamics becomes clear. Short time relaxations, especially between 1-10 ns (which relates to higher Q values), give us a closer look at the relaxation of small chain segments.

In our efforts to understand the shift from the collective dynamics observed at low Q values to the more local dynamics at high Q, we employ a particular model. This model blends the $H(Q)/S(Q)$ adjustment, which is a result of interactions between chains, with a classical polymer model complemented with internal friction. We assume that the movements within a chain operate separately from the interactions between chains.

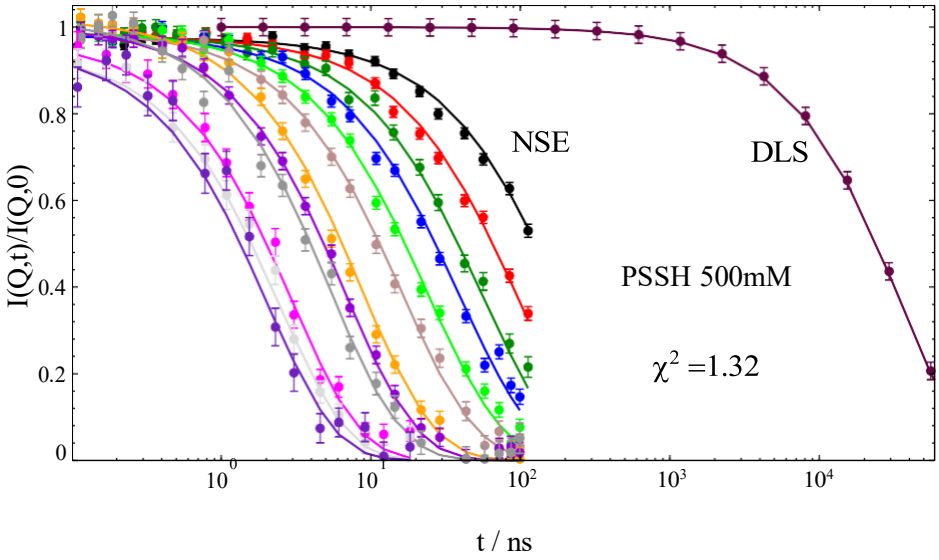

Fig. 20 NSE measured intermediate scattering function I(Q,t)/I(Q,0) up to 100 ns for PSS 39k 500 mM at 30 mg/mL measured at IN15, ILL, Grenoble [95]. Q values are shown in Fig. 21. We add a synthetic Q = 0.0264 nm^{-1} data set that represents the measured D_c from DLS at the same concentration (relaxation time of ≈36 µs). Solid lines represent the combined fit using the H(Q)/S(Q) corrected ZIF model with, in general, small χ^2. Other ion concentrations and data for PSS 17.5k are shown in Supplementary.

The Zimm model, typically used for neutral polymers, is a bead-spring model with N beads connected by segments, each of length l. These beads experience friction with the surrounding solvent, having viscosity η_s, and HIs between the beads [41]. The intermediate scattering function (ISF) for a single chain can be represented as

$$I(q,t) == \frac{\exp\left(-Q^2 \mathrm{D}\tau\right)}{N} \sum_{n,m}^{N} \exp\left(\frac{-q^2 B_{n,m}(t)}{6}\right) \tag{36}$$

$$B_{n,m}(t) = |n-m|^{2\nu} l^2 + \frac{4R_e^2}{\pi^2} \sum_{p=0..\mathrm{N}-1} \frac{A_p}{p^{2\nu+1}} \cos\left(\frac{\pi p n}{N}\right) \cos\left(\frac{\pi p m}{N}\right) \left(1 - e^{-t/\tau_p}\right) \tag{37}$$

with center of mass diffusion for a single chain $D = D_z = 0.196 k_b T/(\eta_s R_e)$, wavevector Q and end-to-end distance $R_e = lN^{\nu}$. The parameter ν describes the interactions between the polymer and the solvent. For θ- and good solvents, it is between 0.5 and 0.6. However, in the case of charged chains, one can expect an elongated chain structure, pushing the ν value even beyond 0.8 [6], [44]. The Zimm time is a crucial measure that is influenced by the chain's expansion. By also taking into account friction experienced between adjacent beads, we further refine the model, leading to the ZIF model, which brings in the concept of mode relaxation times.

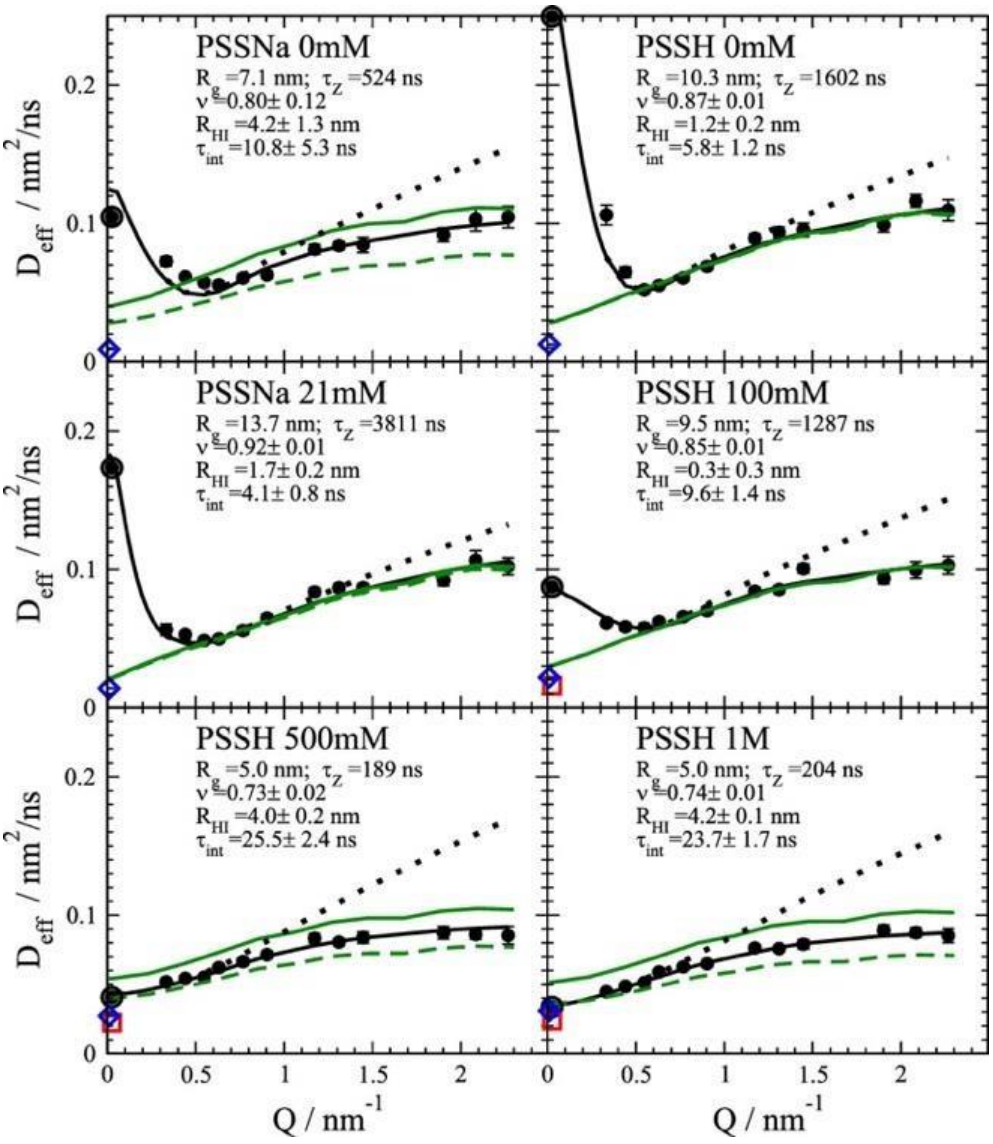

Fig. 21 Effective diffusion coefficients D_{eff} for PSS 39k c_p = 30 mg/ml with respective parameters from the full fit model: experimental (points); ZIF with full $H(Q)/S(Q)$ correction (black line); ZIF only with self-part correction D_s/D_0 (green dashed); same but $\tau_{int} = 0$ (Zimm) (dotted); ZIF without correction (green line); DLS extrapolated concentration 0 mg/mL (red square), 30 mg/mL (circle); PFG-NMR self-diffusion (blue diamond). It should be noted that the self-part corrected ZIF (green dashed line) fits well to D_s. The self-part D_s/D_0 correction is noticeable as a difference between solid and dashed green lines.

The Zimm time (p=1) is $\tau_Z = \eta R_e^3/(\sqrt{3\pi}k_bT)$ and depends on the chain expansion through R_e. By also taking into account friction between neighboring beads (ξ_{int}) we further refine the model, leading to the ZIF model [68]. Mode relaxation times $\tau_p = \frac{\tau_Z}{p^{3\nu}} + \tau_{int}$ are additive slowed down by the internal friction time τ_{int} that stronger affects higher order modes observed at larger Q. This approach has been effectively applied in studies of individual nanoparticles

and IDPs [51], [96]. However, at concentrations below the overlap concentration, the dynamics within a chain could be influenced by interactions between chains [97].

To bridge the gap between D_c and the data we've obtained at intermediate Q with NSE, we've adapted the ZIF model with interactions between chains, leading us to the correction for spherical colloidal particles as $D(Q) = D_Z H(Q)/S(Q)$. Both $S(Q)$ and $H(Q)$ here depict a sort of average of configurations. This also suggests a separation between center of mass diffusion and intrachain dynamics.

The hydrodynamic function $H(Q) = H_d(Q) + D_s/D_0$ for spherical particles of a specified radius can be efficiently calculated using the δγ-expansion technique proposed by Beenakker and Mazur [55], [56] with the distinct contribution

$$H_d(Q) = \frac{3}{2\pi}\int_0^\infty d(ak)\,\frac{\sin^2(ak)}{(ak)^2[1+\Phi S_\gamma(ak)]} \times \int_{-1}^{1} dx(1-x^2)S(|\boldsymbol{Q}-\boldsymbol{k}|-1) \tag{38}$$

and the self-part describing the change in self-diffusion

$$\frac{D_s(\Phi)}{D_0} = \frac{2}{\pi}\int_0^\infty dt\; sinc^2(t)\big[1+\Phi S_\gamma(t)\big]^{-1} \tag{39}$$

where x is the angle between the wave vectors $\boldsymbol{Q}$ and $\boldsymbol{k}$ and function $S_\gamma(t)$ is given by Genz and Klein [70].

Particle correlation and the associated interactions enter the distinct part of H_d through the SF $S(Q)$. The HI is described as the mobility of a sphere, characterized by its geometrical radius a. The corresponding HI volume fraction is $\Phi = \mathrm{n}4\pi a^3/3$, n is the number density. For stronger interactions, like those experienced by charged spheres, there's a clear distinction between the radius a and the interaction's length scale.

The screened HI was set to an equivalent HI screening radius $R_{HI} = a$. This is analogous to attributing a hydrodynamic radius R_h to polymers or non-spherical objects that with an equivalent sphere diffusion coefficient. When HI screening is strong, R_{HI} tends towards smaller values. For ideal Gaussian chains, $R_h \approx 0.66R_g$, which describes the single chain friction with the solvent [41]. This differs from R_{HI}, which looks at the effective HI between chains, but R_h can be a potential upper boundary.

For a comprehensive analysis of the complete NSE spectra, we use $S(Q)$ derived from our SAXS measurements and calculate $H(Q)$. The ZIF model's parameters are fixed by the polymer's dimensions (with l=0.24 nm [98]; for 39k N=212 and for 17.5k N=95, p<25). Our fit incorporates several free parameters: ν, which determines D_Z; R_{HI}, which measures the extent of HI screening; and τ_{int}, highlighting the slowing down at larger Q due to internal friction. All functions are accessible within the free software tool, Jscatter [37].

We observe very good alignments between our NSE spectra fits and the data shown in Fig. 20 and Fig. S7 and Fig. S8 in Supplementary. In Fig. 21, we compare D_{eff} from our observed data, fit models and computations across various salt concentrations c_s. For low salt concentrations at Q < 0.5 nm^{-1}, there's a pronounced collective effect of the $H(Q)/S(Q)$ correction, which is visible as an upturn. This leads to a much larger value of D_c relative to D_s. As the salt concentration increases, this difference starts to vanish as $S(Q)$ becomes weaker.

When Q values exceed 0.5 nm^{-1}, $H(Q)/S(Q)$ appears to be constant, at which point we begin identifying self-diffusion characteristics. In the range up to Q ~1 nm^{-1}, there's a distinct Zimm-like trend where D~Q. The trend's gradient is in close alignment with the Zimm model's (dotted line) relaxation rate $\Gamma_{eff} = Q^2 D_{eff} \sim Q^3 k_B T/\eta_s$ [41]. The linear increase in D_{eff} reflects D_Z along with additional low mode components, which are less affected by internal friction. However, for even larger Q values, deviations from the classic Zimm dynamics slow down more local modes due to internal friction.

Across all ion concentrations, it's clear that τ_{int} considerably reduces D_{eff} in contrast to the pure Zimm model. Interestingly, as ion concentration is growing, τ_{int} also tends to increase, but it remains significantly smaller than the Zimm time τ_Z. This trend results in narrowing Zimm like region as τ_{int} increases with ion concentration.

Fig. 20 shows the sensitivity of NSE data to fluctuations at a nanosecond level for larger Q values. Analyzing ν reveals a decline as ion concentration rises, dropping from values above 0.8. This suggests notable conformational shifts driven by stronger screening effects.

The results for PSSNa at 0 mM NaCl concentration for both 39k and 17.5k show a smaller difference between D_c and D_s when compared to either PSSH at 0 mM or PSSNa at 21 mM. DLS data prove this observation by showing a reduced power law alongside smaller values of D_c. This is not influenced by concentration variances or crossing the c_p^* threshold.

For the 100 mM NaCl concentration both 39k and 17.5k (see Fig. S9), R_{HI} demonstrates very small values (<0.3 nm), especially when set against the considerably larger values observed at both low and high salt concentrations. R_{HI} at 0 mM NaCl aligns closely with values for >100

mM NaCl. A pronounced HI effect is evident, particularly when analyzing the correction from the self-part D_s/D_0, which is visible as difference between the solid and dashed green lines. Further, the ratio R_{HI}/R_g is close to R_h/R_g value of 0.66 expected for Gaussian polymer chain. This could be a limiting case for strong HI, especially in comparison to the weaker HI at intermediate ion concentrations.

A weaker charge of PSSNa at 0 mM NaCl, when compared to 21 mM, explains the reduced difference between D_c and D_s at 0 mM. We are seeing the larger adsorption at the lowest ion concentration, a trend further visible at the DLS data, as seen in Fig. 16, which outlines an alternate power law. However, this isn't reflected in D_s. The differences can be attributed to a larger counterion adsorption of Na^+ ions on PSS, noticeable at both the low and high ion concentrations. This adsorption intensifies the coupling between neighboring segments, increasing both the internal friction and τ_Z at 0 mM and high ion concentrations.

When exploring the effects of temperature, we conducted additional measurements on PSSH at 0 mM, PSSNa at 0 mM and PSSH at 500 mM NaCl concentration, at temperatures of 40 and 60°C. The viscosity-adjusted D_{eff} results from these measurements are illustrated in Fig. 22.

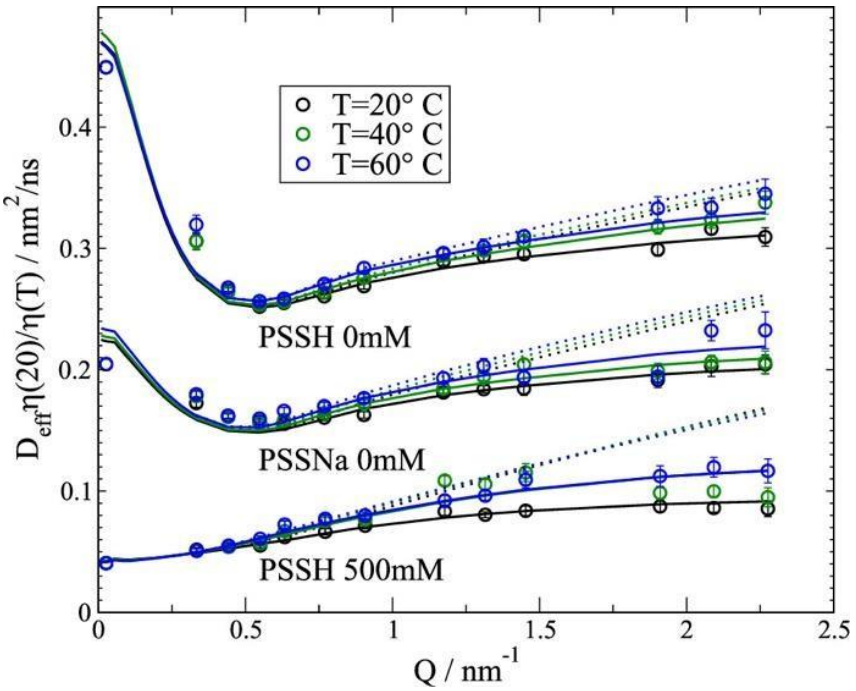

Fig. 22 Viscosity scaled D_{eff} for PSS 39k at different temperatures (color coded as indicated: experimental (points); ZIF with $H(Q)/S(Q)$ correction (solid line); same but $\tau_{int} = 0$ (Zimm) (dotted line)). All values are scaled by solvent viscosity to 20°C. Full NSE spectra with fits and an Arrhenius plot of τ_{int} are shown in Supplementary in Fig. S10 and Fig. S11.

At low Q values, there is an alignment with the viscosity of the solvent. A decrease of τ_{int} is observed with increasing temperature (details in Supplementary in Fig. S11). Both D_Z and τ_Z

are related to the solvent's viscosity. Conversely, τ_{int} is associated with aspects such as bond rotation, steric hindrance, charge repulsion and the binding of Na^+ ions between segments. The activation energy of τ_{int} is close to the water activation energy; therefore, accounting for viscosity scaling also compensates for changes in τ_{int} (further details in Fig. S11).

11.5. Conclusion

In summary, we studied the dynamics of a classical PE, PSS, extending observations on macroscopic length scales to segmental chain dynamics. Different from previous hypotheses, the hydrodynamic interactions between chains are not fully screened and are essential to understand the connection between collective diffusion, self-diffusion and chain dynamics. We observe that the dynamics of a charged PE on a segmental level follows a neutral chain Zimm model with internal friction (ZIF). The PE charges result in an increased R_e. For intermediate Q, the chain dynamics follows the Zimm prediction, while at larger Q the internal friction between neighboring monomers significantly slows segment motion. The source of internal friction seems to be related to counterion condensation.

12. Formation of ordered phases in dense poly amino acid coacervate droplets

12.1. Abstract

In this part we studied phase separation and coacervate formation of polyelectrolyte complexes (PECs) resulting from mixing two oppositely charged poly amino acids (PAAs). The focus was on investigating the influence of external variables, such as pH, salt concentration, temperature, and different approaches in sample preparation on the state and structure of our complexes. Salt plays a crucial role in the PECs formation resulting in getting solid precipitates at low and high NaCl concentrations with defined structure, while at the medium salt concentrations a coacervate phase is observed with no specific internal structure, more like a liquid like phase.

12.2. Introduction

PECs have received increasing attention in recent years as a promising class of functional materials with potential applications in various fields such as biomedical engineering [8], drug delivery [9] and water treatment [18].

The formation of PECs after mixing two oppositely charged PEs results in a phase separation that can be influenced by variety of conditions in the solution, such as salt and PE concentrations, pH, temperature or molecular weights (MWs). Depending on that their state diverse from solid precipitate to liquid dense phase, which is known as a coacervate phase and is seen as droplets in the microscope [21].

Despite the growing interest in PECs, there is still much to be learned about their formation, stability and properties. Many studies have investigated the mechanism of PECs formation and the influence of various factors on their properties. However, there are still many questions that remain unanswered, and further research is needed to fully understand the behavior of these complex systems.

Our system of investigation consists of two oppositely charged PAAs. As negatively charged PAA poly(L-aspartic acid) (PASP) or poly(L-glutamic acid) (PGA) were used, that were mixed with positively charged poly(L-arginine hydrochloride) (PLA). It was already observed that salt strongly influences the state of PECs (for mixtures of poly(acrylic acid) and poly(allylamine hydrochloride) [22]). At zero salt concentration precipitate for these PECs was

observed. With adding salt coacervates were formed and with enough salt a gel-like state can be reached. Even higher salt concentration caused the dissolution of gels or aggregates in the system. Centrifugation is important to collect the micron sized droplets from the phase separation as macroscopic phase and resulted in forming white precipitate at low salt concentration and a highly viscous liquid coacervate phase at medium salt concentrations. The other observation was that 1:1 anion:cation molar ratio results in the strongest PECs formation which was tested in our work as well [22] [23].
In this part, we studied the dependence of PECs structure on temperature, salt and PAAs concentrations and other external conditions that affected our samples.

12.3. Materials and preparation

PASP (MW=11500 Da), PGA (MW=13000 Da) and PLA (MW=19000 Da) were obtained from Alamanda Polymers (Huntsville, Alabama, United States). Sodium chloride (NaCl≥99,5%, MW=58,44 g/mol) was obtained from SigmaAldrich (St. Louis, Missouri, United States). The chemicals were used without additional purification.
Stock solutions of each PAA (6 mM concentration) were prepared in deionized Milli-Q water and were titrated to pH 7 using 0.1 M NaOH or 0.1 M HCl solutions. Impurities were removed by 0.1 μm pore Anotop 10 size exclusion filter.
PECs were prepared in three steps: At first, the NaCl was diluted in water at the concentration to achieve the desired concentration after adding PAAs. Then PASP or PGA from the filtered stock solution was added and the solution was vigorously vortexed for 15 seconds. Finally, PLA was added and the sample was also well mixed. Complexation occurred immediately after adding polycation at the last step. After preparation the samples were stored at 6°C.

12.3.1. Centrifugation

Centrifugation was used to collect the droplets from phase separation into a macroscopic phase that can be examined by scattering methods. After centrifugation (at 5236 g for 10 minutes at 21°C) we either observed the white precipitate on the bottom of the vial or a clear solution. At low and high salt concentrations for both PASP+PLA and PGA+PLA mixtures white precipitate was still observed while at the intermediate NaCl concentrations solutions the precipitates were totally transparent after centrifugation. We could clearly see a border between precipitate and supernatant.

The same properties were discovered at other PAAs contents that only changed the amount of the precipitate.

12.4. Results

12.4.1. Physical properties of PECs

Optical microscopy

The phase separation of complexes of PASP+PLA was studied using optical microscopy (Zeiss Axiovert S100). After adding PLA at the last step of PECs preparation the samples were put between glass slides. Exemplary images of the samples after preparation are shown in Fig. 23. Fig. S12 in Supplementary presents the same samples during the first 24 hours after mixing (0,7 mM total PAAs concentration (the same features were investigated at 0,05 mM)).

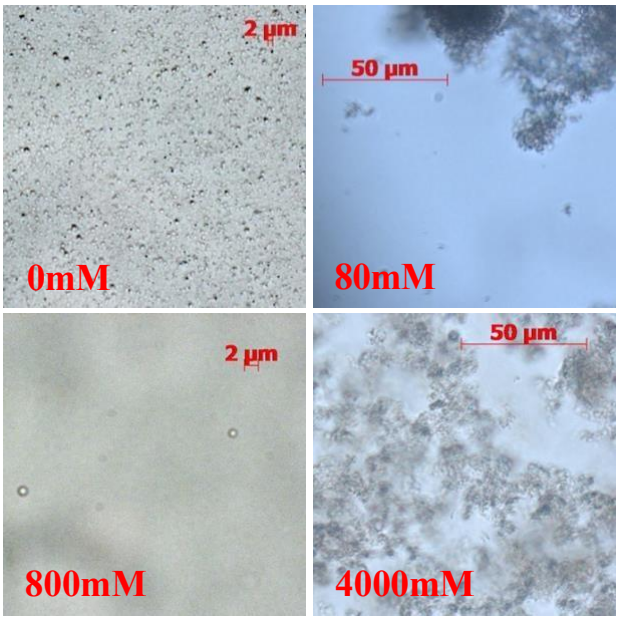

Fig. 23 Images from the optical microscope made for the mixtures of PASP and PLA at different NaCl concentrations directly after preparation at 0,7 mM (10,7 mg/ml) total PE concentration.

At low (0, 80, 160 and 400 mM) and high (2400 and 4000 mM) NaCl concentrations white sticky aggregates were formed but the samples looked different at the microscope. Salt-free mixtures show only small, 0.5-1 μm sized asymmetric nuggets that were stable for 24 hours. Other low salt concentration samples looked locally similar but having large aggregates (>0.1 mm) and disappearing of small nuggets (~μm) with time. Aggregates (<50 μm) at 4000 mM NaCl stayed with time but at 2400 mM they were dissolving, and spherical droplets were formed after 3-5 hours after samples preparation.

Intermediate salt concentrations resulted in forming of spherical droplets 2-5 μm in diameter and in decreasing of their amount with time. After one day they were not more observed, instead not spherical aggregates of the same size were observed.

12.4.2. Chemical composition of precipitate

To get information about the composition of the precipitate, NMR experiments were performed to examine the content of the liquid phase of the supernatant (see Fig. 24). Separate PAAs and supernatants after their mixing and centrifugation were measured. Measuring pure PAAs at the same concentrations as in mixed samples allowed for a more reliable and standardized comparison between the mixed and pure states of the compounds.

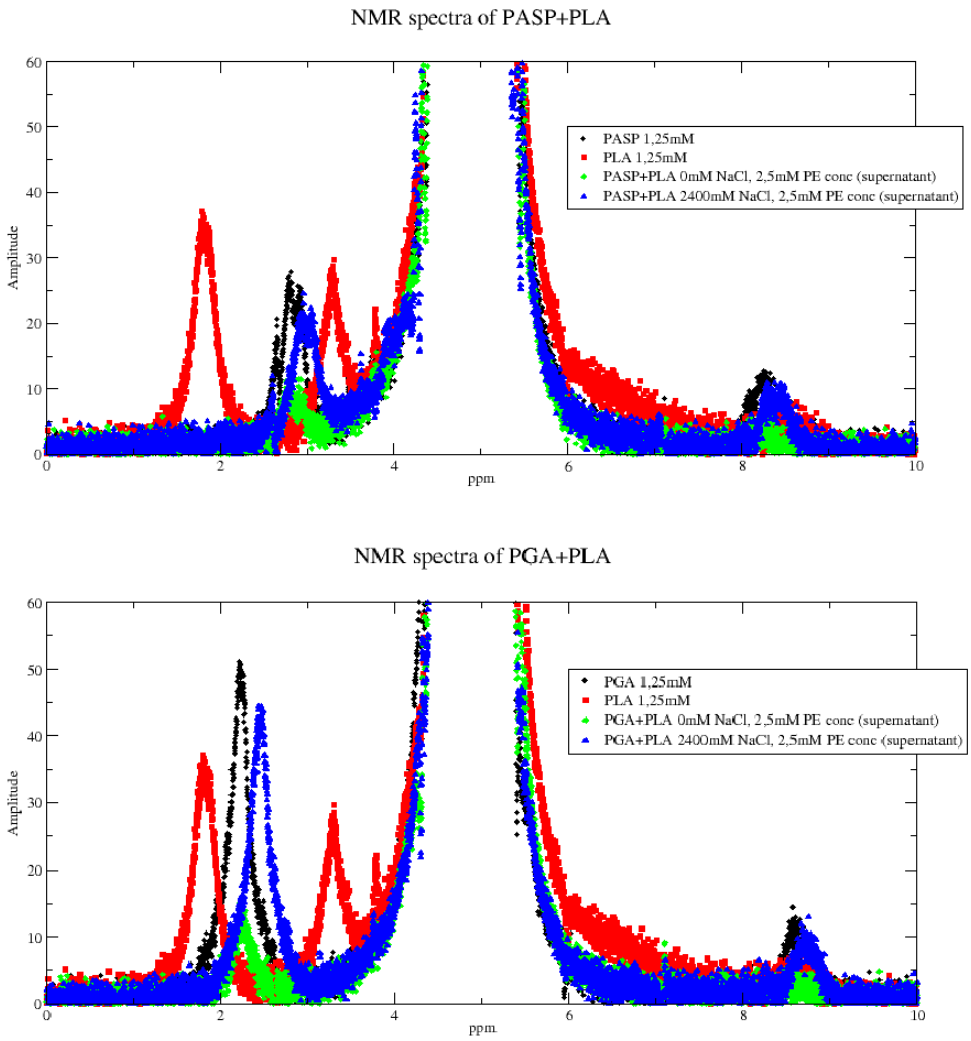

Fig. 24 NMR spectra of separate PAAs and PECs at 0 and 2400mM NaCl.

For both the PASP+PLA and PGA+PLA samples at 0 mM NaCl concentration a part of the negatively charged PAA (30% PASP and 25% PGA. Peak positions: PASP – 2.8 ppm, PGA – 2.3 ppm. Peak amplitude: PASP – 8, PLA – 12) was identified to remain in the supernatant (Fig. 24). This presence indicates that the precipitate formation was mainly attributed to PLA. The driving force of this behavior can be charge neutralization. In this low salt environment, the necessity for PASP to counterbalance the charge of PLA is more pronounced, suggesting differential dissociation behaviors between PASP and PLA. It seems that only 70% of PASP is required to effectively neutralize PLA's charge, with the remaining charge part possibly being compensated by Cl^- ions from the titration process.

At 2400 mM salt concentration, the majority (~85%. Peak amplitudes: PASP – 20, PGA – 42) of PASP/PGA was located in the supernatant. This can be interpreted as a precipitation of the compound of PLA with chloride ions from the NaCl salt, hinting to a possibility of PLA to form hexagonal structures in wet powders, as observed in previous studies [99]. The presence of salt ions appears to favor the interaction between PLA and Cl^- ions, leading to a different structural formation compared to the low salt concentration scenario. This further supports that the ionic environment plays a crucial role in determining the structure and composition of the precipitated complexes.

12.4.3. Structure of PECs

To study the internal structure of our PECs, SAXS experiments on the in-house SAXS instrument GANESHA were done. Samples were put into 2 mm capillaries, centrifuged and SAXS was measured at the bottom of the capillary where precipitate was located.

In the Fig. 25 SAXS curves for PASP+PLA (100 AAs per chain, 1:1 ratio, 2mM total PAAs concentration) PECs are shown. We observed low and high Q peaks at low and high NaCl concentrations when white precipitate after centrifugation was observed. At the intermediate salt concentrations in the transparent phase no prominent structure was detected at SAXS. The positions of the peaks at high Q values indicate a 2D hexagonal structure, while the peaks at lower Qs indicate a second length scale in PEC structure. Hexagonal peak positions indicate a 2 nm lattice constant between the nodes in hexagonal packing at low NaCl concentrations while the second length scale corresponds to a planar stacking with ~15.5 nm lattice constant. At high salt concentrations the hexagonal lattice constant shifts to 1.54 nm and the planar ordering stays around 15.5 nm.

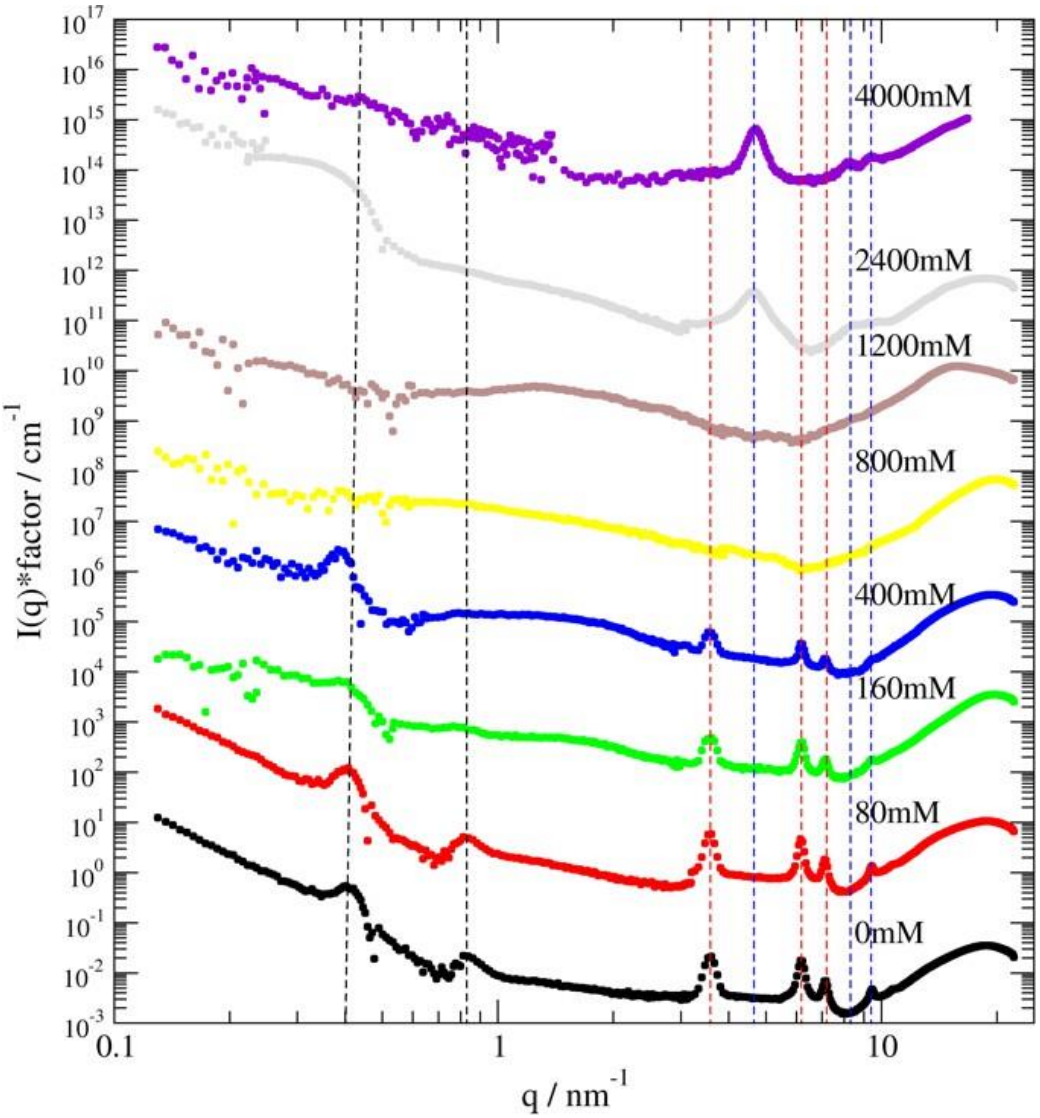

Fig. 25 SAXS curves for PASP+PLA (2mM PAAs concentration) PECs at different NaCl concentrations. Empty cell subtraction is done for all the curves. Black broken lines indicate planar structure peaks, red and blue broken lines indicate peak positions corresponding to Miller indices (h,k)=(1,1), (1,2) and (2,2). The planar structure peak (at low Qs) lattice constant is 15.5 nm from Equation (41). Hexagonal structure peaks (at high Qs) for low salt at 3.6 nm^{-1} represent a lattice constant of 2.0 nm, respectively for high salt at 4.7 nm^{-1} represent 1.54 nm.

With an α-helical pitch of 0.54 nm and 3.6 AAs per turn our PAA of 100 AA length should have a length of 15 nm which aligns closely with the observed 15.5 nm.

The broad additional peak observed consistently at around 20 nm^{-1} is potentially a water peak [100].

At medium salt concentrations, although no structural peaks were detected, a hump was observed around 1-2 nm^{-1}. This might indicate a liquid-like correlation peak between PAA coils, suggesting a transition to a more disordered or fluid state in the coacervate phase under these conditions.

Our interpretation, based on SAXS peak patterns, suggests a hexagonal structural formation with distinct planes, as displayed in Fig. 26. The observed plane lattice constant closely matches the α-helical length associated with a 100 AA sequence. The hexagonal lattice structure, with a constant of around 2 nm, seems to be an ideal fit for PLA with an outer diameter of the α-helix of 2 nm. The diameter of PASP with a short side chain is around 1 nm. A lattice constant of 1.54 nm appears to be between these cases, which could be realized if the side chains are not fully extended but folded onto the core of the α-helical backbone.

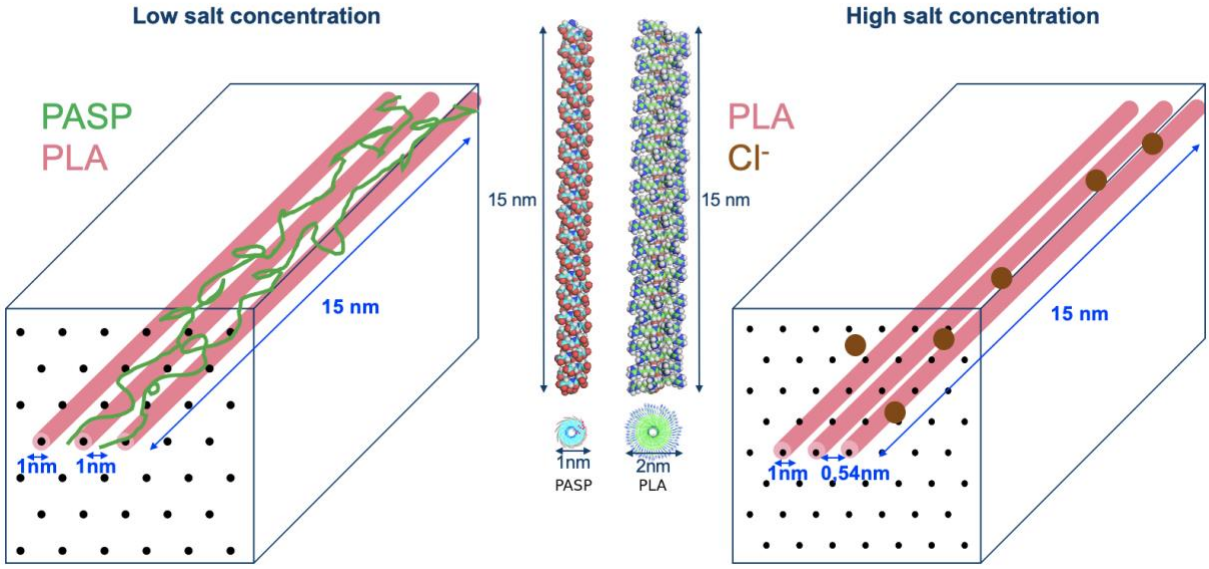

Fig. 26 Possible structure of PECs dense phase at low and high salt concentrations.

Referring to the illustrated models in the figure, the diameter values support our structural conclusions. Our NMR results play a crucial role in our interpretation; in particular cases, we identified an absence of PASP in the precipitate. This observation is crucial as it gives insights into the spatial arrangement and interactions within our samples.

By combining our findings from the NMR and SAXS measurements and integrating them with our understanding of typical PAA helix lengths, we can propose a specific structure and composition for our polymeric complexes. We hypothesize that at low salt concentrations, PLA α-helices are situated within the hexagonal lattice's primary plane. On the perpendicular plane, these helices are systematically aligned, with other PAA (PASP/PGA) or salt ions dispersed randomly in the surrounding matrix. In contrast, at high salt concentrations, our data suggests that PLA occupies the positions within the hexagonal structure, surrounded by Cl^- ions. This comprehensive analysis offers a picture of the structure and spatial distribution within our PEC samples.

To better understand the initial formation of structures in our samples, we conducted SAXS measurements without the centrifugation process. This was to determine if the observed structures were already present even at minimal amounts. Our findings are in Fig. 27. The presence of the high Q peaks even without centrifugation means that the observed structure is formed because of phase separation into PEC, and precipitating and centrifuging does not change the structure.

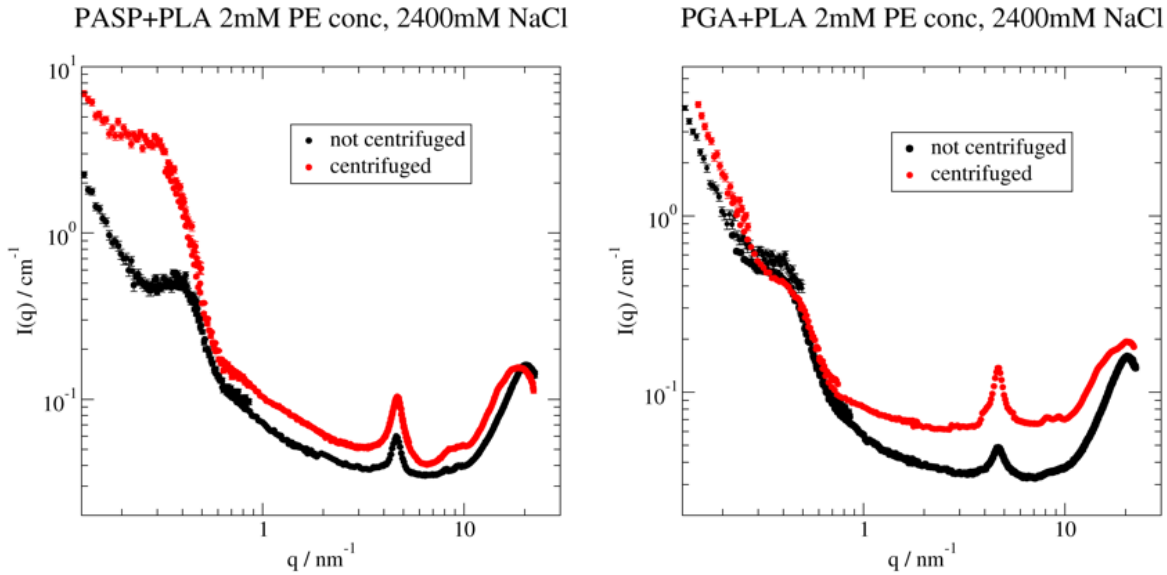

Fig. 27 SAXS curves for PASP/PGA+PLA PECs at 2400mM NaCl concentrations with or without centrifugation before the SAXS measurement. Empty cell subtraction is done for all the curves.

Different compositions

Additional experiments were performed to investigate the influence of different factors (such as different PAA, PAAs concentration and ratio, MWs, etc.) on the PECs structure.

Starting with PGA and PLA mixtures, the results at both 0 and 2400 mM NaCl concentrations are illustrated in Fig. 28 a, b. At low salt concentration the first peak appeared at 5.15 nm^{-1} followed by a second peak at 7.26 nm^{-1}. The peak position ratio of 1.41 corresponds more to a square lattice than to a hexagonal lattice (≈1.73). Also, a small indication for the third peak at 10.3 nm^{-1} is observed. The corresponding lattice constant is 1.22 nm and even smaller than the high salt PASP+PLA case. At low Q only a broad peak shoulder around or in between the first and second lamellar peaks is observed for low salt. At high salt the lamellar peaks seem to be broader and shifted to a bit larger distance.

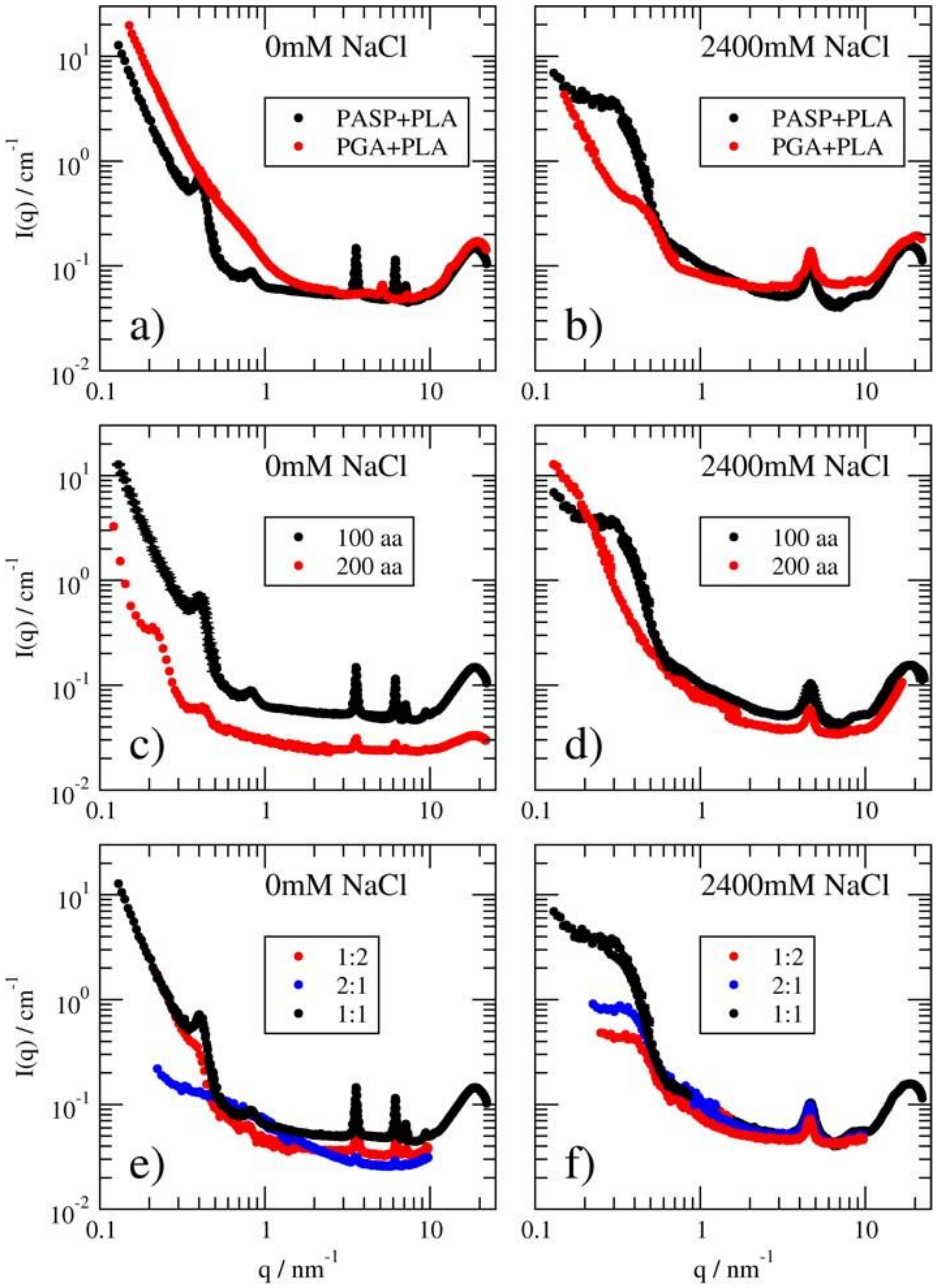

Fig. 28 SAXS curves for PECs with different composition. Empty cell subtraction is done for all the curves. (a) PGA+PLA vs PASP+PLA at 0 mM NaCl; (b) PGA+PLA vs PASP+PLA at 2400 mM NaCl; (c) PASP+PLA mixtures with 200 vs 100 AAs/chain PAAs at 0 mM NaCl; (d) PASP+PLA mixtures with 200 vs 100 AAs/chain PAAs at 2400 mM NaCl; (e) PASP+PLA at 1:1, 1:2 and 2:1 ratios at 0 mM NaCl; (f) PASP+PLA at 1:1, 1:2 and 2:1 ratios at 2400 mM NaCl.

To study the impact of MW, we measured samples with elongated chains, specifically those with 200 AAs per chain. These samples were compared to the previously studied 100 AAs/chain samples. As depicted in Fig. 28 c, d for PASP+PLA and Fig. S13 for PGA+PLA, while the high Q peak positions, corresponding to the hexagonal structure, remained consistent

across both chain lengths, a notable shift was observed in the low Q peaks towards lower Qs for the longer chains. The last result was expected for extended chains as the low Q peak position shows the length of α-helices.

The effect of AAs concentration and sample preparation methodologies on the PECs structure was also explored. As shown in Fig. S14 in Supplementary, the structure of PECs remained the same with a decrease in PAAs' concentration. Furthermore, as was mentioned before, when allowing samples to naturally precipitate over a span of 24 hours, without the application of centrifugation, the peak intensities were decreasing, while the peak positions, indicative of the structure, were retained (as shown in Fig. S15, Supplementary). This potentially underscores the stability of these structures.

We also investigated the structural changes with varying the PAAs' ratio. Our findings, confirming existing literature, showed that a 1:1 ratio maximizes PEC formation without introducing any structural variances, as illustrated in Fig. 28 e, f for PASP+PLA and Fig. S16 for PGA+PLA.

After our NMR findings that highlighted PLA's role in forming PECs, we measured SAXS of PLA solutions at 2400 mM NaCl concentration, for chain lengths of 100, 150, and 200 AAs/chain. Remarkably, all samples showed the same hexagonal peaks observed for PASP/PGA+PLA mixtures at high salt conditions, as presented in Fig. 29.

We also wanted to determine whether the PECs' structure would be the same at shorter chain lengths of 30 and 50 AAs per chain. However, the scattering profiles obtained for these lengths did not exhibit the characteristic features observed for longer chains, suggesting an absence of the previously identified structure (as shown in Fig. S17, Supplementary).

Mixing of PSSNa of 17500 Da (95 monomers per chain) to substitute PASP, and PLA with 100 AAs/chain at both 0 and 2400 mM NaCl did not show the same features at the SAXS measurements as we got from mixtures of PASP+PLA or PGA+PLA (Fig. S18).

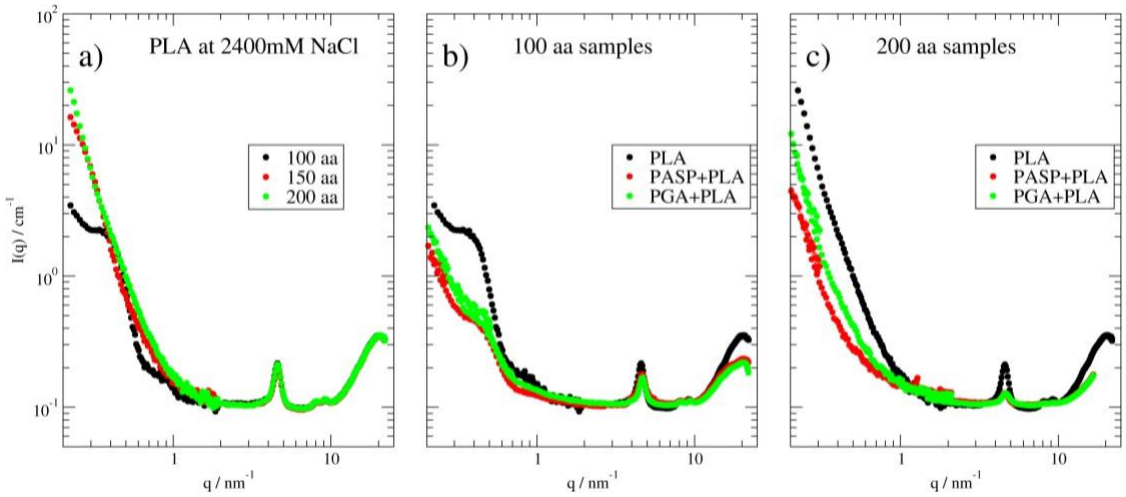

Fig. 29 SAXS curves for PECs at 2400 mM NaCl. Empty cell subtraction is done for all the curves. a) PLA samples at 100/150/200 AAs/chain; b) 100 AAs/chain samples of PLA, PASP+PLA and PGA+PLA; c) 200 AAs/chain samples of PLA, PASP+PLA and PGA+PLA.

Melting and recrystallization

The temperature dependence of the PECs structure was investigated to understand the phenomena of melting and recrystallization, with a goal of controlling and potentially enlarging the domain size of the crystals. For all measured samples, a characteristic result was identified: a distinct melting of PECs, observable through the disappearance of peaks in SAXS curves, indicative of a loss of structural integrity, at a certain threshold temperature upon heating. Interestingly, this was followed by a recovery of their structural formations upon cooling to the initial temperature. Fig. 30 shows one such set of measurements with PASP+PLA mixture with 100 AAs/chain and no salt, where the sample was heated from 15°C to 51°C and cooled down to 20°C to study the structural melting phenomena. Additional measurements at other NaCl concentrations are shown in Supplementary Fig. S19.

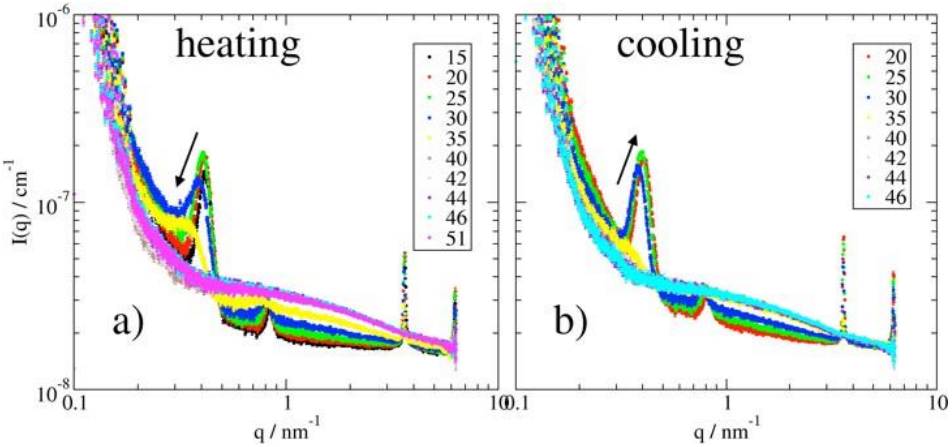

Fig. 30 SAXS curves for PASP+PLA at 0 mM NaCl. Empty cell subtraction is done for all the curves.

For this sample melting temperature was 42°C when the hexagonal peaks vanished in the SAXS measurement. With increasing salt concentrations, the transition temperature was decreasing (40-41°C for 80mM and already 37°C for 160mM NaCl) (see Fig. S19). At high salt concentrations the sample melting was observed at 45 and 60°C for 2400 and 4000mM salt concentrations, respectively.

Domain size during melting and recrystallization

From the scattering curves of temperature scans we can extract the lattice constant a from peak positions q [39] and the domain size d from the full width half maxima (FWHM) according to the Debye-Scherrer equation [101]:

$$\begin{gathered} lamellae\ (low\ Q\ peaks)\colon q_h = 2\pi h/a \\ hexagonal\ (high\ Q\ peaks)\colon q_{hk} = 4\pi\sqrt{h^2 + hk + k^2}/\left(\sqrt{3}a\right) \end{gathered} \tag{40}$$

where (hk) are the Miller indices for a crystal lattice plane.

$$d = {}^{2\pi}/_{FWHM} \tag{41}$$

Corresponding plots are presented in **Error! Reference source not found.** for 0 mM NaCl. W e observe an increase of the hexagonal lattice constant (as Qmax is decreasing) that results in more freedom for the AA sidechains or more space around the α-helices for counter ions. At low Q we observe first a linear increase of plane distance followed by a stronger linear increase above 35ºC. We cannot discriminate between an elongation of the α-helices and an increasing distance between the planes. We observe no significant difference between heating and cooling. The domain size shows different behavior for heating and cooling. The planar domain size that corresponds to

≈5 α-helix repeats reduces to ≈3 α-helix repeats again with a kink around 35ºC. The hexagonal domain size of about 55 lattice constants shows during heating an increase. At 35ºC a sudden jump is observed followed by a decrease of the domain size. This behavior indicates a kind of annealing approaching the melting temperature followed by a melting of the domain. For cooling we observe a grow of the domain size to values larger than the initial domain size. Below 30-35ºC a stable domain size is observed. The difference in domain size after cooling shows exemplary that the domain size can be tuned by careful melting and slow recrystallization short below the melting temperature.

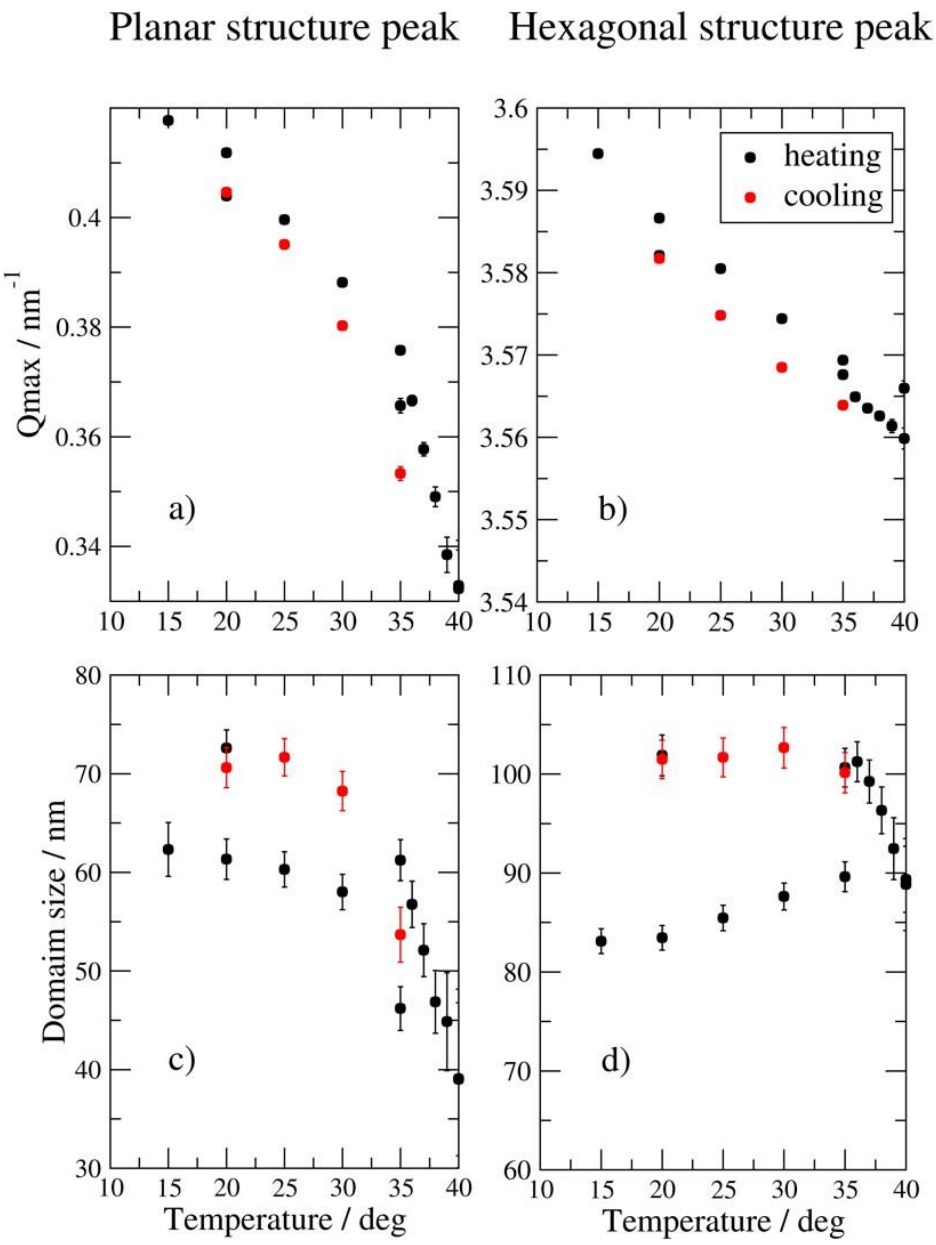

Fig. 31 Peaks' evaluation for PASP+PLA at 0 mM NaCl. a),b) Q value of the peak maximum at low Q values (planar structure peak, a), corresponding lattice constant at 20ºC is 15.3 nm from (41) and high Qs (hexagonal structure peak, b), corresponding lattice constant at 20ºC is 2.0 nm from (41); c),d) the domain size calculated using equation (42) and FWHM of the peak at low Q values (planar structure peak, c) and high Qs (hexagonal structure peak, d).

Scanning electron microscopy (SEM)

We successfully acquired scanning electron microscope (SEM) images of a PASP+PLA complex comprising 200 AAs at a concentration of 0mM NaCl (see Fig. 32). For sample preparation, we employed freezing individual droplets. The SEM image showed the internal structure of a fractured domain. The SEM image unveiled spherical domains with diameters

ranging between 20-30 nm, these are seemingly organized within larger spherical domains, extending up to 1 µm in diameter. The observed size of these larger structures aligns with the dimensions of previously observed droplets. As we move outside the Q range, particularly at the lower end, it is possible that what we see these condensed droplets, each containing multiple domains.

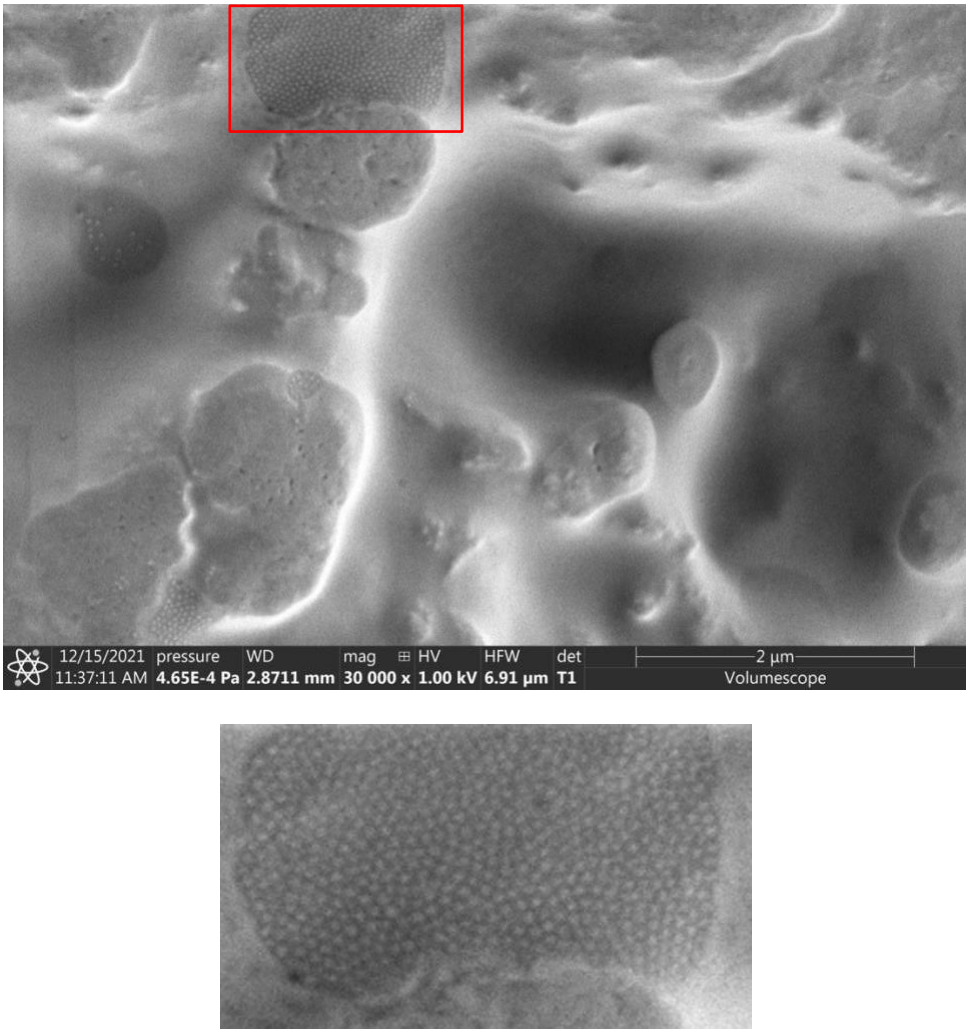

Fig. 32 SEM image of 200 AAs PASP+PLA 0mM NaCl sample. Second image – magnified red region.

Nevertheless, it is remarkable that the structure extends up to the micron scale. Upon observing the cross-section, it's intriguing to note a combination of hierarchical features resembling α-helices, 2D plane of hexagonal lattice, plane stacking forming a domain and liquid-like ordering of domains in a droplet. These characteristics could be a result of shearing during smearing the sample on the sample plate.

The observed 30-40 nm distance between α-helices (Fig. 32) aligns approximately with the domain size needed to yield the low Q peak width of the form we detected. Indeed, only with

a structure approximating this size, roughly twice the length of an α-helix, we observe these flat peaks.

Moreover, the space between the particles appears to be large enough to accommodate considerable amounts of water and salt. This suggests a distinct possibility that these substances could be present in volumes exceeding what can be incorporated into the unit cell. Further analysis and experiments are required to fully unravel these intriguing observations.

12.4.4. How to influence the structure of PECs

Shear orientation

The experiment was designed to evaluate the structural response and resilience of PECs, specifically PASP+PLA complexes with 200 AAs per chain at 0mM NaCl, under controlled thermal conditions and applied mechanical stress. This was done to study the stability and potential reorientation capacity of the helical and hexagonal components within the complexes. A sample of PASP+PLA at 0mM NaCl and 200 AAs per chain was melted in a capillary of 1.5 mm diameter. A second capillary of 1 mm diameter was inserted and rotated to apply shear to the sample between the two capillaries. Cooling was applied afterwards. Subsequent measurements were carried out using SAXS, during which the temperature was incrementally increased from 20°C to 60°C, then reduced back to 20°C in stages of 10 degrees each (refer to Fig. 33 and Fig. S21 in Supplementary).

The 2D SAXS images show an evident orientation within the sample, aligning with the rotational direction applied during the shearing process. This specific orientation was lost at 60°C, indicating a transitional phase, but it was recovered post-cooling.

This observation suggests the potential melting of the helices rather than the hexagonal structure, indicating a level of thermal resilience in the hexagonal lattice under these conditions. The detailed process and the findings from the temperature-dependent SAXS analysis provide significant insights into the behavior of the PECs under thermal variations and mechanical stress, enhancing our understanding of their structural stability.

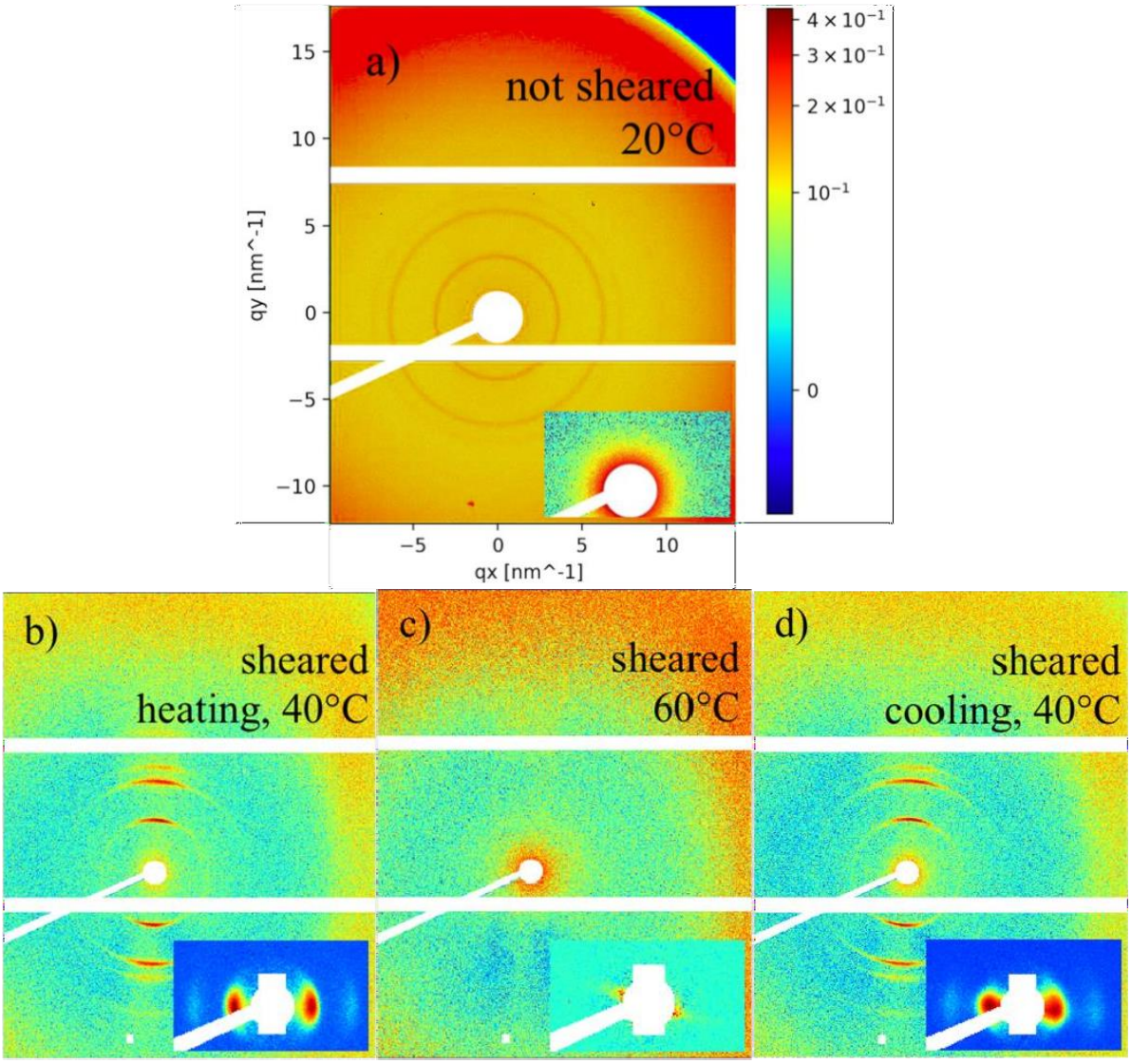

Fig. 33 Comparison of not sheared and sheared samples of PASP+PLA at 0mM NaCl, 200 AAs per chain. Insets – low Q images. a) not sheared sample; b) sheared sample at the heating stage at 40°C; c) sheared sample at 60°C; d) sheared sample at the cooling stage at 40°C.

While the application of shear force was explored for the samples with 0 mM salt concentration, it's important to note that this process was not observed for high salt concentration samples. There is a reasonable expectation that shearing might not have the same effects then. The chloride ions (Cl^-) prevalent in the precipitate at high salt concentrations are considerably smaller in size. This could potentially limit their ability to contribute to a stable structure under shear, and the process may not result in similar structural enhancements or orientation as observed in the low salt concentration samples. Further investigation would be required to confirm these hypotheses.

Magnetic field

The influence of a magnetic field on the orientation and enhancement of the structural integrity of PECs of PASP+PLA at 0 and 2400 mM NaCl concentrations was investigated. DNA fragments have been observed to align perpendicularly to the applied magnetic field, similar to the alignment behaviors observed in our PECs samples [102]–[104].

The samples were prepared in capillaries and centrifuged, with initial measurements taken using SAXS prior to exposure to the magnetic field (before magnetic field data).

Subsequently, these samples were subjected to a magnetic field of 14 Tesla and underwent a melting process therein at a temperature of 45°C. Following this, they were cooled down to 20°C and measured again using SAXS (after magnetic field data) to investigate the impact of the magnetic field on the structure (Fig. 34 and Fig. S22 in Supplementary).

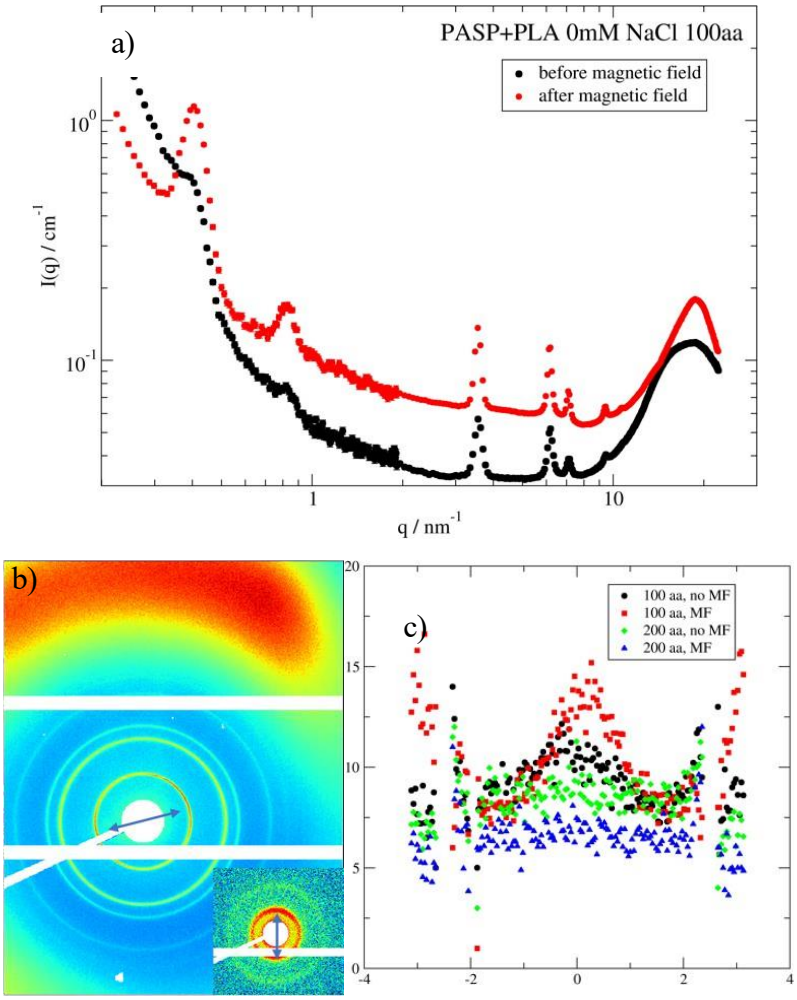

Fig. 34 Influence of the magnetic field on the PECs structure. a) SAXS data for PASP+PLA 0mM NaCl 100 AAs/chain sample before (black) and after (red) magnetic field. b) 2D image of this sample on SAXS after magnetic field for high Qs and low Qs (inset). c) Azimuthal average of the first low Q peak (at 0.2 nm^{-1}).

In the absence of salt, samples with 100 and 200 AAs per chain displayed an enhancement in their structures, as evidenced by increased peak intensities in particular for the low Q peak (Fig. 34 a) and Fig. S22). These samples were also observed to be oriented by the magnetic field, as visible at the 2D images and azimuthal averages of the peaks (Fig. 34 b) and c)).
Conversely, the high salt concentration sample demonstrated a counter-effect when subjected to the magnetic field (Fig. S22). The heating process within the magnetic field induced a disorder within the sample, suggesting a disruption of the ordered structure under these conditions. These findings reveal the complex interplay between salt concentration, magnetic field exposure and thermal fluctuations on the orientation and structural stability of PECs.

Crosslinking

Upon drying, the initially malleable precipitate of PEC transitions into a solid white substance, losing its ordered helical configuration. To preserve this structured arrangement after drying, the material underwent crosslinking by being exposed to a 2% glutaraldehyde solution. This procedure successfully retained the hexagonal helix pattern, evident in subsequent drying stages which resulted in a shift to a square cylinder assembly (Fig. 35). Remarkably, reintroducing moisture restored the original hexagonal structure. Dehydration highlighted specific peak positions at ratios $1:\sqrt{2}:2:\sqrt{5}$ indicative of a square columnar lattice of helices with a helix-helix distance of 1.66 nm, attributed to crosslinking efforts with glutaraldehyde. Our observations draw several parallels between PECs and collagen, notably in their helical structures. While PECs form double helices, collagen typically exhibits a triple helical structure [109]-[110]. Both structures are characterized by an extended chain conformation, demonstrating similar behavior in transitions and helix packing, albeit under different conditions. For instance, both undergo a coil-to-helix transition (melting) at 41°C, although this varies with the salt concentration for PECs. The helices pack into a hexagonal arrangement at low salt concentrations and transition to a quadratic form at high concentrations, whereas collagen retains a nearly hexagonal pattern. Cross-linking stabilizes these structures, using glutaraldehyde for PECs and ester formation in collagen.
These similarities open further research on biomimetic potential and applications.

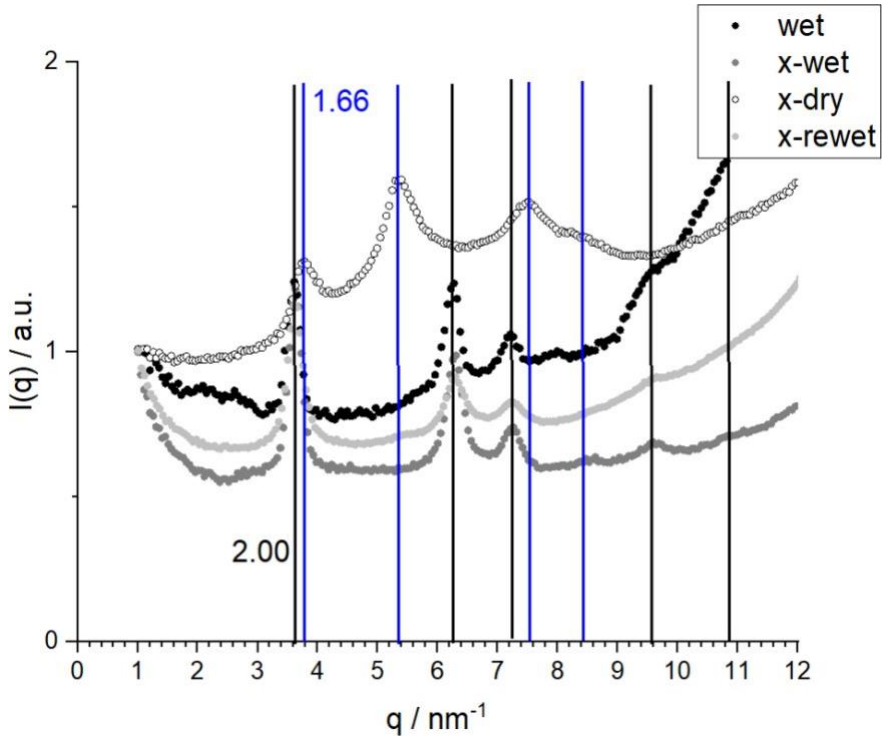

Fig. 35 SAXS data for PASP+PLA 0mM NaCl 100 AAs/chain sample crosslinked with a 2% glutaraldehyde solution in dry and hydrated states.

12.5. Conclusion

In this chapter, we investigated the structure of PECs formed by mixing two oppositely charged PAAs. We explored the influence of various factors such as pH, salt concentration, temperature and PAAs concentrations on the state and structure of the complexes.

Our findings revealed that salt concentration played a crucial role in the formation and structure of PECs. At low and high salt concentrations solid precipitates were observed, while at intermediate salt concentrations a liquid coacervate phase without internal structure was formed. The addition of salt led to the formation of aggregates in the system.

Through NMR experiments, we identified that the white precipitate mainly consisted of the positively charged PLA when no salt was present. At high salt concentrations, the negatively charged PASP or PGA remained in the supernatant, indicating the formation of a compound between PLA and oppositely charged chloride ions from the NaCl salt.

Optical microscopy allowed us to observe the phase separation of the complexes. At low and high salt concentrations, white sticky precipitates were formed, while at intermediate salt concentrations, spherical droplets (coacervates) were observed. SAXS experiments provided insights into the structure of the PECs. The presence of hexagonal peaks in the SAXS curves

suggested a hexagonal packing of PLA α-helices in the nodes of the lattice, with other PAAs or salt ions randomly distributed around except for PGA+PLA where a square lattice was observed.

The structure we discovered is organized in α-helices assembled into hexagonal or square arrays, the similar packaging is observed for tropocollagen. This important finding is a key part of developing materials that mimic natural substances, like collagen, showing new ways to create materials that resemble the structural characteristics found in nature.

We also investigated the influence of different factors such as PAA composition, concentration, molecular weight and PAA ratio on the PECs structure. The results showed that the PECs maintained a similar hexagonal structure regardless of the variations in these factors. Changes in PAAs concentration, centrifugation or PAA ratio did not significantly affect the structure.

Additionally, we examined the melting behavior of the PECs with temperature. The structures of the PECs melted at specific temperatures upon heating and recovered their structure upon cooling. The melting temperature varied with salt concentration, with higher salt concentrations leading to lower melting temperatures.

Finally, we explored the effects of shearing and magnetic fields on the structure of the PECs. Shearing of the PECs resulted in a loss of orientation at high temperatures but regained orientation during cooling. The application of magnetic field enhanced the structure of PECs at low salt concentrations but disrupted the structure at high salt concentrations.

In conclusion, our study provides valuable insights into the structure of PECs and the factors influencing their formation. Understanding the structural properties of PECs is crucial for their potential applications in various fields, including biomedical engineering, drug delivery and water treatment. Further research is needed to explore the mechanical properties and stability of these complex systems and to investigate their performance in specific applications.

13. Conclusions

In this thesis, we have explored the dynamics and structure of polyelectrolytes (PEs) and polyelectrolyte complexes (PECs). The research began with understanding the behavior of polystyrene sulfonate (PSS), a classical PE, challenging existing theories and uncovering new insights into the role of hydrodynamic interactions in their dynamics. We have shown that charged PEs exhibit complex behavior influenced by various factors, including ionic strength and molecular structure.

On larger scale of PE chain size, the polymer dynamics can be described within a colloidal picture of charged chains. Different from previous hypotheses, the hydrodynamic interactions between chains are not fully screened and are essential to understand the connection between collective diffusion, self-diffusion and chain dynamics. The PE charges result in an increased end-to-end distance. On an intermediate scale larger than tens of monomers, the dynamics of the PE chain aligns with what we expect for segmental motion from theoretical models like the Zimm model. However, when we examine shorter length scales of a few monomers, particularly at the level of neighboring monomers, we see that their movement is much slower. This slowdown is due to internal friction between neighboring monomers, which is caused by the way counterions condensate on the polymer. We observed that the dynamics of a charged PE on a segmental level follows a neutral chain Zimm model with internal friction (ZIF).

Continuing with PECs, we examined the influence of environmental variables like pH, salt concentration and temperature on their formation and stability. Our findings have demonstrated that the formation of PECs is not just a simple interaction of oppositely charged poly amino acids (PAAs) but a complex process influenced by various factors like PAA concentration, molecular weight and external forces such as shearing and magnetic field.

Our observations indicate that salt concentration plays a crucial role in determining the behavior of PECs. Consistently, phase separation occurs, leading to different physical states depending on the salt concentration. At low and high salt concentrations, solid precipitates were observed, while at intermediate salt concentrations, a liquid coacervate phase without internal structure was formed. The addition of salt led to the formation of aggregates in the system.

SAXS experiments and optical and electron microscopy observations provided insights into the structure of the PECs. The formation of high-density droplet phases and self-assembled hexagonal lattices built of parallel α-helices are main findings, highlighting the influence of

factors like molecular weight and pH on the self-assembly process. Stacking of planar layers was also observed, contributing to our understanding of the structural arrangement within these complexes. The presence of hexagonal peaks in the SAXS curves suggested a 2D hexagonal packing of PLA α-helices in the nodes of the lattice, while low Q planar peaks suggest additional planar layering perpendicular to the hexagonal layers with α-helical distance. Other PAA (PASP) or salt ions were randomly distributed around α-helices. Hexagonal peak positions indicated a 2 nm lattice constant between the nodes in hexagonal packing at low NaCl concentrations while the second length scale corresponded to a planar stacking with ~15.5 nm lattice constant. At high salt concentrations the hexagonal lattice constant shifts to 1.54 nm and the planar ordering stays around 15.5 nm. For PGA+PLA a square lattice was observed. The PECs maintained a similar hexagonal structure regardless of the variations in PAA composition, concentration, molecular weight and PAA ratio.

Melting of the PECs at a temperature of 42°C was observed at 0 mM NaCl concentration. The melting temperature was decreasing with increasing NaCl concentration (40-41°C for 80 mM and already 37°C for 160 mM NaCl). At high salt concentrations the sample melting was observed at 45 and 60°C for 2400 and 4000 mM salt concentration, respectively. The PECs recrystallized after melting upon cooling with increased domain size which opens a way for further applications where enlarged domain structure plays an important role.

Finally, we explored the effects of shear and magnetic field on the structure of the PECs. Applying the shear forces leads to orientation of the PECs in the rotational direction. This specific orientation disappears at 60°C, indicating a structural transition. Interestingly, the orientational ordering recovers at further cooling.

The application of a magnetic field enhanced the structure of PECs at low salt concentrations but disrupted the structure at high salt concentrations. In general, the effect of magnetic field was found to be less pronounced than mechanical orientation upon shearing.

In conclusion, this thesis has not only contributed to a deeper understanding of PEs and PECs but also provided new insights for future research that could lead to innovative applications of them, enhancing their effectiveness in various scientific and industrial fields. Based on the findings with PSS, future research could explore transitioning to more complex PEs like PAA (e.g., poly(L-aspartic acid) or PASP). This shift could provide insights into simple protein polymers with specific repeating units (e.g. two amino acids repeating), potentially leading to applications in biocompatible materials and advanced drug delivery systems.

For PECs there is a potential for developing fibrous materials. First attempts of linking PECs were done and first solid samples were prepared, after some mechanical experiments on their stretching and shearing can be done. Such fibers could have applications in tissue engineering or as novel materials in textile industries, where the unique properties of PECs could be used for specific functional and structural advantages.

14. Acknowledgments

Firstly, I would like to thank our head of JCNS-1 institute, Prof. Dr. Stephan Förster, whose expertise and insights have been invaluable throughout this process. He provided not only technical guidance but also encouraged me to think critically and creatively. Special thanks to Prof. Walter Richtering from the Institute of Physical Chemistry, for being the second referee of this work.

I deeply appreciate the guidance and expertise shared by my supervisors, Margarita Kruteva and Ralf Biehl from JCNS-1. Their readiness to impart their extensive knowledge on the topic were invaluable to my research progress. Their mentorship not only broadened my understanding but also enhanced my skills in the field, for which I am very grateful.

Special thanks to the technical and scientific staff at the institutes and facilities that have been part of this research. In particular, I am grateful to Ingo Hoffmann at ILL in Grenoble for his introduction to neutron spin-echo technique, to Aurel Radulescu at MLZ in Garching for his supervision of my SANS experiments, and to Martin Dulle for his assistance with SAXS measurements in Jülich. Their assistance was crucial in mastering the techniques that formed the backbone of my experimental work.

I must also thank Beate Förster, for her assistance with the SEM measurements, and Jürgen Allgaier, for his help and support during NMR experiments. Their willingness to share their knowledge and time has been a great help.

To my colleagues in Jülich for their advices, discussions and moral support throughout this journey, lunches and activities after work together. Special mentions to my office mates Igor Graf von Westarp and Luman Haris, for their companionship during breaks that provided much-needed conversations and laughter. To Vladislava Fokina, Ekaterina Kostyurina and Dmitrii Vinogradov for their support.

Lastly, but most importantly, I thank my family and friends in Russia for their morale support and visiting me in Germany during my PhD time. Their belief in me has been a constant source of strength and motivation.

15. Eidesstätliche Erklärung

Ekaterina Buvalaia erklärt hiermit, dass diese Dissertation und die darin dargelegten Inhalte die eigenen sind und selbstständig, als Ergebnis der eigenen originären Forschung, generiert wurden.

Hiermit erkläre ich an Eides statt

1. Diese Arbeit wurde vollständig oder größtenteils in der Phase als Doktorand dieser Fakultät und Universität angefertigt;
2. Sofern irgendein Bestandteil dieser Dissertation zuvor für einen akademischen Abschluss oder eine andere Qualifikation an dieser oder einer anderen Institution verwendet wurde, wurde dies klar angezeigt;
3. Wenn immer andere eigene- oder Veröffentlichungen Dritter herangezogen wurden, wurden diese klar benannt;
4. Wenn aus anderen eigenen- oder Veröffentlichungen Dritter zitiert wurde, wurde stets die Quelle hierfür angegeben. Diese Dissertation ist vollständig meine eigene Arbeit, mit der Ausnahme solcher Zitate;
5. Alle wesentlichen Quellen von Unterstützung wurden benannt;
6. Wenn immer ein Teil dieser Dissertation auf der Zusammenarbeit mit anderen basiert, wurde von mir klar gekennzeichnet, was von anderen und was von mir selbst erarbeitet wurde;
7. Teile dieser Arbeit wurden zuvor veröffentlicht und zwar in:

Ekaterina Buvalaia, Margarita Kruteva, Ingo Hoffmann, Aurel Radulescu, Stephan Förster, and Ralf Biehl, ACS Macro Letters 2023 12 (9), 1218-1223, DOI: 10.1021/acsmacrolett.3c00409

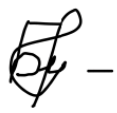

21/05/2025

Datum

Unterschrift

16. Supplementary

16.1. Detailed analysis of PE scattering curves

In this section, the structure and dynamics of polystyrene sulfonate (PSS) are examined using various scattering techniques. PSS serves as a classical model polyelectrolyte (PE) to study hydrodynamic interactions (HIs) and internal friction. The experiments include small-angle X-ray (SAXS) and neutron (SANS) scattering, neutron spin-echo (NSE) spectroscopy and dynamic light scattering (DLS). Results demonstrate the collective diffusion and self-diffusion behaviors of PSS in both dilute and semi-dilute regimes, highlighting the impact of salt concentration on the polymer conformation and dynamics.

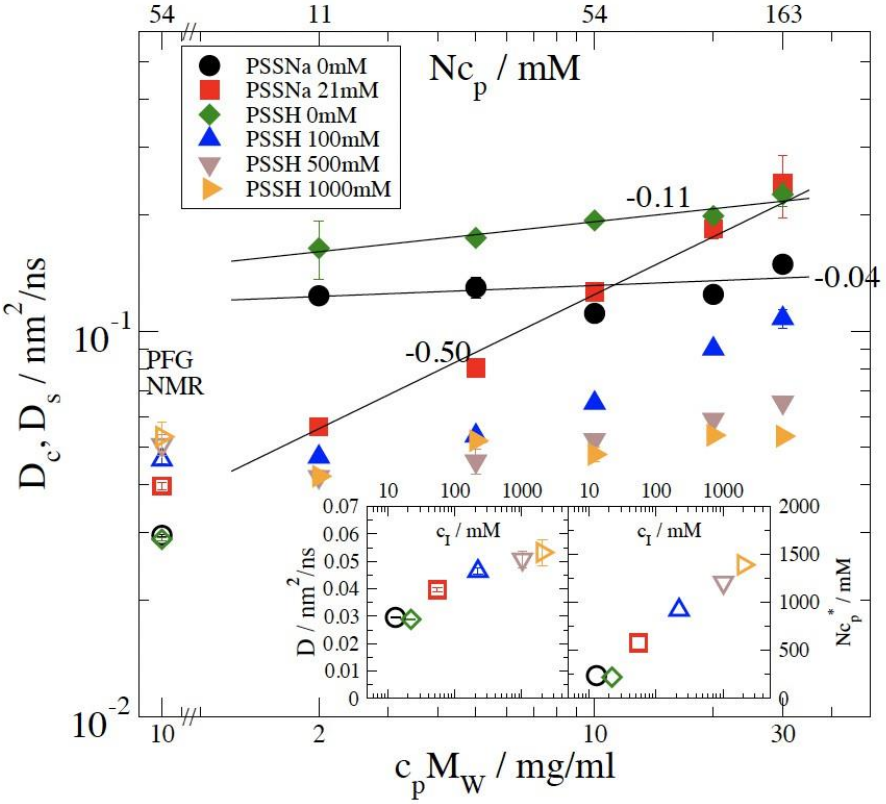

Fig. S1 Collective diffusion coefficient D_C measured by DLS (fast mode, solid symbols) and self-diffusion D_S (open symbols, conc.=10 mg/ml) measured by PFG-NMR for PSS 17.5k. The PFG-NMR X-axis position reflects a low concentration where D_C should equal D_S. Lines describe power laws with indicated powers. The left inset shows the PFG-NMR measured self-diffusion D_S plotted against the ion concentration assuming a PSS effective dissociation rate of 8% [94] and ions from water dissociation according to a measured pD 1.8 at 10 mg/ml. Right inset: Monomer overlap concentration Nc_p^* calculated from D_S (see below). All concentrations are below Nc_p^*.

Overlap concentrations

Neutral polymer solutions are categorized in 3 different concentration regimes: dilute, semidilute and entangled/concentrated [41]. In the dilute region polymers are separate and polymer interactions have a small effect. PEs in dilute conditions at low ionic strength show electrostatic repulsion leading to an electrostatically correlated dilute regime not present for neutral polymers. The semidilute regime is characterized by overlapping coils without entanglements of the polymer. The crossover from dilute to semidilute happens when the occupied polymer volumes fills the sample volume. The polymer coils start to overlap at a monomer concentration $c^* \approx N/R_g^3$ for polymers with polymerization degree N [105]. Corresponding polymer concentration are $c_p^* = c^*/N \approx 1/R_g^3$. Monomer overlap concentrations Nc_p are given for easier comparison to other work e.g. to Lopez [105].

From measured self-diffusion coefficient D_s we can calculate the radius of gyration R_g using $R_g^2 = 6R_e^2$ with $D_S = D_Z = 0.196\,kT/(\eta_S R_e)$ and determine c_S.

Table S1 Monomer overlap concentrations Nc_p^* from D_s measured at 10mg/ml in units mM. For 30mg/ml the additional counterions and changed pD are considered by linear interpolation of 10 mg/ml data. The monomer concentration for later NSE measurements 39k and 17.5k is 163 mM corresponding to 30mg/ml.

sample	PSSNa 0 mM	PSSNa 21 mM	PSSH 0mM	PSSH 100 mM	PSSH 500 mM	PSSH 1M
c_I at 10mg/ml mM	13	55	22	222	1022	2022
Nc_p^* for 39k	14	55	41	214	416	605
Nc_p^* for 17.5k	238	577	221	922	1209	1392
c_I at 30mg/ml mM	41	83	50	250	1050	2050
Nc_p^* for 39k	49	82	53	222	421	-
Nc_p^* for 17.5k	440	636	534	933	1214	-

Lopez examined scattering data (SAXS and light scattering) and viscosity data of PSSNa for different polymerization degree N yielding master curves of $c^* = 1750N^{-2}$ and $c^* = 3600N^{-2}$ at low ionic strength [105]. For N = 212 these results in Nc_p^* values of 39 mM or 80 mM while for N = 95 resulting values are 194 mM and 400 mM, respectively. We find reasonable agreement to these values considering that lowest ionic strength is difficult to achieve.

*

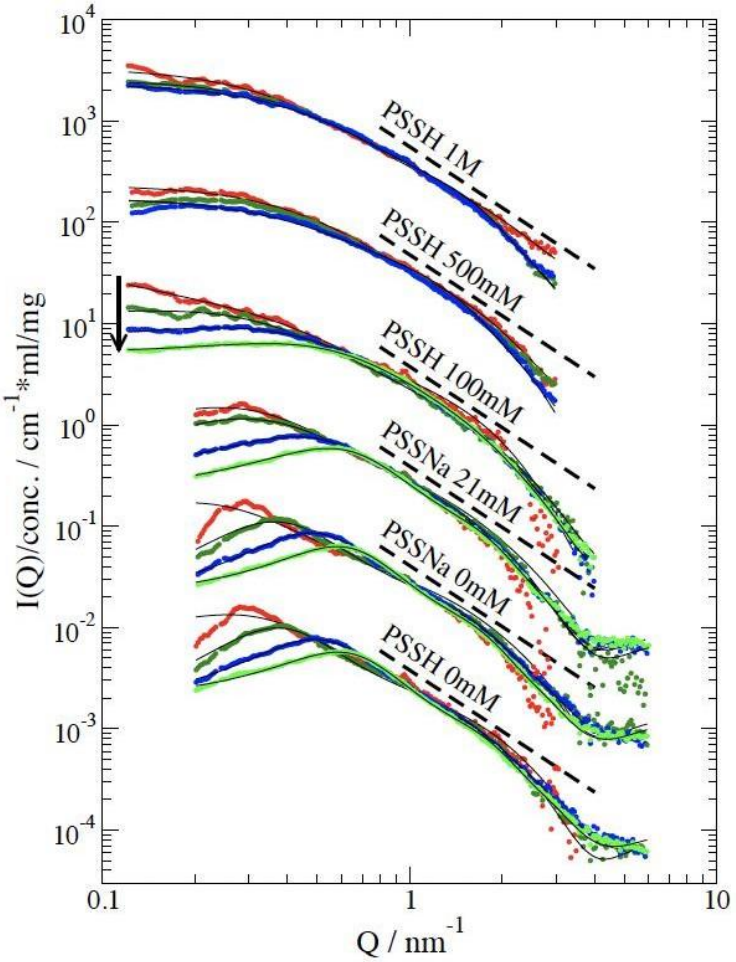

Fig. S2 SAXS data for PSS 17.5k. All measurements were background corrected and scaled by concentration (c_s shifted consecutively by 10 for visibility). Concentrations were 5, 10, 20, 30 mg/ml (colors red to green, along arrow). Black lines correspond to fits as described in main text. See Fig. 17 in main text.

SAXS model

Generalized Gaussian worm

The formfactor of a generalized Gaussian chain is [106]

$$F_g(Q,R_g,\upsilon) = \frac{1}{\upsilon U^{\frac{1}{2\upsilon}}}\gamma_{inc}\left(\frac{1}{2\upsilon},U\right) - \frac{1}{\upsilon U^{\frac{1}{\upsilon}}}\gamma_{inc}\left(\frac{1}{\upsilon},U\right)$$

with $U = \left(QR_g\right)^2$ and the lower incomplete gamma function γ_{inc}. R_g is the radius of gyration and υ the excluded volume parameter.

If the contour length L is much larger than the cross section, the cross section can be separated in a decoupling approximation like the for a wormlike chain [107]. The Gaussian worm formfactor reads:

$$F(Q) = \rho^2 V^2 F_g(Q,R_g,\upsilon)\cdot F_{disc}(Q,R)$$

with $F_{disc}(Q,R) = \frac{J_1(QR)}{QR}$, $J_1(x)$ as first order Bessel function and ρ as contrast of the worm with volume $V = \pi R^2 L$.

Two Yukawa SF

The double Yukawa potential of a particle with radius R at position r' is

$$V(r)/kT = \begin{cases} \infty, & r \leq 1 \\ -K_1\left[\frac{e^{-z_1(r-1)}}{r}\right] - K_2\left[\frac{e^{-z_2(r-1)}}{r}\right], & r > 1 \end{cases}$$

with $z_i=1/\sigma_I$ as inverse screening length (σ_I as screening length), reduced distance r=r'/R and potential K_i at the surface. For K>0 we have attraction while K<0 means repulsion.

Liu et all describe the corresponding structure factor $S(Q)$ within the MSA closure [36].

Diffuse scattering

Diffuse scattering d(Q) describes contributions from inhomogeneities or deviations from a smooth shape like the Gaussian worm assuming statistical independence and a characteristic length σ [39].

$$d(Q,\sigma) = A(1 - e^{-Q^2\sigma^2})$$

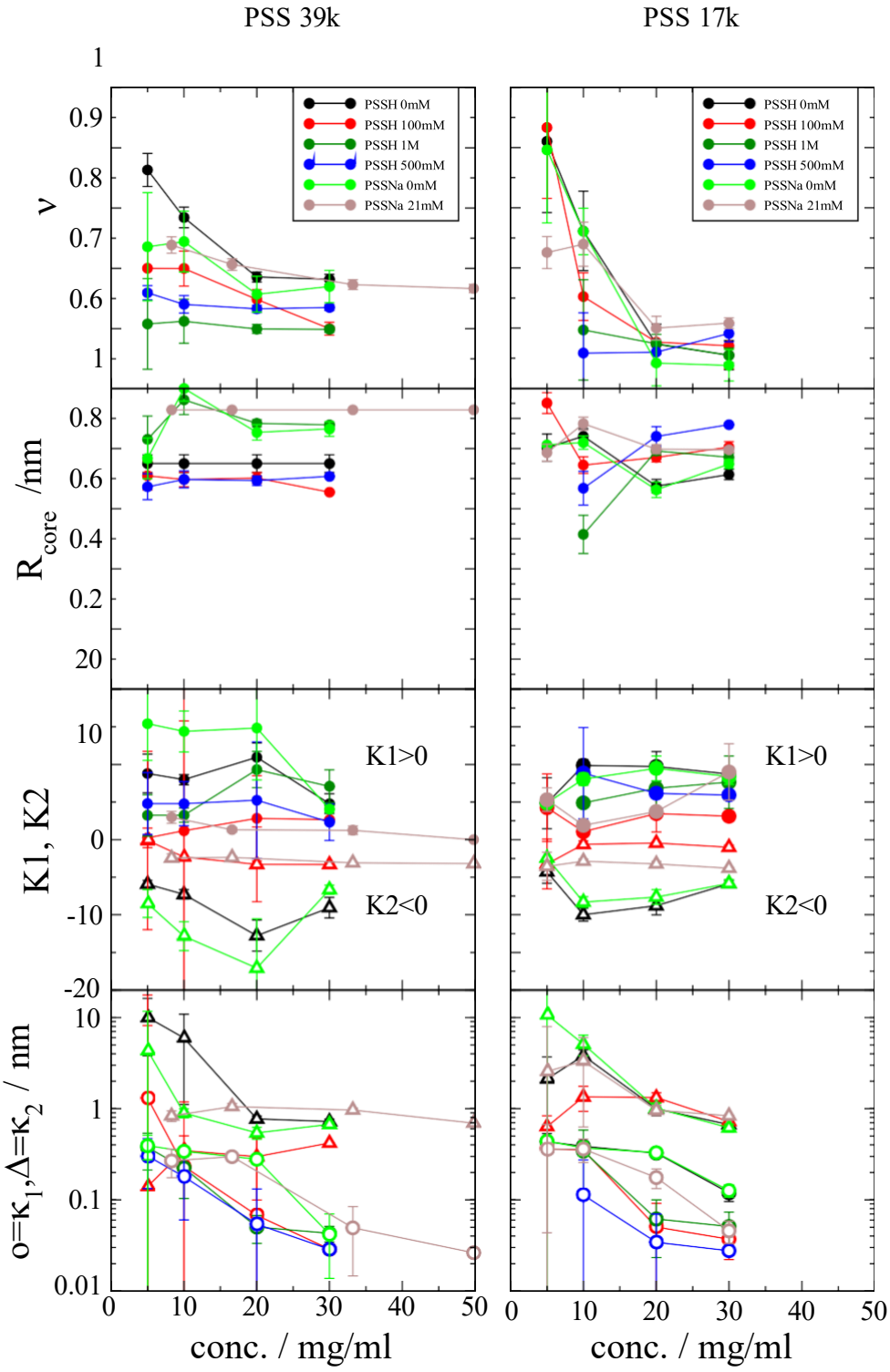

Fig. S3 Relevant SAXS fit parameters for the generalized Gaussian worm (R_{core}, excluded volume parameter υ) and for the two-Yukawa potential (screening length κ_1, surface potential K_i in units kT). $K_1>0$ with short range κ_1 describes attraction, while K_2 describes electrostatic repulsion. Characteristic length of diffuse scattering σ resulted in values between 0.2-0.9 nm of varying intensity which might also include background contributions.

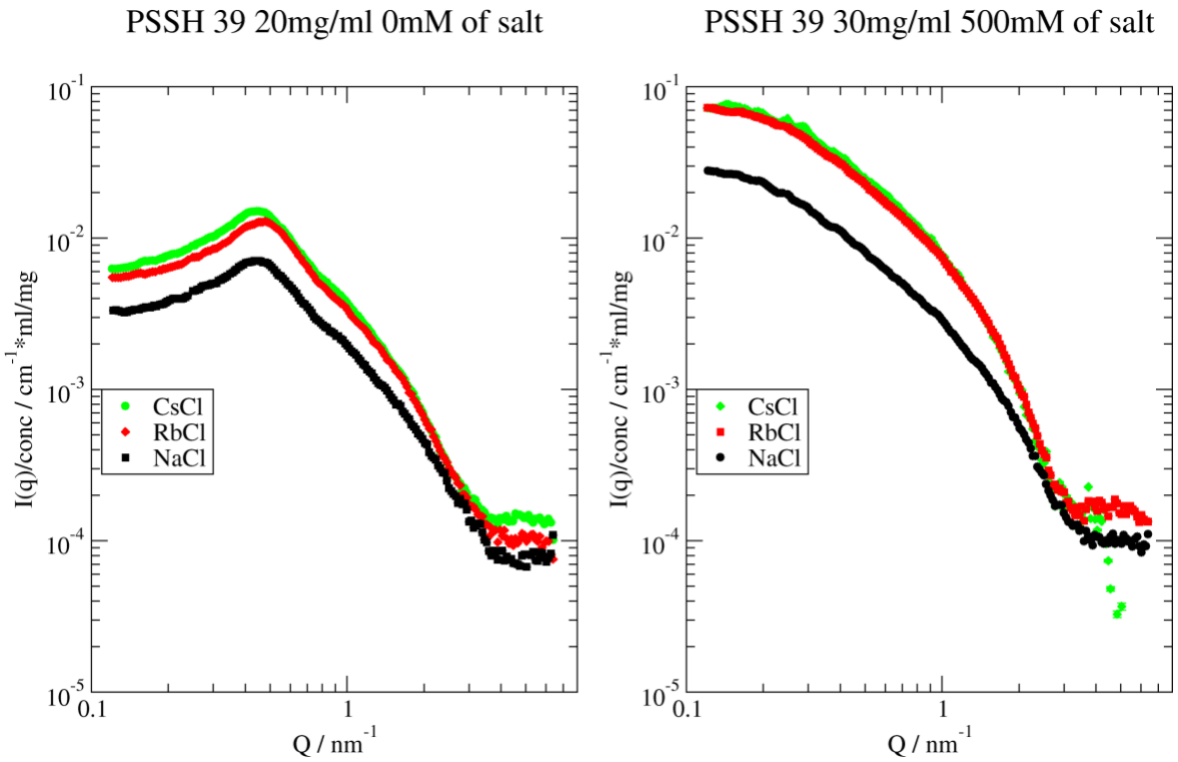

Fig. S4 SAXS data for PSS 39k in NaCl, RbCl and CsCl salts after background correction and scaled by concentration. A stronger SF results mainly in the decreased intensity at low Q depending on the salt used. Measured at inhouse instrument SAXSpace (Anton-Paar).

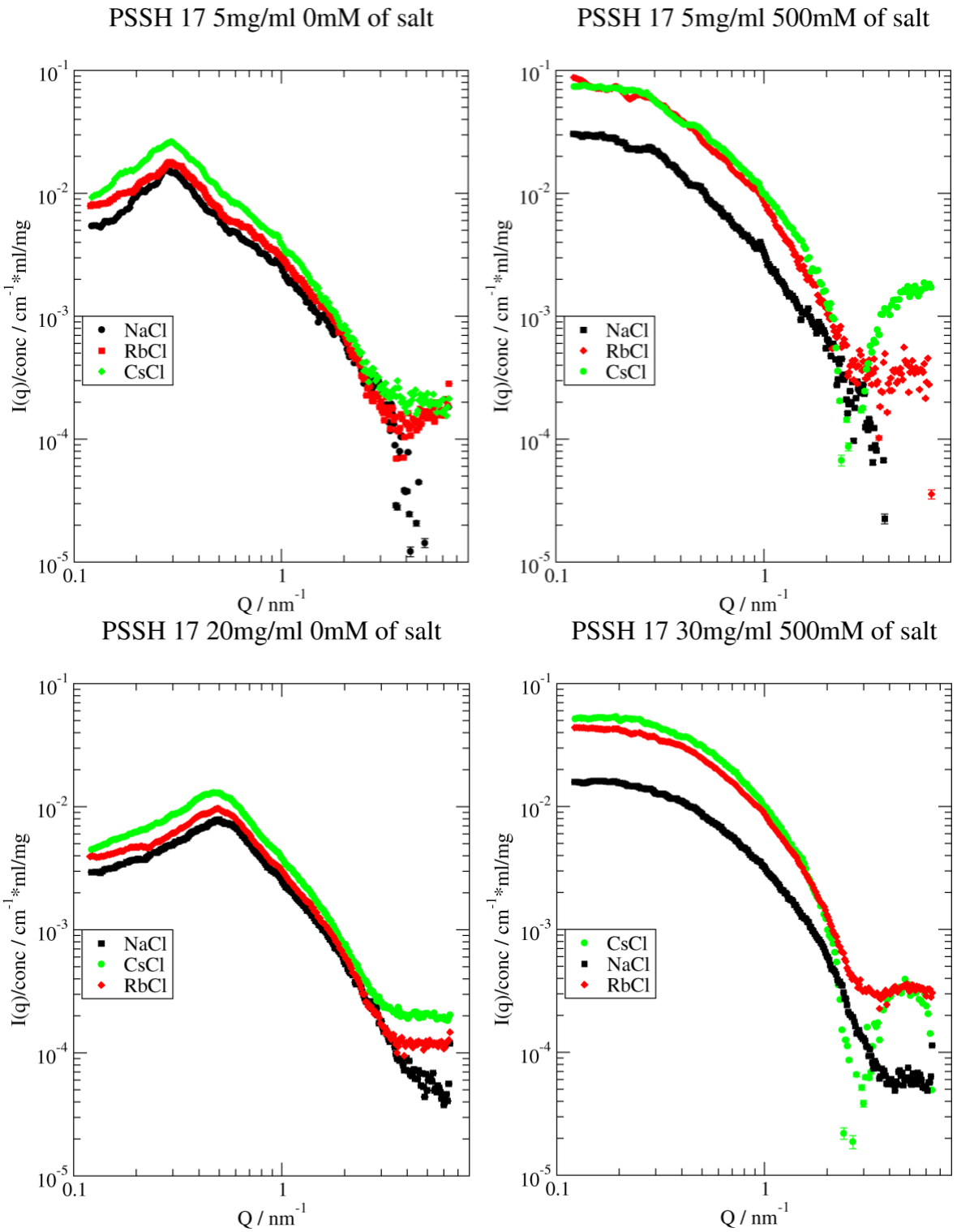

Fig. S5 SAXS data for PSS 17.5k in NaCl, RbCl and CsCl salts after background correction and scaled by concentration. A stronger SF results mainly in the decreased intensity at low Q depending on the salt used. Measured at inhouse instrument SAXSpace (Anton-Paar).

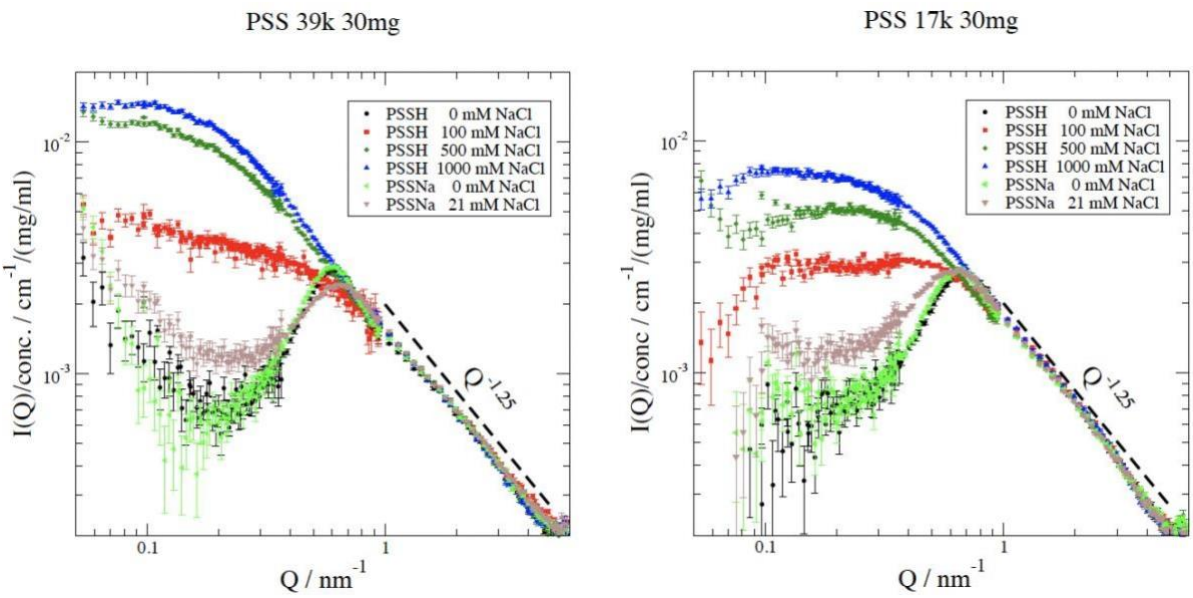

Fig. S6 SANS data at T=20ºC for PSS 39k (left) and 17.5k (right) after background correction and desmearing measured at KWS2, MLZ, Garching [79]. For 17.5k a small increase in slope at larger Q is visible that might also be an indication of the disclike formfactor observed in SAXS. For 39k at low Q we observe for low salt concentrations an upturn caused by the presence of aggregates also visible in DLS as the slow mode.
Extrapolating this contribution to the NSE Q range shows that the slow mode is negligible in the NSE signal. For 17.5k the contribution is even smaller. The data are corrected for instrumental resolution using the Lake algorithm that instrumental resolution does not affect the shown data or the observed power law.

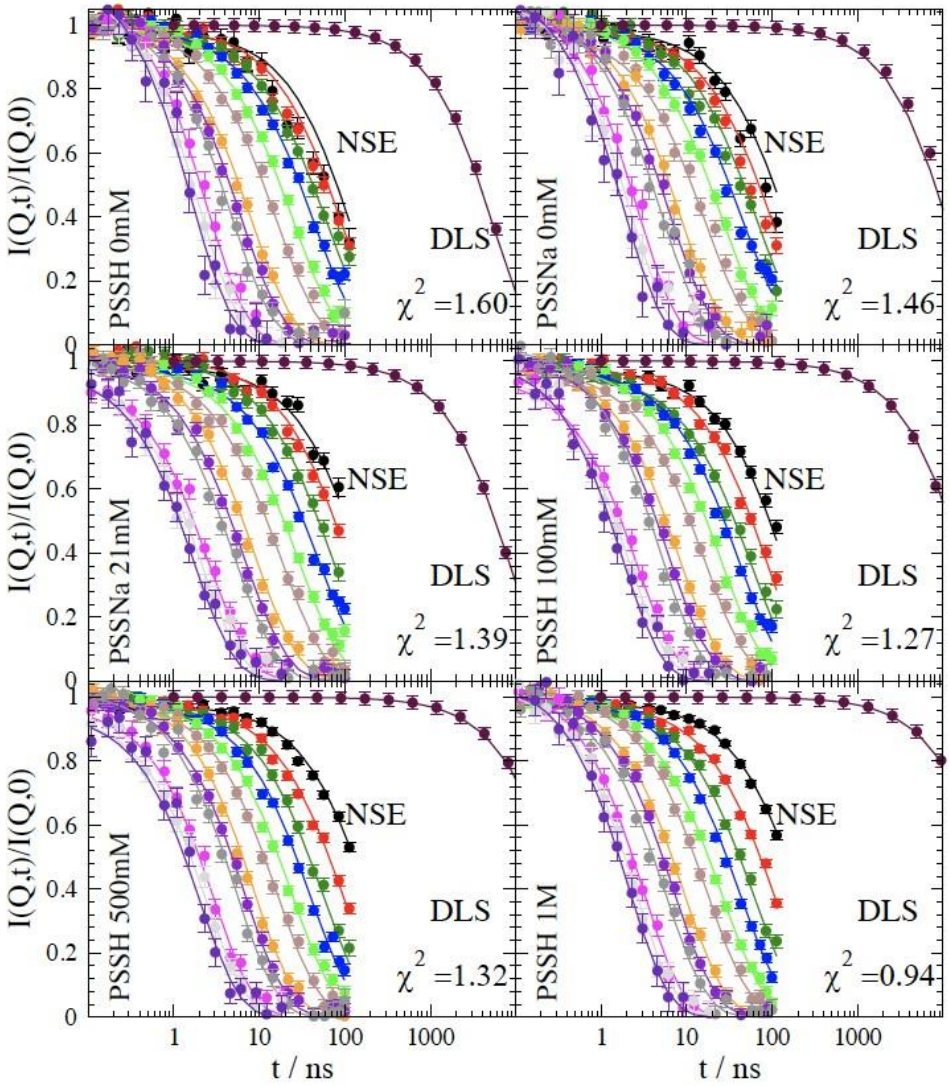

Fig. S7 NSE measured intermediate scattering function $I(Q,t)/I(Q,0)$ up to 100 ns for PSS 39 kDa at 30 mg/ml measured at IN15, ILL, Grenoble. Q values as shown in main text. We add a synthetic Q=0.0264 nm^{-1} dataset that represents a field correlation function g_1(Q,t) with the measured collective diffusion coefficient from DLS at the same concentration. The synthetic dataset was created with same number of points as the lowest Q NSE measurement and approximately same error bars. This results in a weighing of the DLS values equal to the lowest NSE Q value together with a small influence on χ^2. Solid lines represent the combined fit using the $H(Q)/S(Q)$ corrected ZIF model with in general small χ^2.

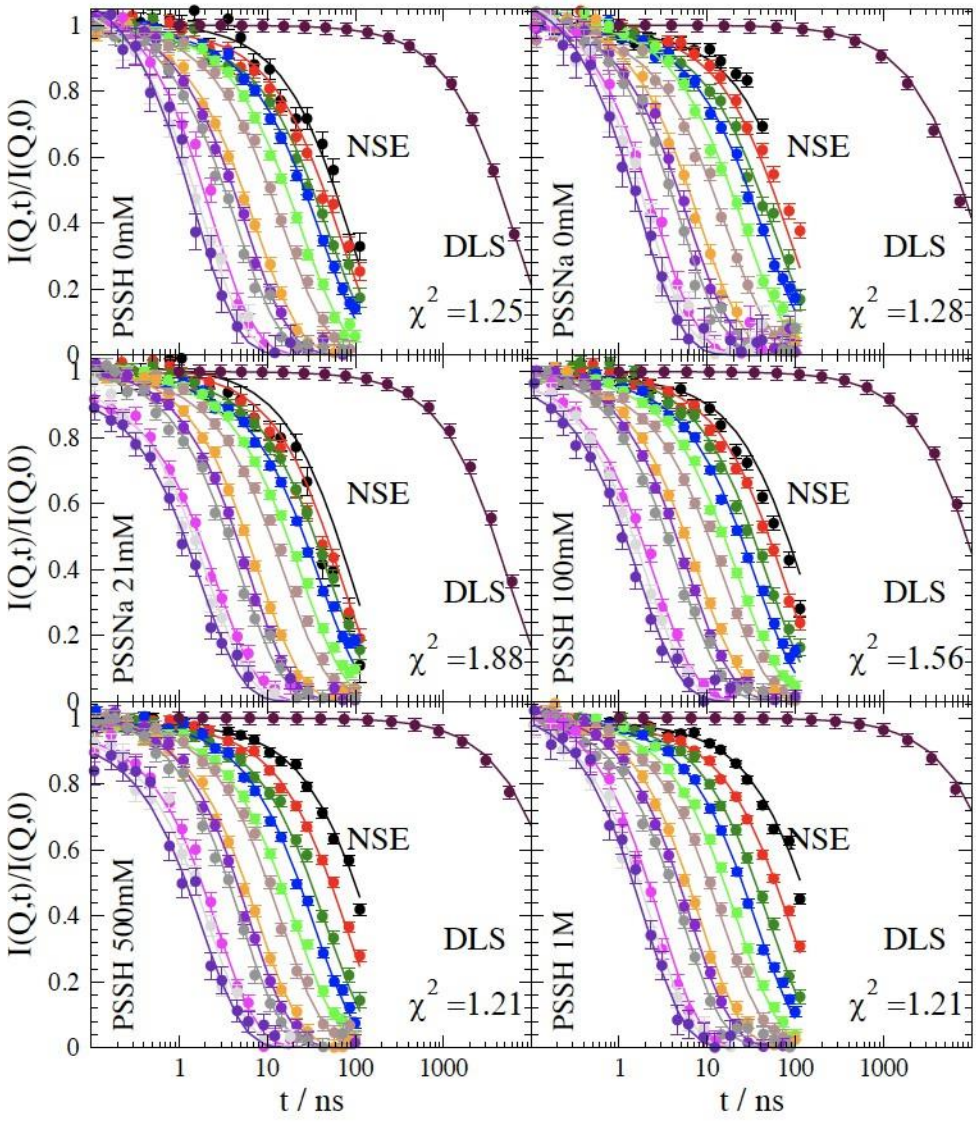

Fig. S8 NSE measured intermediate scattering function $I(Q,t)/I(Q,0)$ up to 100 ns for PSS 17.5 kDa at 30 mg/ml measured at IN15, ILL, Grenoble. See description Fig. S7.

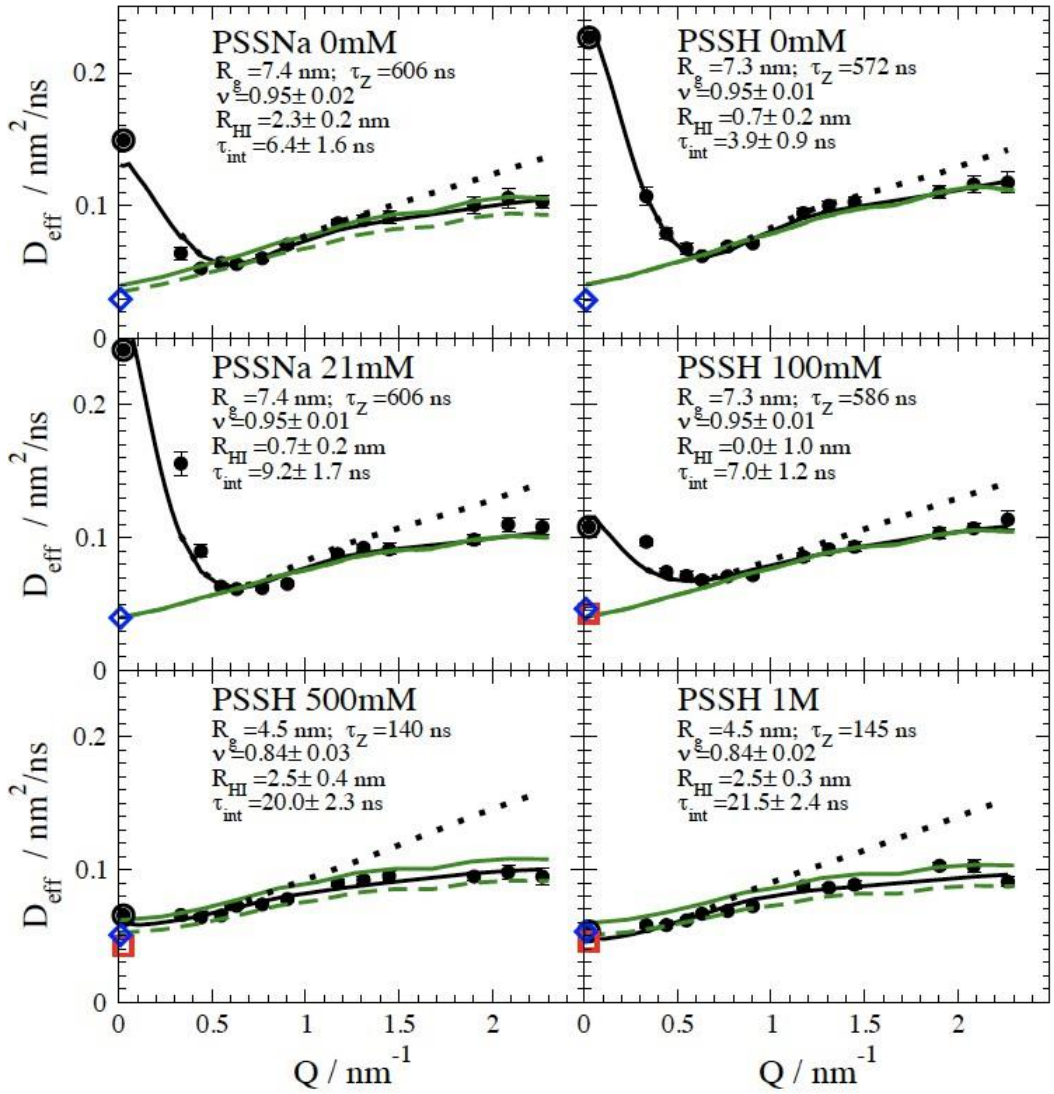

Fig. S9 Effective diffusion coefficients D_{eff} for PSS 39kDa with respective parameters from the full fit model: experimental (points); ZIF with full $H(Q)/S(Q)$ correction (black line); ZIF only with self-part correction D_s/D_0 (green dashed); same but $\tau_{int} = 0$ (ZIMM) (dotted); ZIF without correction (green line); DLS extrapolated concentration 0mg/ml (red square), 30m/ml (circle); PFG-NMR self-diffusion (blue diamond).

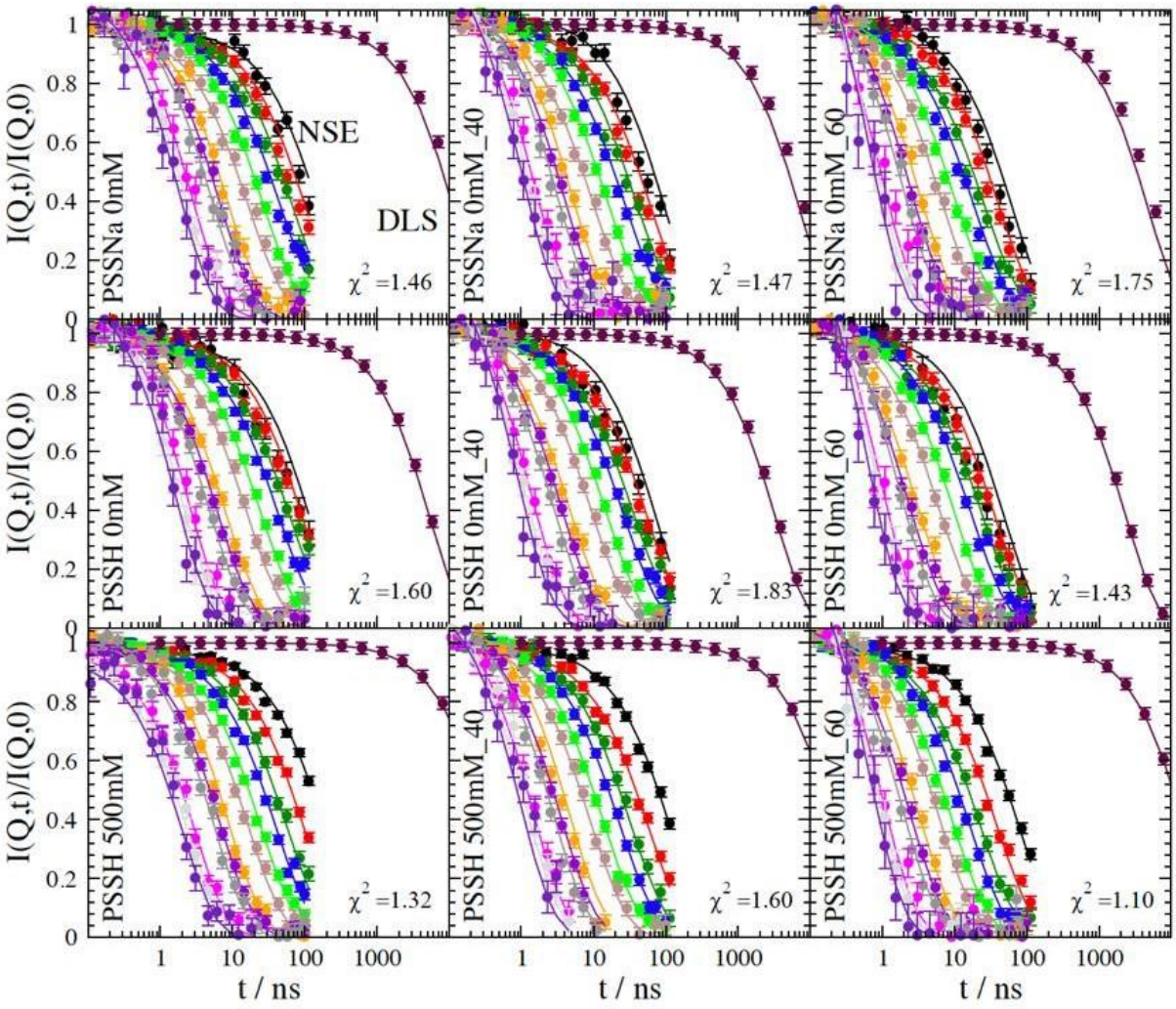

Fig. S10 NSE measured intermediate scattering function $I(Q,t)/I(Q,0)$ up to 100 ns for PSS 39 kDa at 30 mg/ml measured at IN15, ILL, Grenoble for 20, 40 and 60 ºC (from left to right). We add a synthetic Q=0.0264 nm^{-1} dataset that represents the measured collective diffusion coefficient from DLS at the same. Solid lines represent the combined fit using the $H(Q)/S(Q)$ corrected ZIF model with in general small χ^2.

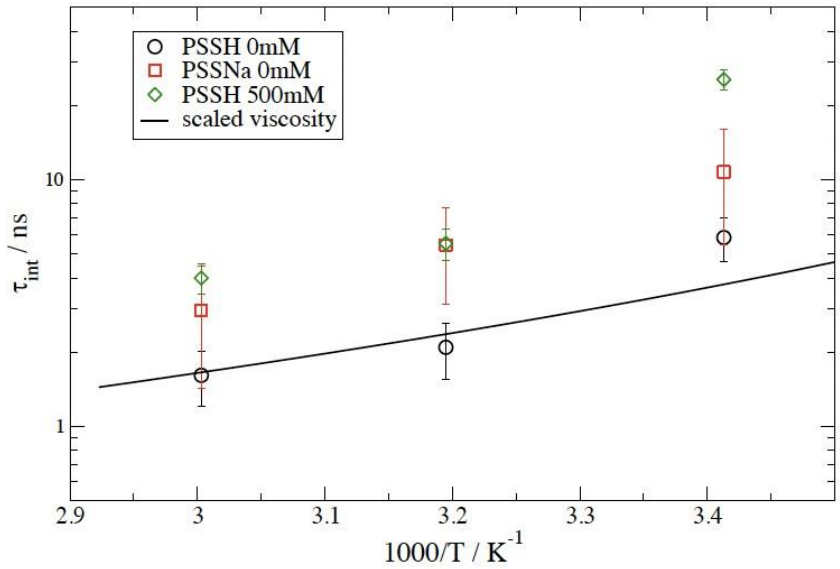

Fig. S11 Arrhenius behavior of internal friction in comparison to D_2O viscosity. Viscosity is scaled by an arbitrary factor 3000. The activation energy of water viscosity is 15.7 kJ/mol [108]. Similar slopes indicate a similar activation energy.

16.2. Detailed analysis of PECs structure

This section focuses on the formation and structural analysis of polyelectrolyte complexes (PECs) created by mixing oppositely charged poly amino acids (PAAs). The investigation covers the influence of environmental factors such as pH, salt concentration and temperature on PEC structure and phase behavior. Techniques like SAXS, optical microscopy and neutron magnetic resonance (NMR) spectroscopy were employed. Key findings include the observation of high-density droplet phases and ordered hexagonal or square arrays of α-helices, dependent on the salt concentration, providing insights into potential applications in drug delivery and tissue engineering.

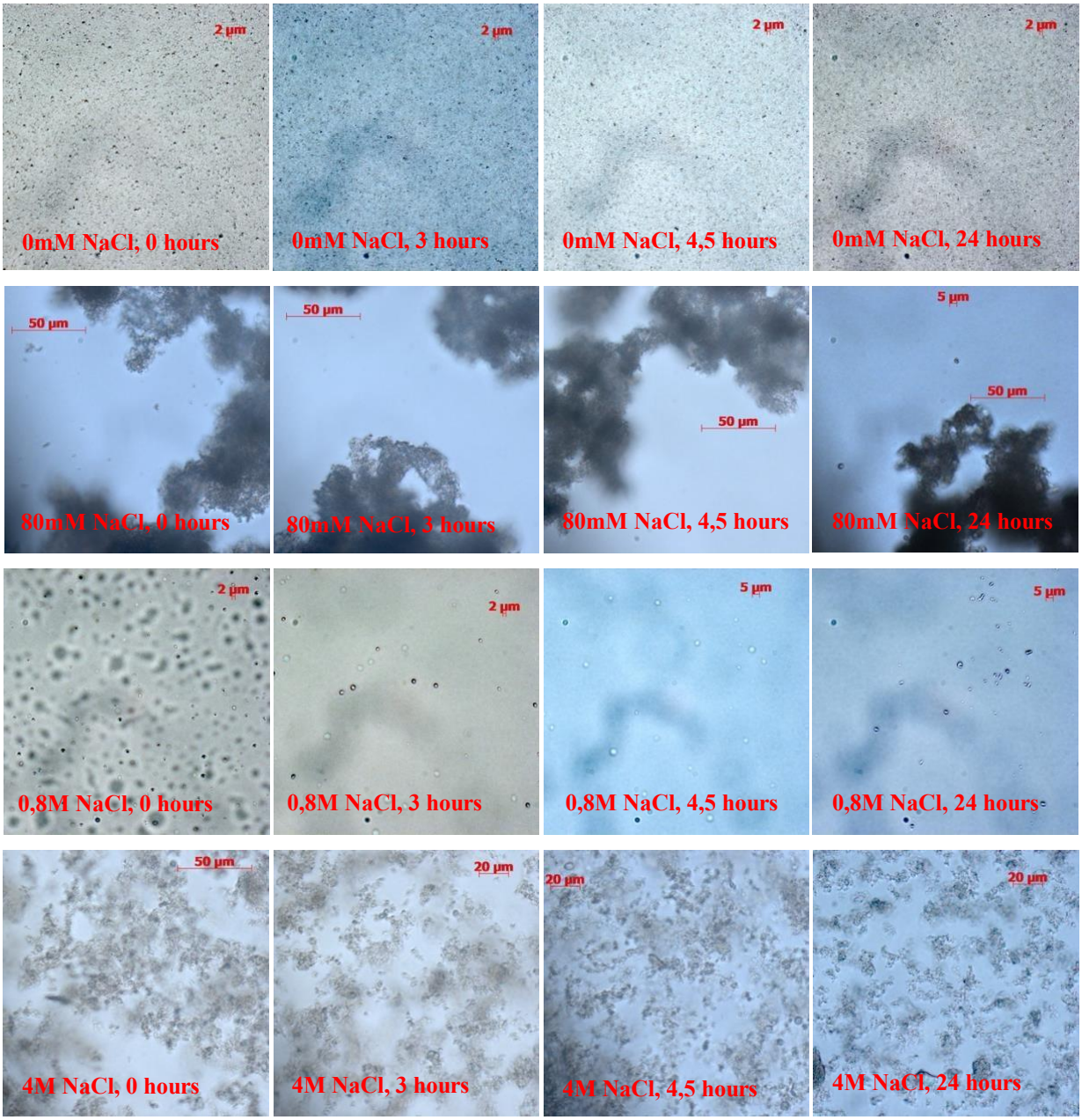

Fig. S12 Images from the optical microscope made for the mixtures of PASP and PLA at different NaCl concentrations directly after preparation, in 3, 4,5 and 24 hours, at 0,7 mM (10,7 mg/ml) total PE concentration.

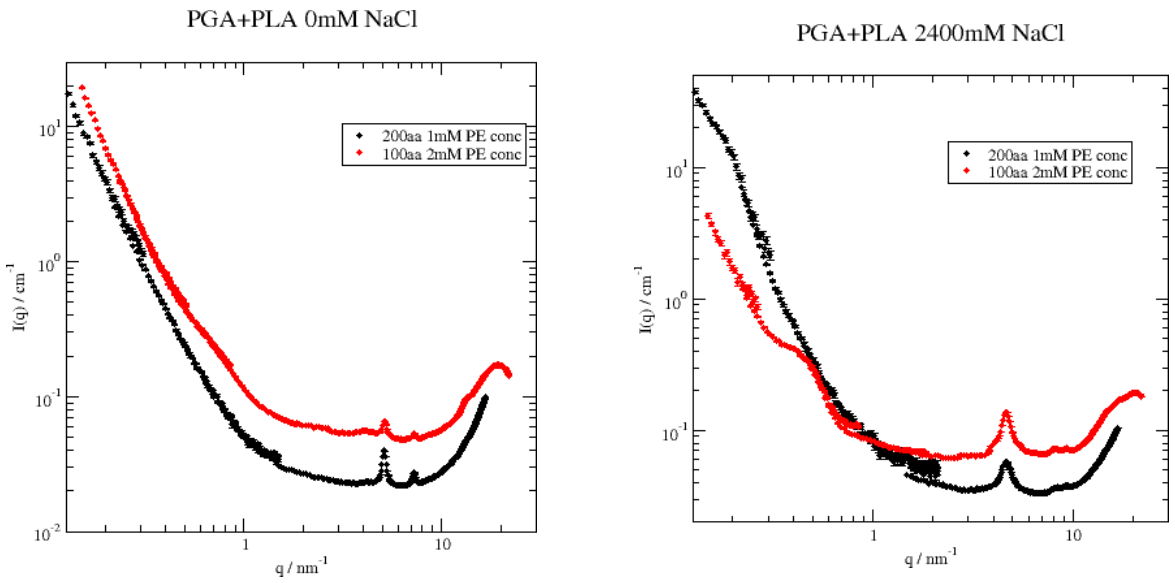

Fig. S13 Comparison of the SAXS curves for PGA+PLA PECs for 100 and 200 AAs/chain. Empty cell subtraction is done for all the curves.

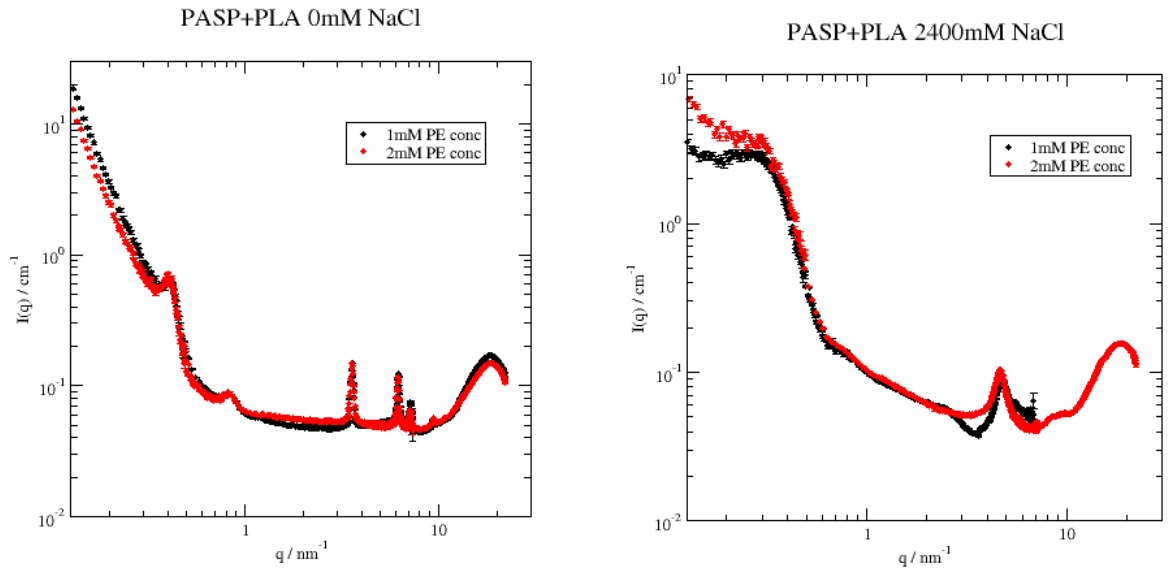

Fig. S14 Comparison of the SAXS curves for PASP+PLA PECs at 1 and 2 mM total PAAs concentration. Empty cell subtraction is done for all the curves.

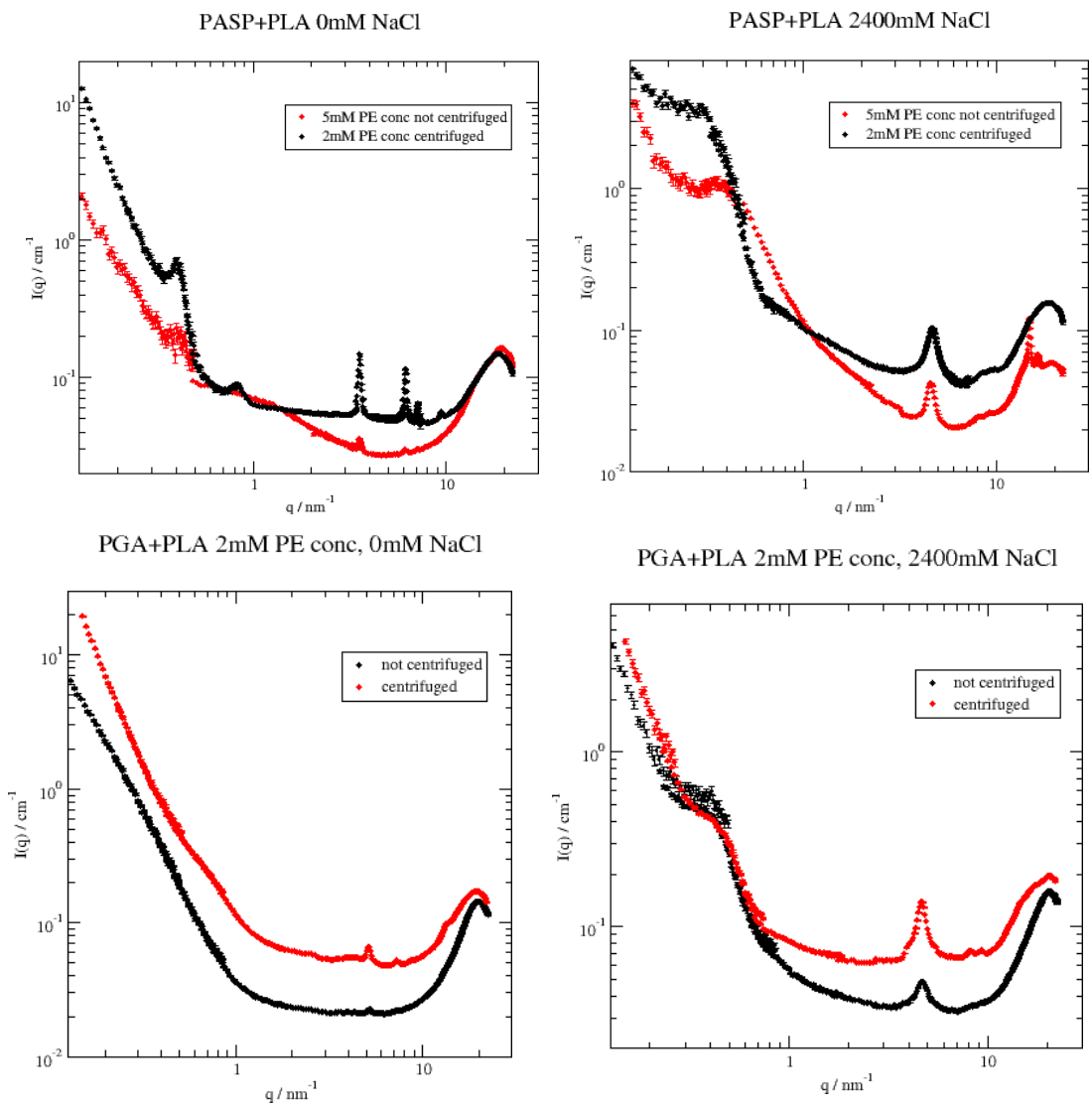

Fig. S15 Comparison of the SAXS curves for PASP/PGA+PLA PECs with and without centrifugation during samples preparation. Empty cell subtraction is done for all the curves.

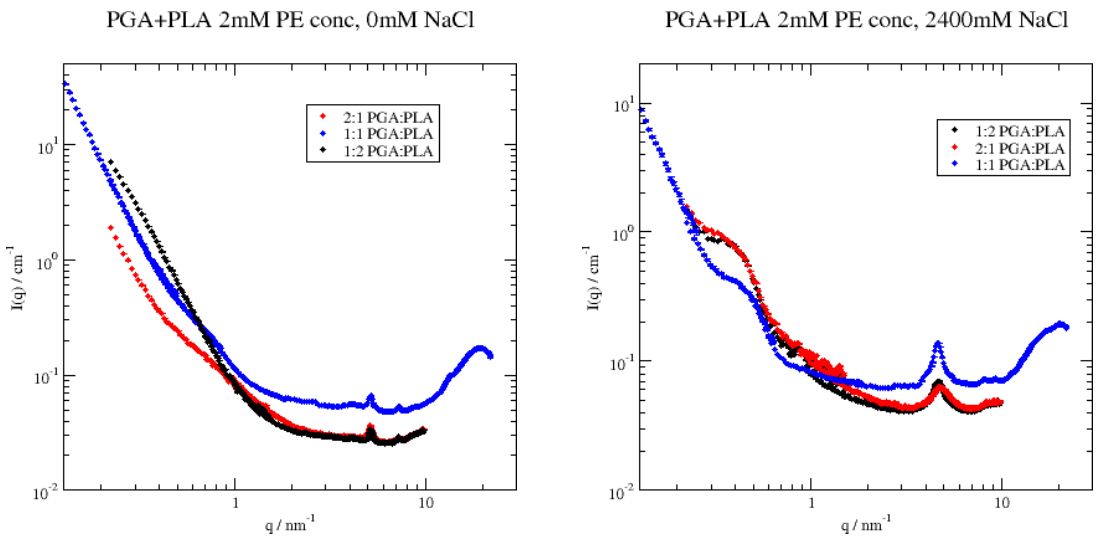

Fig. S16 Comparison of the SAXS curves for PGA+PLA PECs at different PAAs ratios. Empty cell subtraction is done for all the curves.

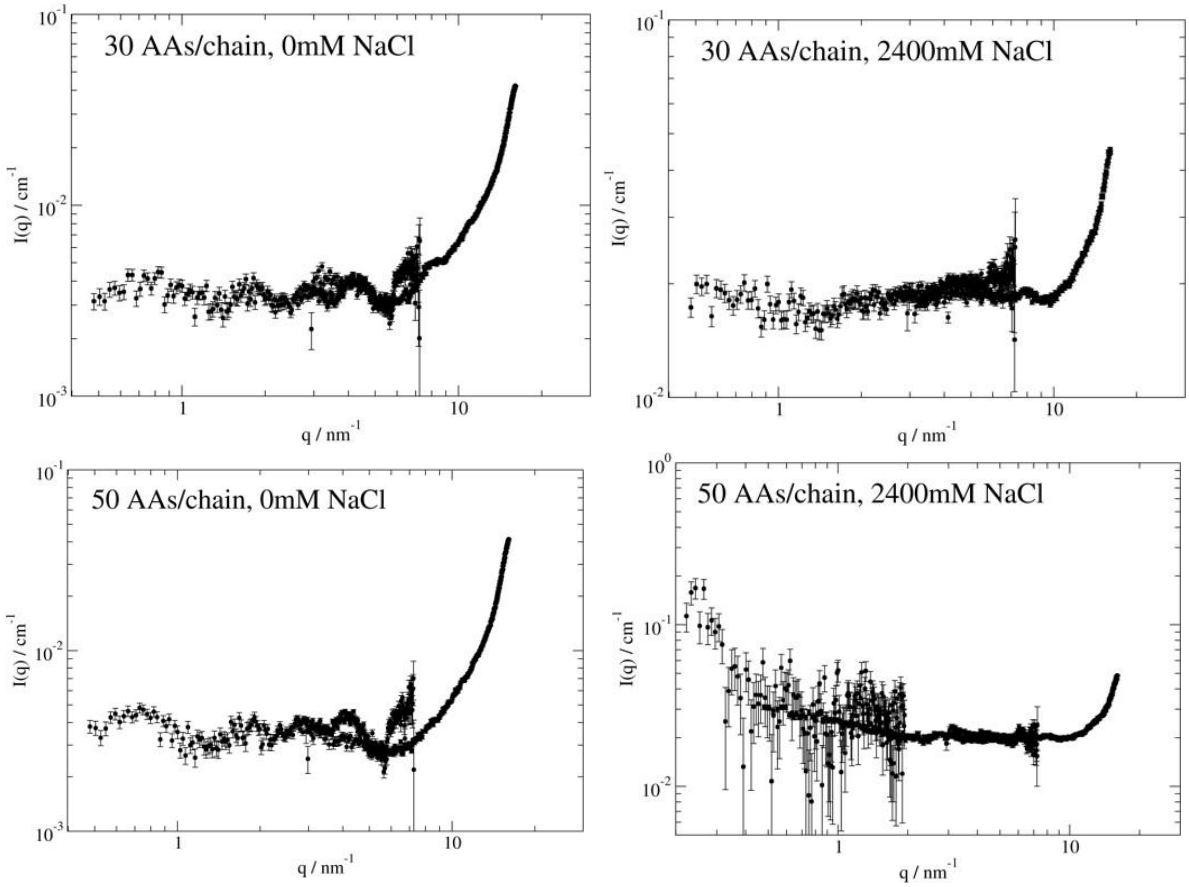

Fig. S17 SAXS curves for PASP+PLA PECs for 30 and 50 AAs/chain. Empty cell subtraction is done for all the curves.

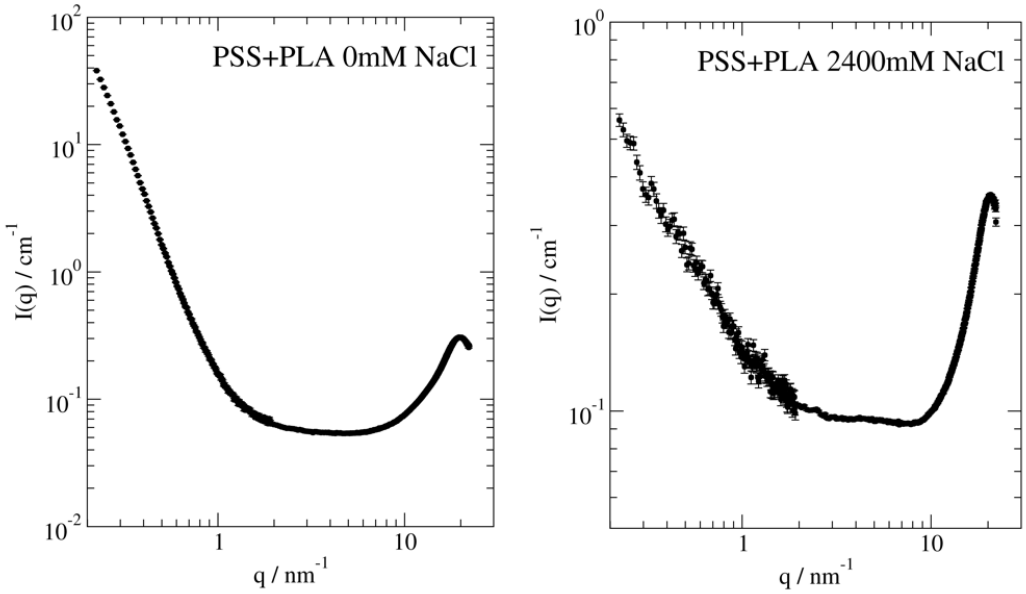

Fig. S18 SAXS curves for PSS 17kDa and PLA 100 AAs/chain PECs at 0 and 2400mM NaCl. Empty cell subtraction is done for all the curves.

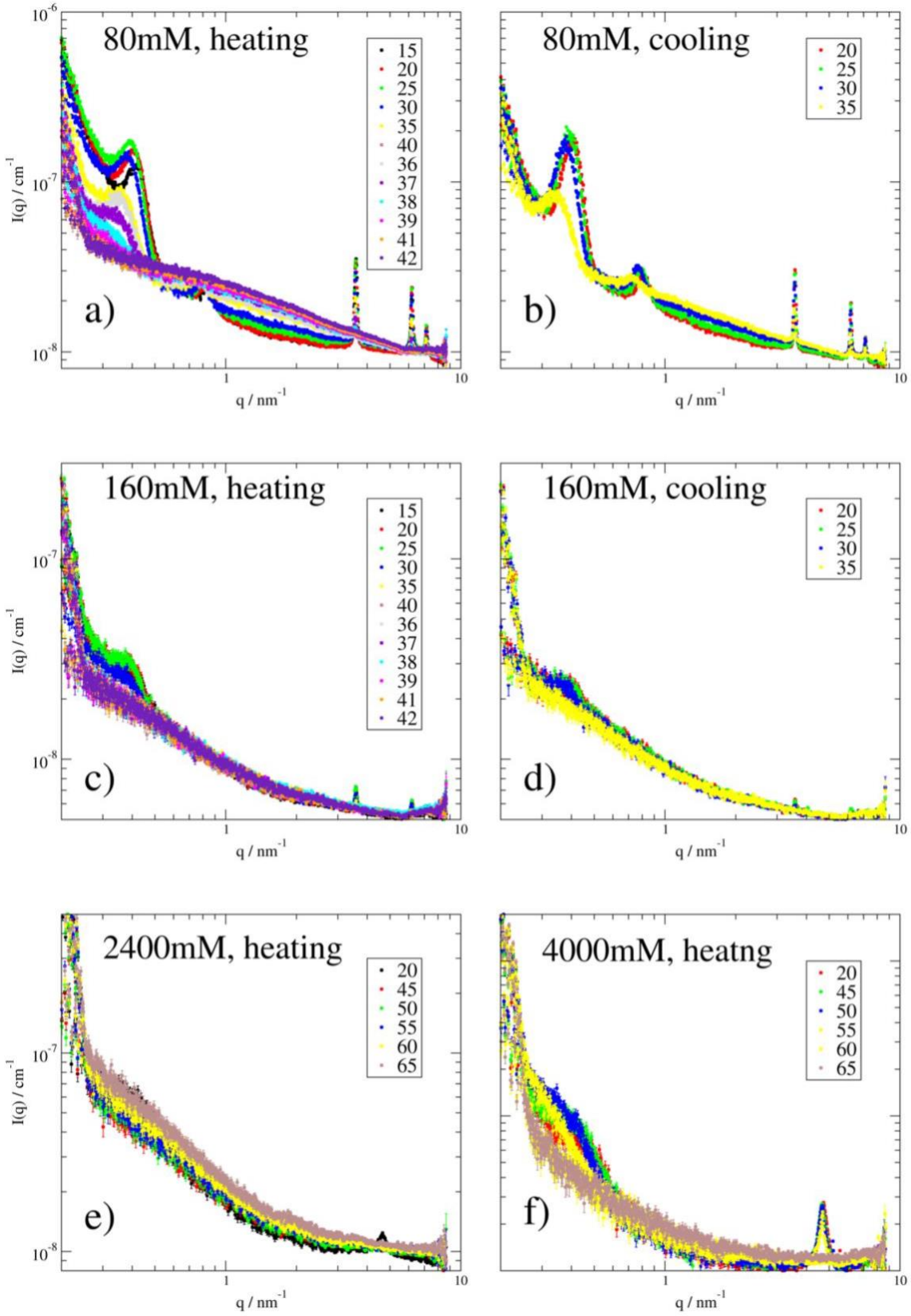

Fig. S19 Temperature scans for PASP+PLA 100 AAs/chain. Empty cell subtraction is done for all the curves. a),b) – 80mM NaCl; c),d) – 160mM NaCl; e) – 2400mM NaCl; f) – 4000mM NaCl.

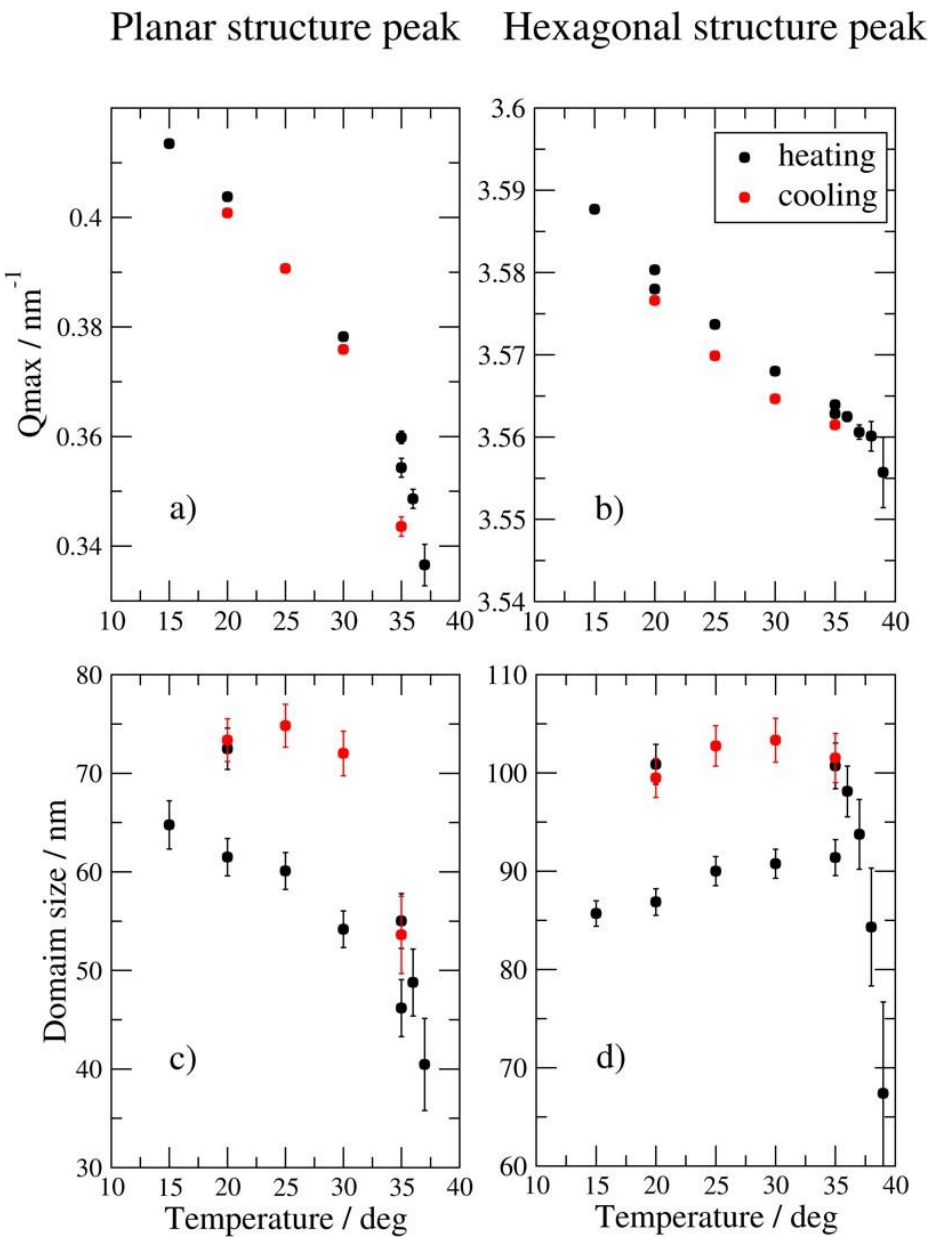

Fig. S20 Peaks' evaluation for PASP+PLA at 80 mM NaCl. a),b) Q value of the peak maximum at low Q values (planar structure peak, a)) and high Qs (hexagonal structure peak, b)); c),d) the domain size calculated using Equation (42) and FWHM of the peak at low Q values (planar structure peak, c)) and high Qs (hexagonal structure peak, d)).

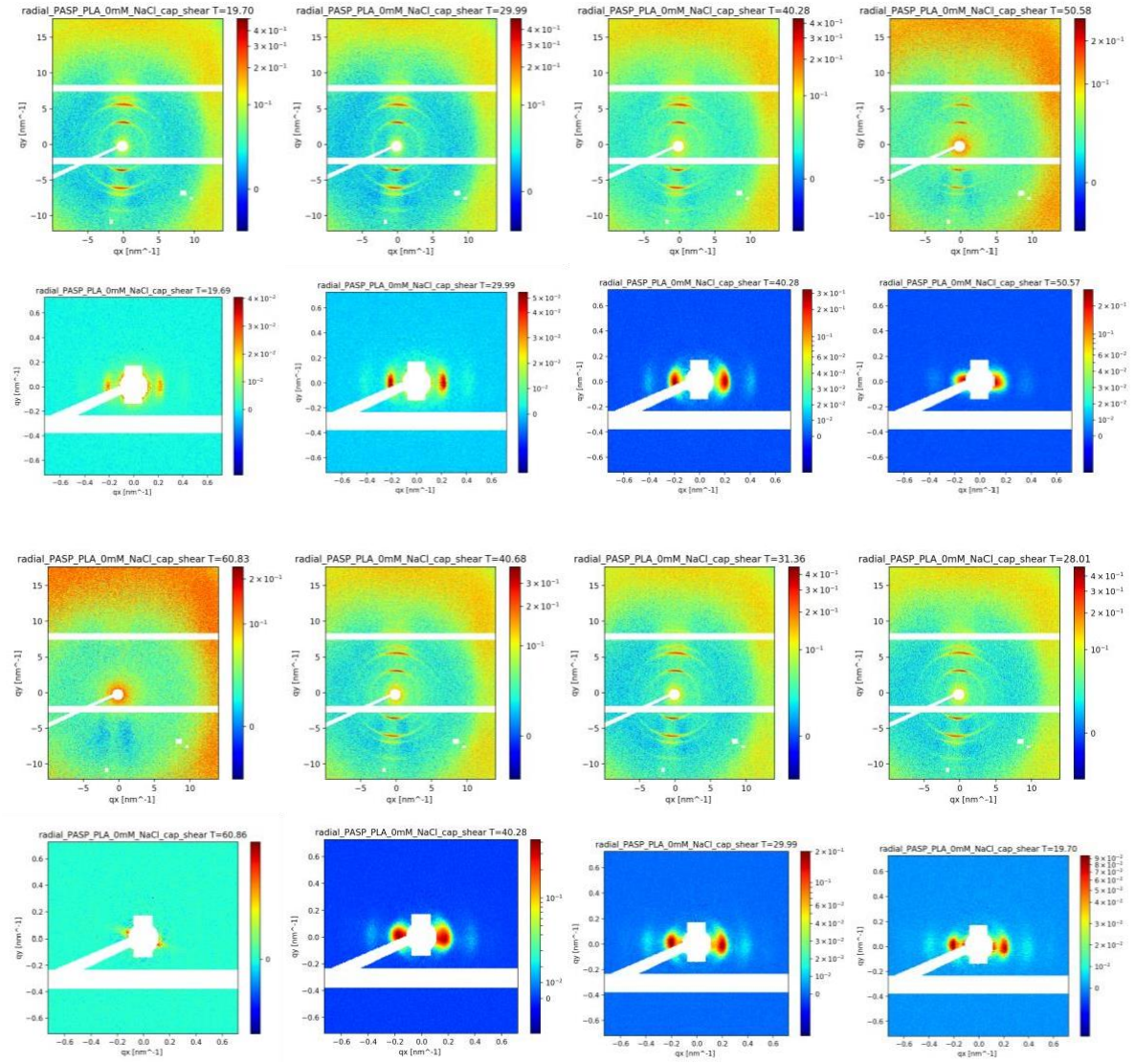

Fig. S21 Sheared PASP+PLA sample at 20, 30, 40 and 50°C upon heating and cooling down. The first and third rows are plots for high Q values, and the second and forth – for low Qs.

Empty cell subtracted PASP+PLA_200aa_0mM_NaCl_after_MF

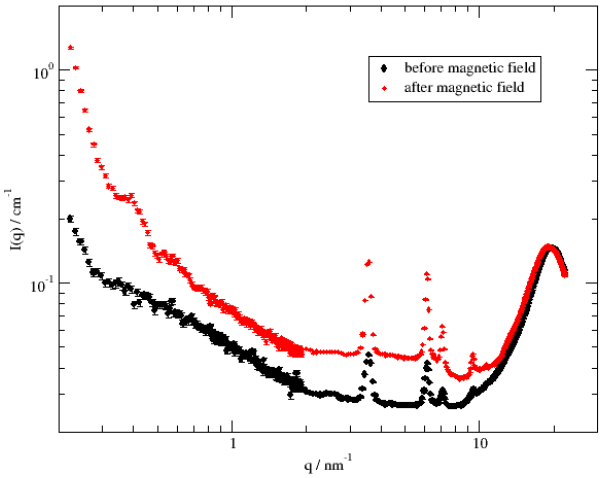

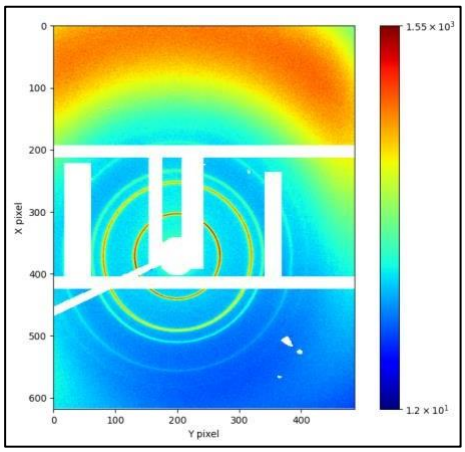

High Q peak

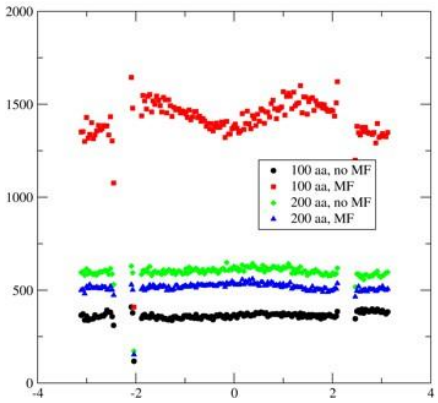

Empty cell subtracted PASP+PLA_100aa_2400mM_NaCl_after_MF

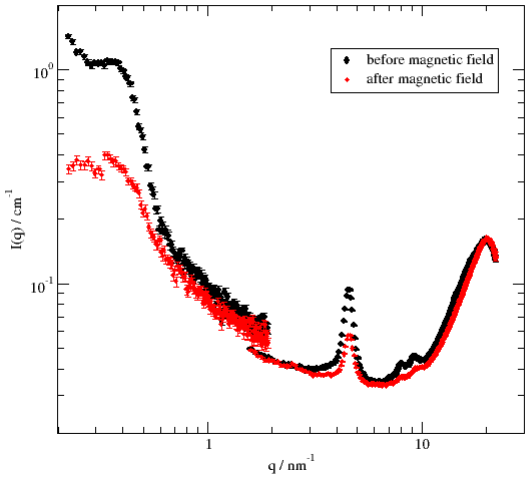

Fig. S22 Influence of the magnetic field on the PASP+PLA sample structure.

17. References

[1] Quiroz, F. G., & Chilkoti, A. (2015). Sequence heuristics to encode phase behaviour in intrinsically disordered protein polymers. Nature materials, 14(11), 1164–1171. https://doi.org/10.1038/nmat4418

[2] Munder, M. C., Midtvedt, D., Franzmann, T., Nüske, E., Otto, O., Herbig, M., Ulbricht, E., Müller, P., Taubenberger, A., Maharana, S., Malinovska, L., Richter, D., Guck, J., Zaburdaev, V., & Alberti, S. (2016). A pH-driven transition of the cytoplasm from a fluid- to a solid-like state promotes entry into dormancy. eLife, 5, e09347. https://doi.org/10.7554/eLife.09347

[3] Kroschwald, S., Munder, M. C., Maharana, S., Franzmann, T. M., Richter, D., Ruer, M., Hyman, A. A., & Alberti, S. (2018). Different Material States of Pub1 Condensates Define Distinct Modes of Stress Adaptation and Recovery. Cell reports, 23(11), 3327–3339. https://doi.org/10.1016/j.celrep.2018.05.041

[4] Franzmann, T. M., Jahnel, M., Pozniakovsky, A., Mahamid, J., Holehouse, A. S., Nüske, E., Richter, D., Baumeister, W., Grill, S. W., Pappu, R. V., Hyman, A. A., & Alberti, S. (2018). Phase separation of a yeast prion protein promotes cellular fitness. Science (New York, N.Y.), 359(6371), eaao5654. https://doi.org/10.1126/science.aao5654

[5] Ruff, K. M., Roberts, S., Chilkoti, A., & Pappu, R. V. (2018). Advances in Understanding Stimulus-Responsive Phase Behavior of Intrinsically Disordered Protein Polymers. Journal of molecular biology, 430(23), 4619–4635. https://doi.org/10.1016/j.jmb.2018.06.031

[6] Muthukumar M. (2017). 50th Anniversary Perspective: A Perspective on Polyelectrolyte Solutions. Macromolecules, 50(24), 9528–9560. https://doi.org/10.1021/acs.macromol.7b01929

[7] Fischer, J., Radulescu, A., Falus, P., Richter, D., & Biehl, R. (2021). Structure and Dynamics of Ribonuclease A during Thermal Unfolding: The Failure of the Zimm Model. The journal of physical chemistry. B, 125(3), 780–788. https://doi.org/10.1021/acs.jpcb.0c09476

[8] Lankalapalli, S., & Kolapalli, V. R. (2009). Polyelectrolyte Complexes: A Review of their Applicability in Drug Delivery Technology. Indian journal of pharmaceutical sciences, 71(5), 481–487. https://doi.org/10.4103/0250-474X.58165

[9] Ishihara, M., Kishimoto, S., Nakamura, S., Sato, Y., & Hattori, H. (2019).

Polyelectrolyte Complexes of Natural Polymers and Their Biomedical Applications. Polymers, 11(4), 672. https://doi.org/10.3390/polym11040672

[10] Alfrey, T., Jr., Berg, P.W. and Morawetz, H. (1951), The counterion distribution in solutions of rod-shaped polyelectrolytes†. J. Polym. Sci., 7: 543-547. https://doi.org/10.1002/pol.1951.120070509

[11] Fuoss, R. M., Katchalsky, A., & Lifson, S. (1951). The Potential of an Infinite Rod-Like Molecule and the Distribution of the Counter Ions. Proceedings of the National Academy of Sciences of the United States of America, 37(9), 579–589. https://doi.org/10.1073/pnas.37.9.579

[12] A. R. Khokhlov, "On the collapse of weakly charged polyelectrolytes," J. Phys. A. Math. Gen., vol. 13, no. 3, pp. 979–987, Mar. 1980.

[13] K. Kaji, H. Urakawa, T. Kanaya, R. Kitamaru. Phase diagram of polyelectrolyte solutions. Journal de Physique, 1988, 49 (6), pp.993-1000. ⟨10.1051/jphys:01988004906099300⟩. ⟨jpa-00210788⟩

[14] S. Förster and M. Schmidt, "Polyelectrolytes in solution," Adv. Polym. Sci., vol. 120, pp. 51–133, 1995.

[15] Gennes, P.-G & Pincus, P. & Velasco, Rosa & Brochard-Wyart, Francoise. (1976). Remarks on polyelectrolyte conformation, J.Physique 37, 1461-1498. http://dx.doi.org/10.1051/jphys:0197600370120146100. 37. 10.1051/jphys:0197600370120146100.

[16] Arun Yethiraj; Theory for chain conformations and static structure of dilute and semidilute polyelectrolyte solutions. J. Chem. Phys. 15 January 1998; 108 (3): 1184–1192. https://doi.org/10.1063/1.475480

[17] A. V. Dobrynin and M. Rubinstein, "Theory of polyelectrolytes in solutions and at surfaces," Progress in Polymer Science (Oxford), vol. 30, no. 11. Elsevier Ltd, pp. 1049–1118, 2005.

[18] Jabin, S., Kapoor, J.K. (2020). Role of Polyelectrolytes in the Treatment of Water and Wastewater. In: Inamuddin, Asiri, A. (eds) Sustainable Green Chemical Processes and their Allied Applications. Nanotechnology in the Life Sciences. Springer, Cham. https://doi.org/10.1007/978-3-030-42284-4_10

[19] Perry, S. L., Leon, L., Hoffmann, K. Q., Kade, M. J., Priftis, D., Black, K. A., Wong, D., Klein, R. A., Pierce, C. F., 3rd, Margossian, K. O., Whitmer, J. K., Qin, J., de Pablo, J. J., & Tirrell, M. (2015). Chirality-selected phase behaviour in ionic polypeptide complexes. Nature communications, 6, 6052. https://doi.org/10.1038/ncomms7052

[20] Porcel, C. H., & Schlenoff, J. B. (2009). Compact polyelectrolyte complexes: "saloplastic" candidates for biomaterials. Biomacromolecules, 10(11), 2968–2975. https://doi.org/10.1021/bm900373c

[21] Meng, S., Liu, Y., Yeo, J. et al. Effect of mixed solvents on polyelectrolyte complexes with salt. Colloid Polym Sci 298, 887–894 (2020). https://doi.org/10.1007/s00396-020-04637-0

[22] Chollakup, Rungsima & Smitthipong, Wirasak & Eisenbach, Claus & Tirrell, Matthew. (2010). Phase Behavior and Coacervation of Aqueous Poly(acrylic acid)−Poly(allylamine) Solutions. Macromolecules. 43. 10.1021/ma902144k.

[23] Priftis, Dimitrios & Tirrell, Matthew. (2012). Correction: Phase behaviour and complex coacervation of aqueous polypeptide solutions. Soft Matter. 8. 9396-9405. 10.1039/C2SM25604E.

[24] Chollakup, Rungsima & Beck, John & Dirnberger, Klaus & Tirrell, Matthew & Eisenbach, Claus. (2013). Polyelectrolyte Molecular Weight and Salt Effects on the Phase Behavior and Coacervation of Aqueous Solutions of Poly(acrylic acid) Sodium Salt and Poly(allylamine) Hydrochloride. Macromolecules. 46. 2376-2390. 10.1021/ma202172q.

[25] Fares, Hadi & Ghoussoub, Yara & Delgado, Jose David & Fu, Jingcheng & Urban, Volker & Schlenoff, Joseph. (2018). Scattering Neutrons Along the Polyelectrolyte Complex/Coacervate Continuum. Macromolecules. 51. 10.1021/acs.macromol.8b00699.

[26] Spruijt, Evan & Leermakers, Frans & Fokkink, Remco & Schweins, Ralf & Well, A.A. & Cohen Stuart, Martien & Gucht, Jasper. (2013). Structure and Dynamics of Polyelectrolyte Complex Coacervates Studied by Scattering of Neutrons, X-rays, and Light. Macromolecules. 46. 4596–4605. 10.1021/ma400132s.

[27] Fischer, Birgit and Abetz, Volker. "Determination of thermodynamic and structural quantities of polymers by scattering techniques" Pure and Applied Chemistry, vol. 90, no. 6, 2018, pp. 955-968. https://doi.org/10.1515/pac-2017-1101

[28] Biehl, R., & Richter, D. (2014). Slow internal protein dynamics in solution. Journal of physics. Condensed matter : an Institute of Physics journal, 26(50), 503103. https://doi.org/10.1088/0953-8984/26/50/503103

[29] D. I. Svergun and M. H. J. Koch, “Small-angle scattering studies of biological macromolecules in solution,” Reports Prog. Phys., 66, 1735, 2003. https://doi.org/10.1088/0034-4885/66/10/R05

[30] Zhang. F, “Small-Angle Scattering and Data Analysis,” Small-Angle Scatt. Data Anal.,

pp. 1–13, 2002.

[31] “SAXS Analysis in Structural Biology.”

[32] L. A. Feigin and D. I. Svergun, “Structure Analysis by Small-Angle X-Ray and Neutron Scattering.” 1987.

[33] Boualem Hammouda, Man-Ho Kim, “The empirical core-chain model, Journal of Molecular Liquids,” volume 247, 2017, pp. 434-440, ISSN 0167–7322, https://doi.org/10.1016/j.molliq.2017.09.114.

[34] Hansen, J. P., & Hayter, J. B. (1982). A rescaled MSA structure factor for dilute charged colloidal dispersions. Molecular Physics, 46(3), 651–656. https://doi.org/10.1080/00268978200101471

[35] S. K. Lai, G. F. Wang, W. P. Peng, and J. L. Wang, “Rescaled mean spherical approximation for concentrated charge-stabilized colloids,” Phys. B Condens. Matter, vol. 269, no. 2, pp. 183–188, Aug. 1999.

[36] Liu, Y., Chen, W. R., & Chen, S. H. (2005). Cluster formation in two-Yukawa fluids. The Journal of chemical physics, 122(4), 44507. https://doi.org/10.1063/1.1830433

[37] R. Biehl, “Jscatter, a program for evaluation and analysis of experimental data,” PLoS One, vol. 14, no. 6, pp. 1–18, 2019.

[38] Michael Kotlarchyk, Sow-Hsin Chen; Analysis of small angle neutron scattering spectra from polydisperse interacting colloids. J. Chem. Phys. 1 September 1983; 79 (5): 2461–2469. https://doi.org/10.1063/1.446055

[39] Förster, S., Timmann, A., Konrad, M., Schellbach, C., Meyer, A., Funari, S. S., Mulvaney, P., & Knott, R. (2005). Scattering curves of ordered mesoscopic materials. The journal of physical chemistry. B, 109(4), 1347–1360. https://doi.org/10.1021/jp0467494

[40] Förster, S., Timmann, A., Schellbach, C., Frömsdorf, A., Kornowski, A., Weller, H., Roth, S. V., & Lindner, P. (2007). Order causes secondary Bragg peaks in soft materials. Nature materials, 6(11), 888–893. https://doi.org/10.1038/nmat1995

[41] Feldman, D. (1989), The theory of polymer dynamics, by M. Doi and S. F. Edwards, the Clarendon Press, Oxford University Press, New York, 1986, 391 pp. J. Polym. Sci. C Polym. Lett., 27: 239-240. https://doi.org/10.1002/pol.1989.140270706

[42] M. Muthukumar; Double screening in polyelectrolyte solutions: Limiting laws and crossover formulas. J. Chem. Phys. 22 September 1996; 105 (12): 5183–5199. https://doi.org/10.1063/1.472362

[43] A. V. Dobrynin, R. H. Colby, and M. Rubinstein, “Scaling Theory of Polyelectrolyte

Solutions," Macromolecules, vol. 28, no. 6, 1995.

[44] M. Muthukumar; Dynamics of polyelectrolyte solutions. J. Chem. Phys. 15 August 1997; 107 (7): 2619–2635. https://doi.org/10.1063/1.474573

[45] Lopez C. G. (2019). Entanglement Properties of Polyelectrolytes in Salt-Free and Excess-Salt Solutions. ACS macro letters, 8(8), 979–983. https://doi.org/10.1021/acsmacrolett.9b00161

[46] Dou, S. and Colby, R.H. (2006), Charge density effects in salt-free polyelectrolyte solution rheology†. J. Polym. Sci. B Polym. Phys., 44: 2001-2013. https://doi.org/10.1002/polb.20853

[47] Boris, D. C., & Colby, R. H. (1998). Rheology of sulfonated polystyrene solutions. *Macromolecules*, *31*(17), 5746-5755. https://doi.org/10.1021/ma971884i

[48] Lopez, C. G., & Richtering, W. (2019). Viscosity of Semidilute and Concentrated Nonentangled Flexible Polyelectrolytes in Salt-Free Solution. The journal of physical chemistry. B, 123(26), 5626–5634. https://doi.org/10.1021/acs.jpcb.9b03044

[49] Hayter, J. & Janninck, G. & Brochard-Wyart, Francoise & Gennes, P.. (1980). Correlations and dynamics of polyelectrolyte solutions. http://dx.doi.org/10.1051/jphyslet:019800041018045100. 41. 10.1051/jphyslet:019800041018045100.

[50] R. Biehl, M. Monkenbusch, and D. Richter, "Exploring internal protein dynamics by neutron spin echo spectroscopy," Soft Matter, vol. 7, no. 4, pp. 1299–1307, 2011.

[51] Stadler, A. M., Stingaciu, L., Radulescu, A., Holderer, O., Monkenbusch, M., Biehl, R., & Richter, D. (2014). Internal nanosecond dynamics in the intrinsically disordered myelin basic protein. Journal of the American Chemical Society, 136(19), 6987–6994. https://doi.org/10.1021/ja502343b

[52] Richter, D. & Monkenbusch, Michael & Arbe, Arantxa & Colmenero, Juan. (2005). Neutron Spin Echo in Polymer Systems. 10.1007/b106578.

[53] Slim, A. H., Shi, W. H., Safi Samghabadi, F., Faraone, A., Marciel, A. B., Poling-Skutvik, R., & Conrad, J. C. (2022). Electrostatic Repulsion Slows Relaxations of Polyelectrolytes in Semidilute Solutions. ACS macro letters, 11(7), 854–860. https://doi.org/10.1021/acsmacrolett.2c00213

[54] B. J. Ackerson, P. N. Pusey, R. J. A. Tough; Interpretation of the intermediate scattering function at short times. J. Chem. Phys. 1 February 1982; 76 (3): 1279–1282. https://doi.org/10.1063/1.443146

[55] C.W.J. Beenakker, P. Mazur, Self-diffusion of spheres in a concentrated suspension, Physica A: Statistical Mechanics and its Applications, volume 120, issue 3, 1983, pp.

388-410, ISSN 0378-4371, https://doi.org/10.1016/0378-4371(83)90061-4.

[56] C.W.J. Beenakker, P. Mazur, Diffusion of spheres in a concentrated suspension II, Physica A: Statistical Mechanics and its Applications, volume 126, issue 3, 1984, Pages 349-370, ISSN 0378-4371, https://doi.org/10.1016/0378-4371(84)90206-1.

[57] Banchio, A. J., Heinen, M., Holmqvist, P., & Nägele, G. (2018). Short- and long-time diffusion and dynamic scaling in suspensions of charged colloidal particles. The Journal of chemical physics, 148(13), 134902. https://doi.org/10.1063/1.5017969

[58] S. Longeville, W. Doster, and G. Kali, "Myoglobin in crowded solutions: Structure and diffusion," Chemical Physics, volume 292, issues 2–3, 2003, pp. 413-424, ISSN 0301-0104, https://doi.org/10.1016/S0301-0104(03)00292-1.

[59] Biehl, R., Hoffmann, B., Monkenbusch, M., Falus, P., Préost, S., Merkel, R., & Richter, D. (2008). Direct observation of correlated interdomain motion in alcohol dehydrogenase. Physical review letters, 101(13), 138102. https://doi.org/10.1103/PhysRevLett.101.138102

[60] Stadler, A. M., Stingaciu, L., Radulescu, A., Holderer, O., Monkenbusch, M., Biehl, R., & Richter, D. (2014). Internal nanosecond dynamics in the intrinsically disordered myelin basic protein. Journal of the American Chemical Society, 136(19), 6987–6994. https://doi.org/10.1021/ja502343b

[61] Inoue, R., Biehl, R., Rosenkranz, T., Fitter, J., Monkenbusch, M., Radulescu, A., Farago, B., & Richter, D. (2010). Large domain fluctuations on 50-ns timescale enable catalytic activity in phosphoglycerate kinase. Biophysical journal, 99(7), 2309–2317. https://doi.org/10.1016/j.bpj.2010.08.017

[62] Stingaciu, L. R., Ivanova, O., Ohl, M., Biehl, R., & Richter, D. (2016). Fast antibody fragment motion: flexible linkers act as entropic spring. Scientific reports, 6, 22148. https://doi.org/10.1038/srep22148

[63] P. N. Pusey, "The dynamics of interacting Brownian particles," J. Phys. A. Math. Gen., vol. 8, no. 9, 1975. https://doi.org/10.1088/0305-4470/8/9/012

[64] Bruce J. Ackerson; Correlations for interacting Brownian particles. II. J. Chem. Phys. 15 July 1978; 69 (2): 684–690. https://doi.org/10.1063/1.436634

[65] D. Feldman, "The theory of polymer dynamics, by M. Doi and S. F. Edwards, the Clarendon Press, Oxford University Press, New York, 1986, 391 pp.," J. Polym. Sci. Part C Polym. Lett., vol. 27, no. 7, 1989.

[66] I. Teraoka, Polymer Solutions: An Introduction to Physical Properties, vol. 3. 2018б ззю 167–275, https://doi.org/10.1002/0471224510.ch3.

[67] Khatri, Bhavin & Mcleish, Tom. (2007). Rouse Model with Internal Friction: A Coarse

Grained Framework for Single Biopolymer Dynamics. Macromolecules. 40. 10.1021/ma071175x.

[68] Cheng, R. R., Hawk, A. T., & Makarov, D. E. (2013). Exploring the role of internal friction in the dynamics of unfolded proteins using simple polymer models. The Journal of chemical physics, 138(7), 074112. https://doi.org/10.1063/1.4792206

[69] Malvern and M. Instruments, "Dynamic Light Scattering : An Introduction in 30 Minutes," Tech. Note MRK656-01, 2011.

[70] U. Genz and R. Klein, "Collective diffusion of charged spheres in the presence of hydrodynamic interaction," Physica A: Statistical Mechanics and its Applications, volume 171, issue 1, 1991, pp. 26-42, ISSN 0378-4371, https://doi.org/10.1016/0378-4371(91)90355-G..

[71] Koch, M. H., Vachette, P., & Svergun, D. I. (2003). Small-angle scattering: a view on the properties, structures and structural changes of biological macromolecules in solution. Quarterly reviews of biophysics, 36(2), 147–227. https://doi.org/10.1017/s0033583503003871

[72] H. Schnablegger and Y. Singh, "The SAXS Guide," Ant. Paar GmbH, 2013.

[73] Lake, J. A. (1967). An iterative method of slit-correcting small angle X-ray data. Acta Crystallographica, 23(2), 191–194. https://doi.org/10.1107/S0365110X67002440

[74] "SAXS Analysis in Structural Biology."

[75] "Neutron Scattering A primer R Pynn Los alamos."

[76] B. Jacrot, "The study of biological structures by neutron scattering from solution," Reports Prog. Phys., vol. 39, no. 156, pp. 911–953, 1976. https://doi.org/10.1088/0034-4885/39/10/001.

[77] Radulescu, Aurel & Pipich, Vitaliy & Frielinghaus, H. & Appavou, Marie-Sousai. (2012). KWS-2, the high intensity / wide Q-range small-angle neutron diffractometer for soft-matter and biology at FRM II. Journal of Physics: Conference Series. 351. 10.1088/1742-6596/351/1/012026.

[78] Houston, J. E., Brandl, G., Drochner, M., Kemmerling, G., Engels, R., Papagiannopoulos, A., Sarter, M., Stadler, A., & Radulescu, A. (2018). The high-intensity option of the SANS diffractometer KWS-2 at JCNS - characterization and performance of the new multi-megahertz detection system. Journal of applied crystallography, 51(Pt 2), 323–336. https://doi.org/10.1107/S1600576718004132

[79] Radulescu, Aurel & Székely, Noémi Kinga & Appavou, Marie-Sousai. (2015). KWS-2: Small angle scattering diffractometer. Journal of large-scale research facilities JLSRF. 1. https://doi.org/10.17815/jlsrf-1-27.

[80] V. Pipich, “QtiKWS.” [Online]. Available: https://www.qtisas.com/qtikws. [Accessed: 22-Feb-2023].

[81] B. Ewen and D. Richter, “Neutron Spin Echo Investigations on the Segmental Dynamics of Polymers in Melts, Networks and Solutions,” Adv. Polym. Sci., vol. 134, 1997, pp. 606–609, ISSN 1359-0286, https://doi.org/10.1016/S1359-0286(98)80034-X.

[82] Farago, B. & Falus, P. & Hoffmann, Ingo & Gradzielski, Michael & Thomas, Frederic & Gomez, C.. (2015). The IN15 upgrade. Neutron News. 26. 10.1080/10448632.2015.1057052.

[83] A. SOMMERFELD, Chapter II - About the Propagation of Light in Dispersive Media* *This Chapter is an authorized translation of A. Sommerfeld, Ann. Physik [4] 44, 177 (1914)., Editor(s): LÉON BRILLOUIN, Pure and Applied Physics, Elsevier, volume 8, 1960, pp. 17–42, ISSN 0079-8193, ISBN 9781483230689, https://doi.org/10.1016/B978-1-4832-3068-9.50007-6.

[84] R. Pecora, Dynamic Light Scattering, 1st ed. New York: Springer US, 1985.

[85] A. Masahiko, Measurement Techniques and Practices of Colloid and Interface Phenomena, 1st ed. Springer Singapore, 2019.

[86] W. I. Goldburg; Dynamic light scattering. Am. J. Phys. 1 December 1999; 67 (12): 1152–1160. https://doi.org/10.1119/1.19101.

[87] S. W. Provencher, “Contin: A general purpose constrainded regularization program for inverting noisy linear algebraic and integral equations,” Computer Physics Communications, volume 27, issue 3, 1982, pp. 229–242, ISSN 0010-4655, https://doi.org/10.1016/0010-4655(82)90174-6.

[88] Kärger, Jörg & FLEISCHER, G.. (2010). ChemInform Abstract: NMR Diffusion Studies in Heterogeneous Systems. Cheminform. 26. 10.1002/chin.199502319.

[89] B. Blümich, “P. T. Callaghan. Principles of nuclear magnetic resonance microscopy. Oxford University Press, Oxford, 1993, 492 pp. ISBN 0 198 53997 5,” Magn. Reson. Chem., vol. 33, no. 4, 1995.

[90] Sørland, Geir. (2014). Dynamic Pulsed-Field-Gradient NMR. https://doi.org/10.1007/978-3-662-44500-6.

[91] D. B. Murphy and M. W. Davidson, Fundamentals of Light Microscopy and Electronic Imaging: Second Edition. 2012, pp. 1–19. https://doi.org/10.1002/9781118382905.ch1.

[92] Sanderson, Jeremy. (2020). Fundamentals of Microscopy. Current Protocols in Mouse Biology. 10. 10.1002/cpmo.76.

[93] S. Förster, M. Schmidt, and M. Antonietti, “Static and dynamic light scattering by aqueous polyelectrolyte solutions: effect of molecular weight, charge density and added

salt," Polymer, vol. 31, no. 5. pp. 781–792, 1990, pp. 781–792, ISSN 0032-3861, https://doi.org/10.1016/0032-3861(90)90036-X.

[94] Jacobs, Michael & Lopez, Carlos & Dobrynin, Andrey. (2021). Quantifying the Effect of Multivalent Ions in Polyelectrolyte Solutions. Macromolecules. 54. 10.1021/acs.macromol.1c01326.

[95] M. B. R. B. E. F. S. H. I. H. O. P. S. A. M. S. S. J. W. L. Kruteva, "Dynamics of Polyelectrolyte Solutions," Grenoble, 2019.

[96] A. Arbe, J.A. Pomposo, A.J. Moreno, F. LoVerso, M. González-Burgos, I. Asenjo-Sanz, A. Iturrospe, A. Radulescu, O. Ivanova, J. Colmenero, Structure and dynamics of single-chain nano-particles in solution, Polymer, volume 105, 2016, pp. 532–544, ISSN 0032-3861, https://doi.org/10.1016/j.polymer.2016.07.059.

[97] A. Z. Akcasu, "Temperature and concentration dependence of diffusion coefficient in dilute solutions," Polymer (Guildf)., vol. 22, no. 9, 1981, pp. 1169–1180, ISSN 0032-3861, https://doi.org/10.1016/0032-3861(81)90129-4.

[98] Brûlet, A. & Boué, François & Cotton, Jenny. (1996). About the Experimental Determination of the Persistence Length of Wormlike Chains of Polystyrene. http://dx.doi.org/10.1051/jp2:1996217. 6. 10.1051/jp2:1996217.

[99] Suwalsky, M., & Traub, W. (1972). An X-ray diffraction study of poly-L-arginine hydrochloride. Biopolymers, 11(3), 623–632. https://doi.org/10.1002/bip.1972.360110307.

[100] Hura, Greg & Sorenson, Jon & Glaeser, Robert. (2000). A High-Quality X-Ray Scattering Experiment on Liquid Water at Ambient Conditions. The Journal of Chemical Physics. 113. 9140-9148. 10.1063/1.1319614.

[101] A. L. Patterson, "The scherrer formula for X-ray particle size determination," Phys. Rev., vol. 56, no. 10, 1939. 10.1103/PhysRev.56.978

[102] G. Maret, M. V. Schickfus, A. Mayer, and K. Dransfeld, "Orientation of Nucleic Acids in High Magnetic Fields," Phys. Rev. Lett., vol. 35, no. 6, 1975. 10.1103/PhysRevLett.35.397

[103] Brandes, R., & Kearns, D. R. (1986). Magnetic ordering of DNA liquid crystals. Biochemistry, 25(20), 5890–5895. https://doi.org/10.1021/bi00368a008

[104] Salamonczyk, M., Zhang, J., Portale, G., Zhu, C., Kentzinger, E., Gleeson, J. T., Jakli, A., De Michele, C., Dhont, J. K., Sprunt, S., & Stiakakis, E. (2016). Smectic phase in suspensions of gapped DNA duplexes. Nature communications, 7, 13358. https://doi.org/10.1038/ncomms13358

[105] Lopez, Carlos. (2019). Scaling and Entanglement Properties of Neutral and Sulfonated

Polystyrene. Macromolecules. 10.1021/10.1021/acs.macromol.9b01583.

[106] Hammouda, B.. (2010). Analysis of the Beaucage model. Journal of Applied Crystallography. 43. 10.1107/S0021889810033856.

[107] G. Jerke, J. S. Pedersen, S. U. Egelhaaf, and P. Schurtenberger, "Static structure factor of polymerlike micelles: Overall dimension, flexibility, and local properties of lecithin reverse micelles in deuterated isooctane," Phys. Rev. E - Stat. Physics, Plasmas, Fluids, Relat. Interdiscip. Top., vol. 56, no. 5, 1997. 10.1103/PhysRevE.56.5772.

[108] Messaâdi, Aymen & Dhouibi, Nesrine & Hamda, Hatem & Belgacem, Fethi & Abdelkader, Yousry & Ouerfelli, Noureddine & Hamzaoui, A.. (2015). A New Equation Relating the Viscosity Arrhenius Temperature and the Activation Energy for Some Newtonian Classical Solvents. E-Journal of Chemistry. 2015. 1-15. 10.1155/2015/163262.

[109] Fratzl, Peter. (2008). Collagen: Structure and Mechanics. 10.1007/978-0-387-73906-9.

[110] Shoulders, M. D., & Raines, R. T. (2009). Collagen structure and stability. Annual review of biochemistry, 78, 929–958. https://doi.org/10.1146/annurev.biochem.77.032207.120833